NSF Grants ATM-9726464 and DGE-9616044

National Science Foundation

LIFECYCLE CHARACTERISTICS AND ORGANIZATION OF TROPICAL ISLAND CONVECTION

by David A. Ahijevych and Steven A. Rutledge

Colorado State University

DEPARTMENT OF ATMOSPHERIC SCIENCE

PAPER NO. 680

LIFECYCLE CHARACTERISTICS AND ORGANIZATION OF TROPICAL ISLAND CONVECTION

by

David A. Ahijevych

and

Steven A. Rutledge

Department of Atmospheric Science

Colorado State University

Fort Collins, CO 80523

Research Supported by

National Science Foundation

under Grants ATM-9726464 and DGE-9616044

Summer 1999

Atmospheric Science Paper No. 680

COLORADO STATE UNIVERSITY

December 7, 1998

WE HEREBY RECOMMEND THAT THE THESIS PREPARED UNDER OUR SUPERVISION BY DAVID A. AHIJEVYCH ENTITLED *LIFECYCLE CHARACTERISTICS AND ORGANIZATION OF TROPICAL ISLAND CONVECTION* BE ACCEPTED AS FULFILLING IN PART REQUIREMENTS FOR THE DEGREE OF MASTER OF SCIENCE.

Committee on Graduate Work

Adviser

Department Head/Director

ABSTRACT OF THESIS

LIFECYCLE CHARACTERISTICS AND ORGANIZATION OF TROPICAL ISLAND CONVECTION

The Maritime Continent Thunderstorm Experiment (MCTEX) was conducted over the Tiwi Islands just off the coast of northern Australia. Two MCTEX case studies are presented herein. The evolution of diurnally-forced convection over the Tiwi Islands is explored, starting with the initial stages of cumulus development, to the mature thunderstorm stage, and finally to the dissipative stage. The convection is described from both a kinematic and electrical perspective.

The leeward coast sea breeze front was the site of the first deep convection. Shallow precipitating cells originating from the island interior created evaporatively-cooled downdrafts that triggered the deep convection as they approached the front. Rapid development ensued as higher-order cloud mergers continued along the sea breeze front, leading to vigorous, electrically active storms. A deep, expanding cold pool at the surface cut off the main storm from its supply of buoyant air. Convection continued along the downshear edge of the cold pool where the low-level shear tended to balance the horizontal vorticity generated by the cold pool.

Polarimetric radar was used to estimate various precipitation quantities, and the relation between lightning and precipitation was investigated. Most of the results were consistent with the non-inductive charging (NIC) mechanism. No lightning was detected in predominately warm-rain cells. Only after significant quantities of millimeter-sized ice particles were produced was lightning detected. Cloud-to-ground

(CG) lightning was somewhat correlated with surface rainfall, but appeared to be more closely tied to the graupel mass in the mixed-phase region. It is postulated that the cloud merger process produces a storm environment favorable for non-inductive charging. Stronger updrafts are capable of suspending more raindrops above the freezing level, creating an ample graupel supply. The presence of supercooled cloud water and ice crystals from the previous cells led to rapid storm electrification. CG flash rates lagged graupel mass by a few minutes, which was consistent with the formation of a lower positive charge center below the main negative charge layer. This origin of this positive charge center could be explained by non-inductive charging of graupel particles falling below the level of charge reversal.

David A. Ahijevych
Atmospheric Science Department
Colorado State University
Fort Collins, CO 80523
Spring 1999

ACKNOWLEDGMENTS

I would like to thank Dr. Rutledge, Dr. Eykholt and Dr. Montgomery for serving on my graduate advisory committee. Special thanks to all members of the CSU Atmospheric Science Radar and Electricity group for generous computer, secretarial, and research assistance. I appreciate the valuable scientific exchanges that occurred inside and outside of the classroom. I would also like to thank everyone who provided MCTEX data sets and various research suggestions, including Mr. Larry Carey (CSU), Dr. Andrew Crook (NCAR), Dr. Tom Keenan (BMRC), Mr. Chris Burghart (NCAR), Dr. Jim Wilson (NCAR), and Mr. Jeff Bailey (NASA/MSFC).

This material is based upon work supported under a National Science Foundation Graduate Fellowship. Any opinions, findings, conclusions or recommendations expressed in this publication are those of the author and do not necessarily reflect the views of the National Science Foundation. Additional funding was provided by NSF grant ATM-9726464 (Dynamical and Electrical Studies of Convection).

TABLE OF CONTENTS

LIST OF TABLES

LIST OF FIGURES

CHAPTER 1

Introduction

1.1 Motivation for study

Since World War II, atmospheric scientists have turned a more watchful eye to the area between 30° N and 30° S, where approximately two thirds of the global precipitation occurs (Sellers, 1969). The convective cloud systems which frequent the equatorial trough and power the upward branch of the Hadley circulation not only directly impact the local population, but indirectly influence weather patterns and people over the entire globe. Newer and more robust computer models with domains spanning the entire globe require better understanding of the tropics, from the large scale radiational forcing caused by extensive thunderstorm anvils to the small scale dynamics of trade wind cumulus. Satellites have revealed that much of the earth's deep convection regularly occurs over regions of sparse observational coverage (Janowiak et al., 1985), and space-borne sensors offer an excellent tool for obtaining estimates of large-scale precipitation over vast tropical oceans and continental interiors. Multinational projects such as the Tropical Rainfall Measuring Mission (TRMM; Simpson et al., 1988) require a synergy between such space-based observational platforms and surface-based validation studies since satellite techniques and measurements require ground-truth data to be thoroughly refined and properly calibrated.

1.2 Tropical field campaigns

In recent years, several field campaigns have addressed the lack of observational data in the tropics. The Global Atmosphere Program (GARP) Atlantic Tropical Experiment GATE, the Tropical Ocean-

Global Atmosphere (TOGA) Coupled Ocean-Atmosphere Response Experiment (COARE) (Webster and Lucas, 1992), the Central Pacific Equatorial Experiment (CEPEX; 1993), and the Equatorial Mesoscale Experiment (EMEX; Webster and House, 1991; Gamache et al., 1987) went a long ways towards helping us understand tropical oceanic convection. The Venezuelan International Meteorological and Hydrological Experiment (VIHMEX; Miller and Betts, 1977), the Convection Profonde Tropicale (COPT81) experiment (Sommeria and Testud, 1984), the Australian Monsoon Experiment (AMEX; Holland et al., 1986) and the Down Under Doppler and Electricity Experiment (DUNDEE; Rutledge et al., 1992) aided similar advances in the field of tropical continental convection. Observational gaps in the remaining tier of the triad of tropical convection -- island convection -- were partly filled by the Island Thunderstorm Experiment (ITEX; Keenan et al., 1989), winter monsoon experiment (winter MONEX; Houze et al., 1981), and the program on which this thesis is based, the Maritime Continent Thunderstorm Experiment (MCTEX) (Keenan et al., 1994b; 1996b).

Some of the deepest convection in the world occurs over the Indonesian archipelago, whose myriad islands serve as "hot plates" for the tropical atmosphere. Taken as a whole, this conglomeration of thunderstorm activity over the "maritime continent" (Ramage, 1968) approaches the spatial scale of the Rossby radius of deformation and provides primary forcing for the Hadley and Walker circulations (Krishnamurti et al., 1973; Janowiak et al., 1985; Rasmusson and Arkin, 1985). The amount of convective activity in this region is closely related to the El Niño-Southern Oscillation phenomenon and has been shown to influence the behavior of the subtropical jet on a daily basis (Lau et al., 1983). Additional studies provided evidence that these vigorous thunderstorms are central to maintaining the global electrical circuit (Williams et al., 1990; Rutledge et al., 1992), in addition to being a key component of the global circulation.

Influenced strongly by diurnal and coastal effects, thunderstorms occur regularly over Indonesia and tropical Australia. Over the Tiwi Islands, north of Darwin, in Australia's Northern Territory, intense convection is often spawned by a combination of land heating and sea breeze convergence. The MCTEX was designed to study this interaction on an intimate level in an effort to improve understanding of similar phenomena found over the hundreds of other islands dotted across the "maritime continent." As stated in the science plan (Keenan et al., 1994b), the MCTEX basic science objective was:

> *to improve knowledge of the dynamics and interaction of the physical processes involved in the organization and lifecycle of tropical island convection over the Maritime Continent and the role of this convection in the atmospheric energy and moisture balance.*

1.3 Sea breeze studies

The sea breeze plays a major role in the development of thunderstorms over the Tiwi Islands. Land heats up and cools down quicker than water due to its lower heat capacity. In the presence of significant solar heating and light-to-moderate environmental winds, a circulation develops that is transverse to the coastline which drives a shallow layer of oceanic air towards the island's interior due to the density difference between the hot air above the land surface and the relatively cool air above the water. This sea breeze front acts like a miniature cold front, lifting the convectively active boundary layer ahead of it and focusing cloud and shower development along its leading edge. In tropical regimes, sea breezes are especially robust and are often the primary impetus for deep convection.

For example, the Florida peninsula has been the site of numerous modeling and observational studies due to the reoccurring thunderstorms along its east and west sea breezes in the summertime (Simpson et al., 1975; Nicholls et al., 1991). Skinner and Tapper (1993) summarized the diurnal sea breeze circulation and surface radiation budget specific to the Tiwi Islands.

It is well established by various studies that the ambient wind direction modulates sea breeze intensity by sharpening or weakening the thermodynamic transition across the front, depending on whether the flow is against or with the sea breeze (Wexler, 1946; Pielke, 1974; Helmis, 1987; Atkins et al., 1995). When the gradient flow is on-shore, the oceanic air progresses inland relatively quickly with a diffuse boundary and weaker low-level convergence than when the ambient wind opposes the sea breeze. Cloud and thunderstorm development is therefore hindered along the windward-coast of the Tiwi Islands and enhanced along the leeward-coast sea breeze front. This was exemplified by the modeling work of Crook (1997a). In 3-D numerical simulations of 27 Nov. 1995 MCTEX convection, light northeasterly surface wind prompted initial development over the southwest coast sea breeze, consistent with observations. Additional simulations of 20 Nov. 1995 using low-level southwesterly wind showed initial convective development over the northeast quadrant of Melville Island, again, in agreement with observations (N. A. Crook, 1998, personal communication). Accordingly, a reliable predictor of initial thunderstorm development location during the MCTEX was the surface wind direction. The diurnal thunderstorms were usually triggered over the leeward half of the Tiwi Islands along the sea breeze front experiencing the best low-level convergence. This pattern was repeatedly demonstrated during the MCTEX, including the two case study days chosen for this thesis.

Wakimoto and Atkins (1994) and Atkins et al. (1995) found that horizontal convective rolls nearly parallel to the mean boundary layer wind direction modulated convection along the sea breeze front and led to periodic updraft enhancements where they intersected it. Sensitive radars have proven useful in identifying such low-level convergence features. Several studies have shown the applicability of these observations to predicting thunderstorm initiation, organization and lifetime (Wilson and Megenhardt, 1997; Wilson and Schreiber, 1986). Similar observations of low-level reflectivity thin lines and Doppler velocity gradients were made with the *C*-band (5.5-cm wavelength) *pol*arimetric (C-pol) radar in the MCTEX. These clear-air radar features, along with surface mesonet data, were used to locate sea breeze fronts, cold pool boundaries, and other boundary layer structures. As found by other authors (Schreiber, 1986; Wilson and Schreiber, 1986; Keenan et al., 1991), the meeting of a pre-existing cell with one or more of these boundaries often led to rapid cell intensification.

1.4 Lightning studies

Improved ground-based networks and new advanced satellites (Christian et al., 1989; Goodman, 1995) are providing new information on global lightning flash rates. Many scientists have turned their attention to this impressive source of data and found ways to incorporate it into rainfall measurements (Buechler et al., 1990; Williams et al., 1992; Shih, 1988; Petersen and Rutledge, 1998; Tapia et al., 1998), flash flood predictions (Holle and Bennett, 1997), and global weather prediction models (Puri, 1987). Petersen (1997) and Petersen and Rutledge (1998) demonstrated that under certain circumstances, the cloud-to-ground (CG) flash density of a convective system can be quantitatively related to the amount of rainfall produced, and that lightning observations should reveal the gross characteristics of a storm's vertical profile of heating and drying on a convective scale.

The MCTEX provided an opportunity to remotely sense the microphysical structure of tropical thunderstorms as they evolved from isolated warm-rain cells to multicellular deep convection, and finally to decaying stratiform precipitation. Each of these stages was captured with polarimetric radar, and inferences about storm electrification, intensity (Zipser and Lutz, 1994), and vertical profiles of latent heating (Houze, 1989; Petersen, 1997) for these different stages could be made.

Unlike most oceanic convection, continental and island convection is often characterized by considerable instability (Szoke et al., 1986; Keenan and Carbone, 1992) and is capable of generating strong updrafts that loft large quantities of supercooled water into the mixed-phase region (0 to -40°C). In their study of Florida thunderstorms during CaPE, Bringi et al. (1997) found Z_{DR} columns (polarimetric signatures produced by millimetric-sized raindrops above the freezing level) extending to 6 km AGL (-8°C) in strong updrafts. Additional polarimetric signatures above the columns indicated rapid development of mixed-phase conditions, initiated by freezing of lofted supercooled raindrops. Hubbert et al. (1998) found similar multiparameter radar patterns in a severe Colorado hailstorm.

It has been shown in laboratory studies that significant charge transfer can occur when millimeter-sized rimed targets (i.e. graupel) collide with smaller ice crystals (diameters of ~100 μm) in the presence of supercooled water droplets (Reynolds et al., 1957; Takahashi, 1978; Jayaratne et al., 1983; Saunders et al., 1991; Avila and Caranti, 1994; Baker and Dash, 1994). No ambient electric field is necessary. The sign and strength of this non-inductive charge (NIC) transfer is dependent on the temperature, ambient liquid water content, and relative velocity (size) of the particles. This process is proposed to be the dominant charging mechanism in lightning-producing cumulonimbus clouds by several authors (Illingworth and Latham, 1977; Takahashi, 1984; Ziegler et al., 1986; Randell et al., 1994; Williams, 1995). Modeling results have suggested that updrafts within tropical oceanic cells must be strong enough to support the lofting of liquid or frozen drops of ~1 mm diameter above the -10°C level to produce lightning via non-inductive charging (Zipser, 1994; Petersen, 1997). Further, a sufficient concentration of millimetric-sized frozen particles is considered necessary (1 L^{-1}) in order to generate significant cloud electrification (Takahashi, 1984). With the lightning flash data provided by the Advanced Lightning Direction Finder (ALDF) network and a flat plate antenna, CG lightning production and total storm flash rate were monitored for tropical island storms during the MCTEX. The polarimetric radar simultaneously collected information regarding the microphysical evolution of the storms, allowing a basic premise of NIC theory to be tested (i.e. that millimetric-sized ice in the mixed-phase region is a prerequisite for thunderstorm electrification). For the MCTEX case study days described below, the lightning flash rates were compared to the radar estimates of ice and water mass in the mixed-phase region of the storms. Hence, additional observational support for the NIC theory was produced.

If lightning flash rate could be linked to elevated ice production and stronger updrafts, then a storm's electrical activity could also shed light on its vertical distribution of latent heating, a crucial component of cumulus parameterization in global climate models (Brown and Bretherton, 1997), and an important factor in simulations of the Walker circulation (Hartmann et al., 1984) and the 30-60 day oscillation (Lau and Peng, 1987).

1.5 Case study days

Using satellite imagery from 1978-86, Keenan et al. (1990) found that during the November/December period, island thunderstorms formed over the Tiwi Islands on 65-90% of the days. Two island thunderstorm days during the MCTEX were selected for extensive study in this thesis. Both cases (23 and 27 Nov. 1995) were distinguished by strong diurnal convective storm complexes, typical for this transition time between the dry and wet seasons (Keenan et al, 1988), and provided ample opportunity to investigate lifecycle characteristics and organization of tropical island thunderstorms. 28 Nov. 1995 has already been investigated by Rutledge and Carey (1997) and Carey et al. (1997b)

Descriptions of the MCTEX electrical and radar data sets are found in Chapter 2, along with an overview of the editing and analysis methods. Chapter 3 summarizes the synoptic conditions for both case study days and details the initiation, organization, and evolution of each storm system. Polarimetric radar estimates of rainfall and ice mass aloft are provided in Chapter 4 and compared to measurements of cloud-to-ground (CG) lightning flash rate and total flash rate as detected by the ALDF network and flat plate antenna. Finally, Chapter 5 summarizes and discusses the results and includes inferences concerning cell evolution, rainfall estimates and storm electrification.

CHAPTER 2

Data and Methodology

This chapter describes lightning detection instruments used in the MCTEX and states the methods by which data were extracted and analyzed. An overview of the basic characteristics of the BMRC C-band polarimetric radar is provided, and the process of editing the data is discussed. Also included are brief descriptions of several polarimetric radar variables and their meteorological applications. Lastly, the actual algorithms used to obtain radar-derived quantities, such as rain mass flux and precipitation-sized ice mixing ratio are documented.

2.1 Flat plate antenna

A Colorado State University flat plate antenna was installed near the radar at Nguiu to detect all types of lightning flashes. This instrument sensed the electrostatic field changes associated with both CG and IC lightning discharges, allowing the total lightning flash rate to be obtained. It consisted of a disk-shaped conductor oriented with its long axis parallel to the ground. The disk was attached to a stand and inverted so that the housing for its electronics sheltered the metal disk from above. The electronics integrated the current flowing to the antenna plate and provided an output voltage proportional to the charge on the plate due to the ambient electric field (see Uman, 1987). The integrating capacitor C discharged through a relatively large resistor R so that the output voltage decayed toward zero with a time constant RC. In order to adequately capture the electrostatic field changes associated with lightning flashes, a time constant of 30 ms was used. Different gain settings were available in order to avoid voltage saturation from nearby flashes. However, for the majority of the experiment the flat plate antenna sampled with the high gain channel. Insensitive channels were rarely used. This resulted in a flash detection range of about 40 km.

An Analog-to-Digital (A/D) converter over-sampled the output voltage at 1 kHz in order to suppress sampling errors, and the signal strength in volts was stored on a personal computer (PC). The PC provided a time stamp from its internal clock and was periodically calibrated in order to correct a time drift of several seconds per day. Any error in this flat plate time stamp was insignificant when used in conjunction with radar data, which had a time resolution of 4-8 minutes.

Similar to previous studies (Carey and Rutledge, 1996; 1998) the flat plate antenna data were post-processed with an equally weighted, running mean filter specifically designed to eliminate a known noise source at 60 Hz. An absolute calibration of the antenna was not performed, so the voltage signal was not converted to electrostatic field strength. Instead, lightning flashes were identified by points where the signal-to-noise ratio of the voltage signal exceeded a predetermined threshold. The average "noise" level was obtained by sampling the antenna's voltage output during several fair weather days. Return strokes were handled by requiring 500 ms to pass before the next lightning signal could be considered a separate flash.

The flat plate did not perform well when rain fell on the device and short circuited the plate. This saturated the voltage readings and caused the calculated flash rate to escalate. This problem persisted until the flat plate dried out, so the flash rate was suspect during precipitation events at the site and for some time after the rain ceased. Usually the instrument was shut down before this occurred and it was occasionally manually dried so it would be operational again as quickly as possible.

2.2 Advanced Lightning Direction Finder (ALDF) network

Four National Aeronautics and Space Administration Marshall Space Flight Center NASA/MSFC Advanced Lightning Direction Finder (ALDF) sensors were stationed across the MCTEX analysis region. These sensors, developed by Global Atmospherics Inc. (GAI), detected the field strength, magnetic bearing, and arrival time of lightning-induced radio emissions, allowing the location and time of occurrence for lightning ground strikes to be retrieved. Similar to the devices described by Krider et al. (1976) and used in the National Oceanographic and Atmospheric Administration Forecasting System Laboratory (NOAA/FSL) network, these sensors consisted of a wideband system of two orthogonal magnetic loop antennas and a flat plate electric antenna. The detection efficiency of the NOAA/FSL DF's was estimated at 70-85% for ranges less than 100 km, so it is probably very similar for the sensors used in the MCTEX.

The accuracy of the derived stroke location depended on the stroke's proximity to the sensor baselines, the type of retrieval algorithm used, and the number of independent time of arrival/magnetic bearing measurements utilized by the retrieval algorithm. Koskak et al. (in review) demonstrated that more participating sensors and increased distance from baselines meant better stroke location accuracy. They tested various retrieval methods on sets of computer-generated lightning sources and found positioning errors ranging from 1 to 10 km over the Tiwi Islands. For this study, CG stroke locations and times of occurrence were supplied by the lightning group at MSFC. They provided several location solutions for each stroke based on different retrieval methods, but only the time and location derived by the most reliable method were chosen to represent the stroke.

These individual strokes were then grouped into flashes assuming that strokes occurring within a certain time interval and distance of each other belonged to the same flash. If two strokes were detected within 1 second and 20 km of each other, then they were considered to be part of the same flash. The total flash count was fairly insensitive to the chosen time interval, but slightly sensitive to the spatial requirements, due to the uncertainty of some flash locations derived from only two ALDF sensors.

2.3 C-pol radar

The Bureau of Meteorology Research Centre/National Center for Atmospheric Research (BMRC/NCAR) C-band (5.3-cm) polarimetric/Doppler radar system was used during the MCTEX (Keenan et al., 1998). This radar is capable of transmitting radiation of linear horizontal and vertical polarizations and receiving the co- and cross polarizations on a pulse-to-pulse basis. In addition to collecting the standard horizontal reflectivity (Z_h), radial velocity (V_r), and spectral width (σ_v) variables, C-pol also extracted differential reflectivity (Z_{DR}), 2-way total differential propagation phase shift (Ψ), and the coefficient of correlation at zero lag between the horizontally and vertically polarized backscattered echo ($|\rho_{hv}(0)|$). These polarimetric variables were obtained using the algorithms of Zahrai and Zrnic (1993). For a thorough discussion of polarimetric data, see Doviak and Zrnic (1993). The radar pulse repetition frequency (PRF) was 1000 Hz, and 128 samples (64 horizontal, 64 vertical interleaved) were collected for each gate.

2.3.1 Radar data quality control

Data were provided on dual-high density Exabyte tapes in a format designed by Lassen Inc. The radar had recently been upgraded to dual-polarimetric operation at the time of the MCTEX, and the new software used to archive the data labelled the azimuths incorrectly. Therefore, all radar volumes required a two-beam shift. Data recorded early in the experiment required an additional half-beam correction. Then it was converted to standard Universal Format (UF; Barnes, 1980). The UF fields were viewed and manipulated with radar editing software developed by NCAR (RDSS; Oye and Carbone, 1981).

It is well established that polarimetric radar measurements can recover rain rates with greater accuracy and consistency than with reflectivity alone. Sachidananda and Zrnic (1985) found that in order to estimate rain rate (R) more accurately than is possible with an ordinary $R(Z_h)$ relation, the errors in differential reflectivity Z_{DR} must be less than 0.1 dB, and errors in the reflectivity factor must be below 1 dBZ. For the purposes of this study, it was necessary to identify sub-quality polarimetric data and avoid including them in radar estimates of precipitation.

The coefficient of correlation at zero lag between the horizontally and vertically polarized backscattered echo (hereafter referred to as $|\rho_{hv}(0)|$) was used to determine which data points were suspect. $|\rho_{hv}(0)|$ is a function of the shape, oscillation, wobbling, and canting angle distribution of hydrometeors in the radar volume (Sachidananda and Zrnic, 1985). Furthermore, $|\rho_{hv}(0)|$ is dependent on the breadth of the drop axis-ratio distribution (Jameson, 1987; Jameson and Dave, 1988) and is lowered where there is a broad range of hydrometeor types [such as in the mixed-phase region at the base of the melting layer (Zrnic et al., 1993), or in regions of wet hail]. Sachidananda and Zrnic (1985) showed theoretically that in pure rain, shape effects only reduced $|\rho_{hv}(0)|$ to 0.99, but canting angle variations and noise acted to reduce the correlation to about 0.98 in actual observations of pure rain. They indicated a further drop in $|\rho_{hv}(0)|$ in lower reflectivities, possibly due to sidelobes and receiver noise (as mentioned by Doviak and Zrnic, 1993). The variances of Z_{DR} (Sachidananda and Zrnic, 1985) and Ψ (Zrnic, 1977) are both inversely related to $|\rho_{hv}(0)|$. Therefore, where $|\rho_{hv}(0)|$ was very low (below 0.7), Z_{DR} and Ψ were judged to be statistically unreliable and were not used in any radar analyses. This eliminated noisy polarimetric data associated with low SNR occurring in clear air or along the periphery of precipitation echoes. Noisy polarimetric data were also eliminated where fluctuations in differential phase shift upon backscattering (δ) reduced $|\rho_{hv}(0)|$ (Doviak and Zrnic, 1993). Large values of δ were observed in some of the newly developed precipitation cores sampled during the MCTEX. These cores had very high Z_{DR} values (>4 dB), and likely contained very large raindrops that violated Rayleigh scattering assumptions. Rayleigh assumptions require particle diameters to be less than $\lambda/16$, where λ is the radar wavelength. For C-band, the transition from Rayleigh scattering to Mie scattering occurs around 3.4 mm. C-band radar is therefore vulnerable to Mie scattering effects from large raindrops. This is especially true in the tropics, where large raindrops are not uncommon. The $|\rho_{hv}(0)|$ threshold helped to eliminate some noisy polarimetric data where Mie scattering likely occurred.

The 2-way total differential propagation phase shift (Ψ) at range r_0 is composed of three terms:

$$\begin{aligned} \Psi &= 2\int_0^{r_0}\left[k_h(r)-k_v(r)\right]dr+\delta(r_0)+\phi_0 \\ &= \qquad \phi_{DP} \qquad + \ \delta \ + \phi_0 \ , \end{aligned} \tag{2.1}$$

where k_h and k_v are the increments (for horizontal and vertical polarizations) to the free space propagation constant due to the presence of hydrometeors, r the radar range, δ the differential phase shift upon scattering (Doviak and Zrnic, 1993), ϕ_0 the system phase (known), and ϕ_{DP} the propagation differential phase shift. Wind tunnel experiments have shown that raindrops larger than 1 mm diameter falling at terminal velocity deform into oblate spheroids with their major axis preferably aligned in the horizontal (Pruppacher and Beard, 1970). As radar electromagnetic waves having different polarizations propagate through a collection of non-spherical hydrometeors, a phase difference develops between the waves. Oblate raindrops, or any similarly shaped anisotropic scatterer, have more dielectric area in the horizontal plane than in the vertical plane, so a horizontal linearly polarized wave propagating through a population of oblate raindrops experiences greater phase shift than a vertical linearly polarized wave propagating through the same collection of raindrops [i.e. $k_h(r)>k_v(r)$]. This means that the first term in eqn. 2.1 (i.e. ϕ_{DP}) is positive whenever the radar beam propagates through oblate raindrops. It is a range-cumulative term and is proportional to the mass-weighted mean oblateness of the precipitation particles between the radar and range r_0. The second term, the backscatter differential phase shift (δ), is zero for Rayleigh targets, but can be appreciable where Mie scattering occurs. This term contributes high frequency "noise" to the steady upward trend of Ψ with increasing range, but can be separated from Ψ with an appropriate filter. The system phase (ϕ_0) was 0°.

The 2-way total differential propagation phase shift (Ψ) was recorded in units of degrees such that $-32° < \Psi < +32°$. The values were "folded" (aliased) if the actual Ψ extended beyond these boundaries (e.g. +33° was folded to -31°). Using RDSS, Ψ data were manually unfolded so that they could be used in various radar algorithms. This field must be unfolded before calculating specific differential phase shift (K_{DP}). Heavy rain along several radar beam paths resulted in $\Psi > 110°$ and required a triple unfolding of the raw data! Most noisy Ψ data around the edges of precipitation echoes were removed by the $|\rho_{hv}(0)|$ thresholding process, but some Ψ perturbations persisted in the interior of heavy rain shafts. This was probably where raindrops were so large that δ became a significant contributor to Ψ.

Once Ψ was unfolded, ground clutter needed to be suppressed. Echoes close to the radar due to tall trees and ridges generated a reflectivity pattern at low elevation angles that could affect precipitation estimates. The severity of the ground clutter was highly sensitive to the radar beam elevation angle. A simple reflectivity-rain rate (Z_h-R) estimator applied to the ground clutter reflectivity pattern revealed significant contributions to the estimated rain mass flux from these non-precipitation echoes. Ground clutter was removed by delineating the region in RDSS, and eliminating Z_h, Z_{DR}, and Ψ at gates within the delineated region where radial velocity equalled zero or ± 13.69 m s^{-1} (the velocity folding, or Nyquist interval).

This method was effective and accurate if care was taken to avoid removing real precipitation echoes. (This could happen if actual precipitation exhibited a radial velocity of either 0 m s^{-1} or $\pm$13.63 m s^{-1} within the delineated boundary.) For most radar scans, this was not a concern since the areal coverage of the ground clutter was small and precipitation rarely interfered. Second-trip echoes were removed in similar fashion.

Horizontal reflectivity was corrected for gaseous attenuation in accordance with Battan (1973, see Fig. 6.1 therein), where

$$\text{corrected } Z_h = \text{observed } Z_h + \left(0.008 \cdot 2 \cdot \textit{slant range}\right) \ [dBZ] \ . \qquad (2.2)$$

The correction was small, and only reached 2.4 dBZ at 150 km. For wavelengths longer than 3 cm, the major attenuation of a radar signal is due to hydrometeors, with only minor effects from atmospheric gases (Hitschfeld and Bordan, 1954).

2.3.2 Calculating specific differential phase shift (K_{DP})

A 13-point running-mean filter was applied to the Ψ data to estimate the propagation differential phase shift (ϕ_{DP}) along each ray. Most precipitation is either oblate or quasi-spherical, so ϕ_{DP} almost invariably monotonically increases with range. However, what the radar actually measured was Ψ, the total 2-way differential phase shift. As mentioned earlier, Ψ is the sum of ϕ_{DP} and the backscatter differential phase shift (δ) after removal of the system phase offset. Due to resonance effects, δ can be non-zero for large scatterers. This can create erratic excursions in Ψ when interrogating extremely large raindrops. The 13-point running mean filter smoothed Ψ, minimizing the influence of noise and differential backscatter. This preserved the physically meaningful trend associated with ϕ_{DP} and allowed specific differential phase shift (K_{DP}) to be calculated by taking the range derivative of ϕ_{DP} using a simple finite difference method. The backscatter differential phase shift (δ) was backed out using the relation

$$\delta = \Psi - \phi_{DP} \quad . \tag{2.3}$$

Ψ is not reliable in light precipitation, so K_{DP} was only calculated at gates where Z_h>30 dBZ.

Specific differential phase K_{DP} is only affected by anisotropic hydrometeors and has been shown to be the product of the precipitation liquid water content and the mass-weighted mean axis ratio of the raindrops (Jameson, 1985). Isotropic (spherical) hydrometeors produce equal phase shifts for either polarization, so the phase difference is due largely to the anisotropic constituents of the medium. For example, if statistically isotropic hail is mixed with rain, K_{DP} is mainly affected by the raindrops. Balakrishnan and Zrnic (1990) used this property to separate the portion of the reflectivity factor due to rain from the portion due to hail. They used an empirical K_{DP}-R relationship to obtain R, and then with an appropriate Z_h-R relationship, estimated the reflectivity due solely to rain. Subtracting the rain reflectivity from the total reflectivity [mm^6 m^{-3}] yielded the isotropic hydrometeor contribution to reflectivity (produced mainly by hail).

K_{DP} has also been used for robust and accurate estimates of heavy rainfall (>60 mm hr^{-1}) by Chandrasekar et al. (1990). K_{DP} estimates hold several advantages over reflectivity-only estimates because 1) K_{DP} is independent of receiver/transmitter calibration, 2) insensitive to partial beam filling, 3) independent of attenuation, 4) relatively insensitive to drop size distribution (DSD), and 5) not biased by the presence of hail (Chandrasekar et al., 1990).

2.3.3 Converting radar volumes from polar to Cartesian coordinates

Before proceeding with radar analyses, C-pol data was interpolated to a Cartesian grid with the origin at the radar site. This was done with the National Center for Atmospheric Research REORDER software package. The horizontal grid spacing was 1 km and the vertical spacing was 0.5 km. A Cressman weighting function (Cressman, 1959) was used with radii of influence proportional to range. This accounted for the decreasing spatial resolution of radar data away from the grid origin.

2.3.4 Precipitation attenuation correction

One of the trade-offs to using a small wavelength radar is increased attenuation. The C-pol 5-cm radar is more portable and less expensive to operate compared to the NCAR 10-cm S-pol radar, and its smaller wavelength theoretically allows better resolution of propagation differential phase shift. However the C-band system is much more susceptible to attenuation. This must be accounted for when estimating rain rate with horizontal reflectivity or differential reflectivity. When a radar pulse intercepts precipitation, it loses power to absorption and scattering. The specific attenuation expressed in dBZ km^{-1} is

$$A_h = 4.34 \times 10^3 \int_0^\infty N(D)\ \sigma_e(D)\ dD = A_h(absorption) + A_h(scatter) \quad , \tag{2.4}$$

where N(D) dD is the number of hydrometeors per unit volume having diameters in the interval between D and D+dD, and $\sigma_e(D)$ is the extinction cross section (Doviak and Zrnic, 1993). At centimeter wavelengths, A_h(absorption) dominates for all rain rates (Fig. 8.12, Doviak and Zrnic, 1984). There is no easy solution to eqn. 2.4, so investigators have resorted to numerical methods using full electromagnetic scattering theory and specified DSD's to study A_h.

Polarimetric measurands are also adversely affected by attenuation. Since raindrops are oblate, more attenuation occurs in a horizontally polarized signal than in a vertically polarized signal. The effects of differential attenuation (A_{hv}) on differential reflectivity (Z_{DR}) can be quite large at C-band, and left uncorrected, will certainly bias estimations of rain rate (Aydin, 1992). Scarchilli et al. (1993) studied the variability of A_h and A_{hv} as a function of rainfall rate at C-band frequencies. Their results showed that specific attenuation rates could be as high as 0.5 dB km^{-1} and A_{hv} could reach 0.15 dB km^{-1} in heavy rain.

Hildebrand (1978) described an attenuation correction procedure for reflectivity (Z) based on an empirically derived Z-A_h relationship. The relationship was only appropriate for a specific temperature and DSD and required a properly calibrated radar. The observed reflectivity factor (Z_{obs}) was converted to attenuated rainfall rate and then to an attenuation estimate. The new estimate of reflectivity factor (Z') was then produced by adding the integrated attenuation between the radar and the point of interest to the observed attenuated reflectivity factor, Z_{obs}. If the revised reflectivity factor estimate (Z') was used to derive revised attenuation estimates, then another set of reflectivity factor estimates could be obtained, Z''. This iterative procedure could be repeated until successive iterations did not produce a significant change in the estimated total attenuation along the radar beam. Hildebrand (1978) noted that in cases where the attenuation correction produced an overestimate of attenuation, the attenuation estimates diverged after several iterations. In these cases the iteration process was restarted and halted after only a few iterations. Hildebrand (1978) also found that radar calibration errors had a larger effect on attenuation estimates than errors in the Z-A_h relationship, and he suggested that a dense rain gauge network used in conjunction with the radar was the most viable method of obtaining precipitation estimates from radar reflectivity factor alone. This iterative correction procedure did not perform well when radar calibration errors were larger than the attenuation corrections, or when dealing with storms having reflectivity maxima greater than 60 dBZ (Hildebrand, 1978). The absence of a unique relation also made the Z-A_h relation difficult to use in practice (Aydin et al. 1989). In a related study, Aydin et al. (1989) introduced an attenuation correction procedure for dual-polarized radars parameterizing the ratio of specific attenuation and reflectivity factor (A_h/Z) in terms of Z_{DR}.

An alternative attenuation correction method that uses differential phase ϕ_{DP} was proposed by various investigators (Bringi et al., 1990; Jameson, 1992; Scarchilli et al., 1993) and is the method chosen for this study. This recent interest was fueled by the finding that specific attenuation (A_h) and specific differential attenuation (A_{hv}) are approximately linearly proportional to the specific differential phase shift (K_{DP}) at weather radar wavelengths (Bringi et al., 1990):

$$A_h \approx a \cdot K_{DP} \tag{2.5a}$$

$$A_{hv} \approx b \cdot K_{DP} \; . \tag{2.5b}$$

Unlike the previous methods, this correction procedure does not depend on the actual rain rate profile between the radar and the target.

The change in Z_h and Z_{DR} due to attenuation can be expressed as integrations of the specific attenuation and specific differential attenuation, respectively, over a propagation path:

$$\Delta Z_h = -2\int A_h \, dr \tag{2.6a}$$

$$\Delta Z_{DR} = -2\int A_{hv} \, dr, \tag{2.6b}$$

and the propagation differential phase shift as an integral of K_{DP}:

$$\phi_{DP} = 2\int K_{DP} \, dr. \tag{2.7}$$

Substituting eqns. 2.5a and 2.5b into eqns. 2.6a and 2.6b reveals both the relationship between the incremental reflectivity loss due to attenuation (ΔZ_h) and ϕ_{DP} and the similar relationship between ΔZ_{DR} and ϕ_{DP}:

$$\Delta Z_h = -a \cdot \phi_{DP} \tag{2.8a}$$

$$\Delta Z_{DR} = -b \cdot \phi_{DP} \; . \tag{2.8b}$$

Now consider these definitions for the intrinsic reflectivity and intrinsic differential reflectivity (unmodified by propagation effects):

$$Z_h^{observed} = Z_h^{\text{intrinsic}} - a \cdot \phi_{DP} \tag{2.9a}$$

$$Z_{DR}^{observed} = Z_{DR}^{\text{intrinsic}} - b \cdot \phi_{DP} \quad . \tag{2.9b}$$

If we differentiate eqns. 2.9a and 2.9b with respect to ϕ_{DP}, we see that a and b are each composed of two terms (using finite difference notation):

$$a = \frac{\Delta Z_h^{\text{intrinsic}}}{\Delta\phi_{DP}} - \frac{\Delta Z_h^{observed}}{\Delta\phi_{DP}} \tag{2.10a}$$

$$b = \frac{\Delta Z_{DR}^{\text{intrinsic}}}{\Delta\phi_{DP}} - \frac{\Delta Z_{DR}^{observed}}{\Delta\phi_{DP}} \quad . \tag{2.10b}$$

Now if we ignore the intrinsic variation of Z_h and Z_{DR} with respect to ϕ_{DP} (i.e. assume the first terms on the right sides of eqns. 2.10a and 2.10b are zero) then we can estimate a and b by analyzing actual radar observables. With ϕ_{DP} and our estimates of a and b, the corrected Z_h and Z_{DR} can be obtained from

$$Z_h^{corrected} = Z_h^{observed} + a \cdot \phi_{DP} \tag{2.11a}$$

$$Z_{DR}^{corrected} = Z_{DR}^{observed} + b \cdot \phi_{DP} \quad . \tag{2.11b}$$

The polarimetric radar volumes for our MCTEX case study days were corrected for precipitation attenuation in this manner. To estimate a, a linear regression was performed on Z_h and ϕ_{DP} for each polarimetric radar volume. All eligible data points between 0.5 and 2 km AGL, inclusive, were used. Care was taken to avoid intrinsic variation of Z_h and Z_{DR} with respect to ϕ_{DP}. Similar to the strategy used by Ryzhkov and Zrnic (1995b), only points where $1<K_{DP}<2^\circ$ km^{-1} were used. But as Carey et al. (1997a) demonstrated, further restrictions improved the quality of the linear regression data. In addition to falling within the prescribed K_{DP} boundaries, all points must have had $|\rho_{hv}(0)|>0.95$, and $|\delta|<5°$. These extra tests better isolated rain and eliminated points with noisy data and/or Mie scattering. The radar volumes with the greatest coverage of moderate or heavy rain offered the most reliable linear regressions due to the high number of qualified samples. For radar volumes near the beginning or end of the storm's convective life-cycle, the number of samples was severely reduced and this sometimes resulted in unreliable or physically unrealistic estimates (less than zero) of *a* or *b*. If the estimate of *a* or *b* was negative, or if fewer than 100 samples were used in the regression analysis, or if the coefficient of determination (R^2) was too low, then that particular *a* or *b* value was not used to correct the radar volume. Instead, an average value of *a* or *b* was used in its place. The requirement for *a* was $R^2>0.15$, and for *b* $R^2>0.25$. The average values of *a* and *b* for 23 Nov. and 27 Nov. are shown in Table 2.1 along with values derived from theory and estimated by Carey et al. (1997a) for 28 Nov. 1995.

Table 2.1 Comparison of a's and b's

	a [dBZ per deg of phase shift]	b [dB per deg of phase shift]
23 Nov. 1995	0.056-0.174 (mean: 0.09)	0.013-0.030 (mean: 0.022)
27 Nov. 1995	0.077-0.214 (mean: 0.14)	0.015-0.032 (mean: 0.022)
28 Nov. 1995 (Carey et al., 1997a)	0.057-0.159 (median: 0.091)	0.012-0.031 (median: 0.018)
Theory (Keenan et al., 1997)	0.047-0.075	0.006-0.016

The variance of *a* and *b* depended on (a) DSD fluctuations, (b) variability in the estimate of ϕ_{DP} due to normal radar measurement variance, and (c) nonzero values of δ (Bringi et al., 1990).

Figs. 2.1 and 2.2 show rain mass flux estimates versus time (UTC time is 9.5 hours behind local standard time) for 27 Nov. before and after correcting for precipitation attenuation. Fig. 2.1 suggests that precipitation attenuation accounted for a ~50% drop in the estimated total rain mass flux when using Z_h alone to estimate rain rates. On the other hand, Fig. 2.2 shows the relative insensitivity of an $R(K_{DP})$ estimator to precipitation attenuation.

Rain mass flux estimates that relied heavily on the $R(K_{DP},Z_{DR})$ algorithm were similar to those that relied on $R(K_{DP})$. After correcting for differential attenuation, the estimated rain mass flux based on the $R(K_{DP},Z_{DR})$ algorithm dropped slightly and fell below values estimated with $R(K_{DP})$. Higher Z_{DR} implies a lower rain rate, assuming the other radar parameters remain unchanged. Over the entire storm, the change was not great, and the shape of the rain mass flux curve remained the same. This will be discussed below in Chapter 4.

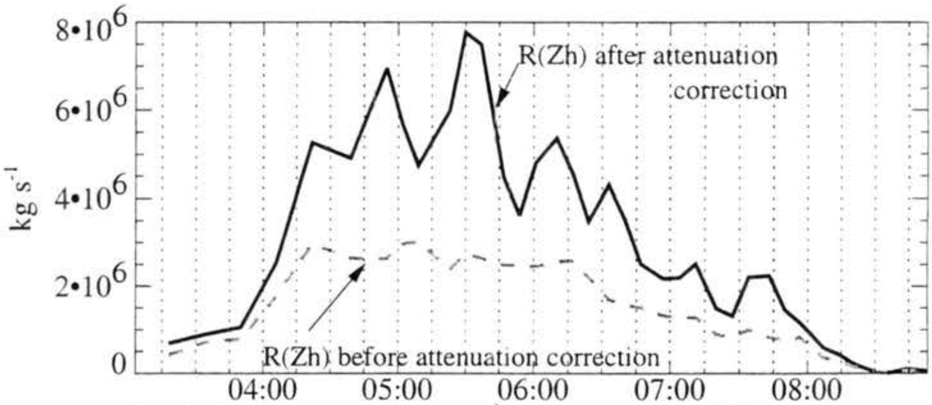

Fig. 2.1 Time series of total island rain mass flux [kg s^{-1}] at 1 km AGL for 27 Nov. 1995. Rain mass flux was derived from the $R(Z_h)$ relationship (eqn. 2.12d). Dashed gray line is *before* precipitation attenuation correction (as described in section 2.3.4) and black line is *after* precipitation attenuation correction. For this figure and in all subsequent figures, times are in UTC, unless otherwise noted.

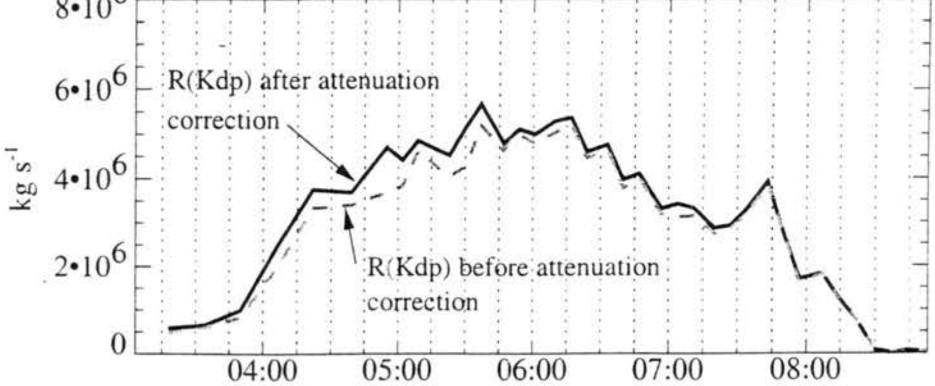

Fig. 2.2 As in Fig. 2.1 except for the $R(K_{DP})$ relationship.

2.3.5 Quantitative estimates of liquid and frozen precipitation

Electromagnetic scattering theory was applied to disdrometer data collected during the MCTEX to produce four different rain rate (R) relationships with Z_h, K_{DP} and Z_{DR}:

$$R(K_{DP}, Z_{DR}) = 25.00(K_{DP})^{0.988}(Z_{DR})^{-0.585} \quad (2.12a)$$

$$R(Z_h, Z_{DR}) = 0.00177(Z_h)^{0.979}(Z_{DR})^{-1.279} \quad (2.12b)$$

$$R(K_{DP}) = 23.37(K_{DP})^{0.82} \quad (2.12c)$$

$$R(Z_h) = 0.00596(Z_h)^{0.862} \quad (2.12d)$$

with R in mm hr^{-1}, K_{DP} in deg km^{-1}, Z_{DR} in dB and Z_h in mm^6 m^{-3}.

Natural raindrop size spectra N(D) have successfully been fitted to both exponential functions (e.g. Marshall and Palmer, 1948)

$$N(D) = N_0 \exp\left(-3.67\frac{D}{D_0}\right) \quad (2.13)$$

and general gamma distributions (Ulbrich, 1983)

$$N(D) = N_0 D^{\mu} \exp\left[-(3.67+\mu)\frac{D}{D_0}\right], \quad (2.14)$$

where D_0 is the median-volume diameter and $-3<\mu<8$. The multiple parameters contained in these functions (N_0, D_0, and μ) are better replicated by utilizing more than one remotely sensed measurand. Theoretically, assuming no radar calibration issues, eqns. 2.12a and 2.12b can more faithfully retrieve the actual rain drop-size distributions because they use more than one measurand. More accurate DSD estimates improve rain rate estimates. Therefore, to construct rain rate fields, 2.12a was first used on all grid points where K_{DP} and Z_{DR} both exceeded the noise level (i.e. $K_{DP}>0.25$ deg km^{-1}, $Z_{DR}>0.5$ dB, $Z_h>0$ dBZ) and represented a realistic DSD (if K_{DP} was high, then Z_{DR} must have been high). Then 2.12b was applied to the remaining points where Z_{DR} was large enough (>0.5 dB). But if neither of these equations applied, and K_{DP} was still above 0.25 deg km^{-1}, then 2.12c was used. This left the remaining points with any reflectivity to be evaluated with 2.12d. About three fourths of the rain mass flux was estimated by 2.12a, with 2.12b and 2.12c responsible for the other fourth.

The rain fields created via this method were compared to rain fields created via a "$R(K_{DP})$" method. Only $R(K_{DP})$ and $R(Z_h)$ were used for the "$R(K_{DP})$" method. In this case, all points where $K_{DP}>0.25$ deg km^{-1} utilized $R(K_{DP})$. Otherwise $R(Z_h)$ was applied.

Polarization diversity techniques for estimating rain rate have been explored by a number of investigators. Specific differential phase shift (K_{DP}) has been shown to be superior to using the reflectivity factor-rain rate $R(Z_h)$ relation alone (Zrnic and Ryzhkov, 1996; Ryzhkov et al., 1997). The same can be said for differential reflectivity-based methods $R(Z_h, Z_{DR})$ (Aydin et al., 1987; Gorgucci et al., 1994). At high rain rates, Chandrasekar et al. (1990) demonstrated that K_{DP} was more accurate than the estimator that used Z_h or Z_{DR}. This was especially true in the presence of hail (Zrnic and Ryzhkov, 1996; Hubbert et al., 1998; Balakrishnan and Zrnic, 1990).

Rain and precipitation-sized ice reflectivities were partitioned at all vertical levels using *difference reflectivity*, Z_{DP}. Z_{DP} was first proposed by Golestani et al. (1989) to deal with mixed-phase precipitation. It is defined as 10 times the logarithm of the difference (in $mm^6\ m^{-3}$) between the reflectivity factors at horizontal Z_h and vertical polarization Z_v:

$$Z_{DP} = 10\ \log_{10}\left(Z_h - Z_v\right)\ , \tag{2.15}$$

where $Z_h > Z_v$. This discrimination method assumes that ice particles (e.g. graupel, hail, large aggregates, frozen raindrops) are quasi-spherical and thereby contribute equally to both Z_h and Z_v. Any contribution to Z_{DP} must be from oblate hydrometeors (i.e. rain). Even if the frozen hydrometeors were not perfectly spherical, these deviations are mitigated by the fact that the dielectric constant of ice is significantly lower than that of water. This further diminishes the impact of ice on the difference reflectivity calculations. Golestani et al. (1989) discovered a nearly linear relationship between Z_{DP} and $Z_{h,rain}$ for simulated gamma drop-size distributions:

$$Z_{DP} = 1.2(Z_{h,rain}) - 15.4\quad [dBZ]\ . \tag{2.16}$$

If we apply this relationship to a radar volume containing mixed-phase hydrometeors, the observed difference reflectivity determines the reflectivity due solely to rain ($Z_{h,rain}$). The reflectivity due to ice ($Z_{h,ice}$) can be isolated by taking the difference between the observed Z_h and $Z_{h,rain}$.

To estimate the linear relationship between Z_{DP} and rain reflectivity $Z_{h,rain}$ in *this study*, a least-squares line was fit to Z_{DP} and $Z_{h,rain}$ data pairs using C-pol data from low levels of the storm. Since hail is rarely observed at the surface in the tropics, these regions were almost certainly free of ice. This yielded the following empirical relationship for the MCTEX:

$$Z_{DP} = 1.30(Z_{h,rain}) - 18.2 \quad , \qquad (2.17)$$

with Z_{DP} in dB and $Z_{h,rain}$ dBZ. Similar calculations by Carey and Rutledge (1996) for an S-band radar in a multicellular storm in Colorado led to a slope of 1.10 and an intercept of -9.36. Conway and Zrnic (1993) derived 1.13 and -9.1, respectively. Note that the MCTEX relationship was different from the relationship derived by Golestani et al. (1989) and these other investigators. This could be due to different radar calibration and/or drop-size distributions and/or radar wavelengths.

In this study, the reflectivity due to ice hydrometeors and due to liquid hydrometeors was calculated at all points where Z_{DR}>0.5 dB and Z_h>35 dBZ.

Once the ice reflectivity ($Z_{h,ice}$) was determined it was used to estimate the precipitation-sized ice mixing ratio (M_{ice} in g kg^{-1}) using eqn. 2.18:

$$M_{ice} = 1000\pi \frac{\rho_i}{\rho_a} N_0^{3/7} \left(5.28 \times 10^{-18} \frac{Z_{h,ice}}{720} \right)^{4/7} , \qquad (2.18)$$

where ρ_i is ice density (917 kg m^{-3}, the density of solid ice was used since no in-situ ice density measurements were available), ρ_a is air density [kg m^{-3}], N_0 is the intercept parameter of an assumed inverse exponential particle size distribution [4×10^6 m^{-4} taken from Petersen (1997) who simulated MCTEX island convection with a 1-D microphysical model], and $Z_{h,ice}$ is in mm^6 m^{-3}. The total reflectivity was used to decide whether the ice was primarily large ice particles such as graupel, frozen drops and large aggregates, or primarily ice crystals and small aggregates. If Z_h<35 dBZ the reflectivity was attributed to small ice particles, and if Z_h>35 dBZ the reflectivity was assigned to graupel. Graupel particles tend to be larger than other ice crystals and snow aggregates, so they are much more reflective. This partitioning stategy led to two distinct modes of ice. As will be shown in Chapter 4, the graupel mass was well correlated with lightning flash rates. The small ice particle mass peaked at later times and was not as strongly related to electrical activity. This electrical corroboration lends credence to the ice partitioning method.

Standard residual errors in dual-polarization measurands can lead to unrealistic partitioning of ice and rain, especially near the surface (L. Carey 1998, personal communication). In the tropics it is very uncommon to have frozen precipitation reach the ground due to the height of the melting level. Therefore, if the radar suggested ice below the melting level, the numbers were checked to make sure the ice reflectivity signal was above a certain threshold. This threshold was a product of *mf* and the standard residual error (~1.3 dBZ), where *mf* was directly proportional to the vertical distance from the melting level. The greater the separation between the melting level and the grid point, the greater the threshold. If the estimated ice reflectivity was less than this threshold, then 100% of the reflectivity was attributed to water. Similarly, when the radar depicted liquid water above the freezing level, the liquid water signature must have been above the threshold, or else all reflectivity was attributed to ice. Near the melting level, the threshold was a mere 1.3 dBZ since it is not all that unlikely to have transient penetrations of liquid water above the freezing level or to have ice below it, especially in turbulent thunderstorms. The requirements for detecting precipitation of the unlikely phase (i.e. ice below the melting level or liquid above the melting level) became more stringent as one moved away from the 0°C level (at the surface, the threshold was 8.2 dBZ).

Precipitation-sized liquid water content (M_{water} in g kg^{-1}) was computed directly from K_{DP}:

$$M_{water} = 0.8757(K_{DP})^{0.739} \quad . \tag{2.19}$$

This relationship was based on theoretical scattering calculations derived from MCTEX disdrometer data. Another method based on $Z_{h,water}$ was also tested, but led to no significant changes in total liquid water mass over the entrire storm.

CHAPTER 3

Convective Organization

An overview of the convective evolution for the two MCTEX case study days follows. First, a brief description of the Tiwi Islands is provided along with a general climatology of the region. Important aspects of island convection are described, and several issues raised by previous investigators are brought forth. Next, we provide a synoptic overview of the 23 Nov. and 27 Nov. case study days, and detail the convective development for each day. These observations are compared to past studies and the extent to which they support established theories and conceptual models is discussed.

3.1 Description of study area

3.1.1 Tiwi Islands

The Tiwi Islands are located approximately 50 km north of Darwin, Australia, in the extreme southeastern tip of the "maritime continent" (Ramage, 1968). The Tiwi's are comprised of two islands separated by a narrow tidal channel which runs from northwest to southeast (see Fig. 3.1). Bathurst Is. is the smaller of the two and is situated to the west of Melville Is. Together, they stretch about 150 km from east to west and 65 km north to south. Vegetation consists primarily of open eucalypt forest with some mangroves around the estuaries along the northern coast. Also, some pine plantations can be found in west central Melville Is. (Keenan et al., 1996b). Close to the southern coast of Melville Is., a narrow ridge 50 - 100 m above sea level roughly parallels the coast, and to the north, the topography gradually descends to the sea. The land is part of a reserve controlled by the Tiwi Land Council and is mostly unpopulated (Keenan et al., 1996b).

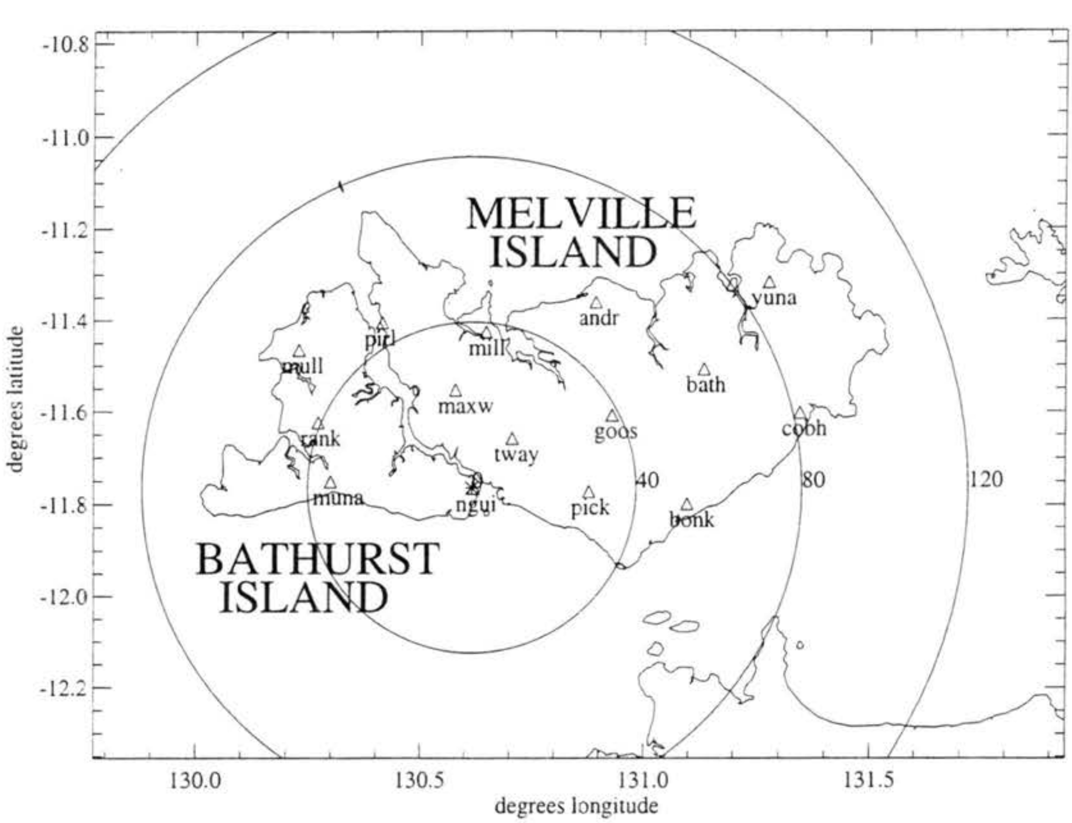

Fig. 3.1 Map of Tiwi Islands with range rings [km] centered on the C-pol radar location (asterisk). Also included are locations (triangles) and names of automated weather stations (AWS).

3.1.2 Climatology

During the austral winter the Intertropical Convergence Zone (ITCZ) is situated to the north of the islands and southeasterly winds from the Australian continent advect dry air over the islands and suppress precipitation. Typically, by November or December, the equatorial trough migrates southward enough to influence northern Australia, and the moist unsettled weather associated with the monsoon trough eventually dominates the region. Hence, the islands experience pronounced wet and dry seasons. Less than 10% of the annual rainfall occurs from May through October when the average 0900 LST wet-bulb temperature is 22°C and the monthly rainfall is 15 mm over northwest Melville Island. At the same location, from

December through March, the average morning wet-bulb temperature increases to 26°C and the monthly rainfall jumps to 370 mm (Bureau of Meteorology, 1998). Monsoonal bursts of deep westerly flow to 400 mb occur during this period. These westerly periods usually last less than a month and are commonly interrupted by "breaks" in which the low to mid-level flow shifts to drier easterlies. These westerly events are associated with easterly propagation of periodic Madden-Julian oscillations (Madden and Julian, 1994). Widespread stratiform precipitation with embedded convection in the monsoonal periods gives way to a greater concentration of diurnal convective cloud complexes, including island thunderstorms. These "break" periods are climatologically similar to the pre-monsoonal "transition" period that occurs towards the end of the dry season before the austral summer monsoon establishes itself across northern Australia. It is during this "transition" period that the MCTEX was conducted. Increasing sun angle and a shift to easterly low- to middle-level flow of subtropical origin combine to produce island thunderstorms between 65-90% of these days (Keenan et al., 1990). Simpson et al. (1993) analyzed vertical thermodynamic soundings from Darwin and found that day-to-day variation in the profiles of temperature and humidity was remarkably small. They found that the most variation occurs in the dew point temperatures above 800 mb, and that these fluctuations were mostly the result of differences in ambient moisture between the drier, undisturbed monsoon-break conditions and the wetter, disturbed monsoon-approach environment. They also correlated the undisturbed monsoon-break conditions with a higher ratio of convective versus stratiform rainfall (Simpson et al., 1993).

3.1.3 Convective initiation

A typical morning sounding from the MCTEX is shown in Fig. 3.14. With such a high dew point, the air temperature cannot drop very far before it reaches saturation. This was manifested in the formation of light radiation fog observed over the islands some mornings (L. Carey, 1998, personal communication).

By early afternoon, the island environmental sounding typically showed a well-mixed adiabatic layer extending from near the surface to 1-2 km AGL. The boundary layer depth over the islands is more representative of oceanic soundings than continental soundings (Riehl, 1979). Over continental regions, where a larger fraction of solar energy is converted to sensible heating, one often finds a much deeper mixed-layer. Superadiabatic conditions often exist near the surface, and large evapotranspiration rates lead to a tight downward-directed moisture gradient over the Tiwi Islands. Near 800 mb, evidence of a moist cloud layer capped by the trade inversion often is found. As mentioned by Keenan et al. (1994a), this structure is typical of a planetary boundary layer affected by broken shallow inversion-capped cumulus.

Before significant convection can occur, the mixed-layer must be deep enough and moist enough to provide an adequate supply of moist static energy to developing updrafts. These air parcels must overcome entrainment and break through the trade inversion to reach their level of free convection (LFC) and accelerate upward. Simpson et al. (1993) showed that a large portion of the surface energy flux must go into latent heating of the sub-cloud mixed-layer. This moistening required much more time and energy than the required sensible heating of the mixed-layer, and Simpson et al. (1993) stressed the importance of evapotranspiration. The observed low cloud bases and estimated high precipitation efficiency of ITEX thunderstorms supported findings that the Bowen ratio (ratio of latent heat flux to sensible heat flux) was similar to that over open ocean (Simpson et al., 1993).

Thunderstorm development early in the monsoon transition season is often suppressed due to weak evapotranspiration. A study by Simpson et al. (1993) suggested that ventilation of the sub-cloud layer by surface winds above 5-7 m s^{-1} also suppressed development of deep convection. With high winds, the residence time of air over the island is too brief to create the deep mixed-layer necessary for precipitating cumulus.

The C-pol radar was sensitive enough to detect cloud patterns within the boundary layer even without the presence of significant precipitation (there were copious clear air targets over the Tiwi's). The radar and visible satellite images indicated that early convection was sometimes organized in parallel rows or cloud streets (e.g. 26 Nov. in fig 3.2). During conditions of combined surface heating and strong winds, weak horizontal helical circulations can form in the boundary layer (LeMone, 1973). Theoretical and observational studies of these horizontal convective rolls (HCR's) have shown that they are aligned nearly

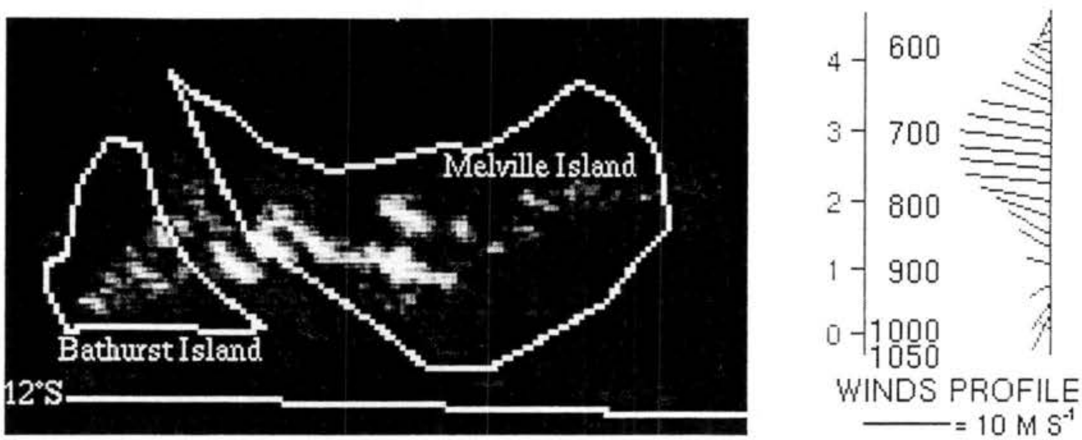

Fig. 3.2 Visible satellite image of Tiwi Islands at 0530 UTC on 26 Nov. 1995. Cloud streets parallel to the surface to 700-mb shear vector were evident. To the right is a vertical wind vector profile from the 0422 UTC Maxwell Point rawinsonde. Height [km] and pressure [mb] are indicated.

parallel to the mean boundary layer wind direction and can develop when an inflection point occurs in the mean wind profile (Kuettner, 1971; Mason and Sykes, 1982; Rabin et al., 1982). This inflection point can exist in tropical locations due to the jet-like vertical profile of the trade winds (e.g. Fig. 3.2). It is not very often that this type of organization was identifiable in the clear-air returns of C-pol reflectivity and velocity fields, possibly because of the low signal-to-noise ratio or the fact that low-level winds and the accompanying shear was generally weak over the islands. Inhomogeneities of low-level convergence and surface fluxes due to the complex coastline shapes and varying ground cover conditions might have had a greater influence on boundary layer convective organization. However, several investigators have observed coupling between HCR's and the sea breeze that enhanced convergence along the sea breeze front at points of intersection with each HCR (e.g. Mitsumoto et al., 1983; Wakimoto and Atkins, 1994; Atkins et al., 1995). This interaction probably occurred to some degree over the Tiwi Islands during the MCTEX when the low-level wind profile was appropriate for the formation of HCR's even when their structure was not clear on radar.

The sea breeze flow is influenced by the horizontal temperature difference between the land and the sea, and its structure is modified by small-scale motions induced by the variation of the land surface temperature itself (Mitsumoto et al., 1983; Xu et al., 1996; Chiba, 1997). Laird et al. (1995) examined Cape Canaveral, FL sea breezes and found that inland water bodies created their own lake/river breeze circulations, which interacted with and enhanced the convection associated with the sea breeze front. When the sea breeze approached and disrupted the quasi-stationary convergence zone associated with the river breeze, thunderstorms were triggered (Laird et al., 1995). During the MCTEX, it was shallow, isolated precipitating cells embedded in the gradient flow which were responsible for a similar inland convergence zone. These cells created evaporatively-cooled downdrafts that spread out at the surface. These divergent surface flows enhanced the low-level convergence ahead of each small cool pool. As they approached the leeward coast sea breeze front, rapid convective development ensued and strong thunderstorms were triggered just ahead of and along the sea breeze front. This progression of events will be reiterated below for the two case study days.

Similar to the Keenan et al. (1990) findings, the thunderstorms during the MCTEX usually commenced between 0300 and 0600 UTC, although some days experienced much earlier initiation due to external influences (e.g. 23 Nov. 1995).

3.1.4 Mergers

A detailed description of cloud mergers over the Tiwi Islands is provided by Simpson et al. (1993). They manually analyzed C-band radar data and categorized precipitating cells as either single cells, or first, or second-order merged complexes. Simpson et al. (1993) concluded that convection in the Maritime Continent was concentrated similarly to that found in Florida by Simpson et al. (1980). Simpson et al. (1993) also illustrated the multiplicative effects of merging on rainfall and echo area. They found that 70% of the rain was produced by second-order mergers, which represented less than 5% of the total number of convective systems.

Radar coverage did not facilitate a similar construction of merger statistics for the MCTEX. Complete island coverage was often sacrificed in lieu of sector scans, so the widely-scattered single-cell population was probably undersampled. Also, the radar was usually operated in *non*-polarimetric mode during the early afternoon. For those times, rain rate estimates would need to be based on Z_h alone, so they would first require a completely different attenuation correction technique (such as Hildebrand, 1978). Therefore, non-polarimetric radar volumes were not used for rain rate estimation. Fortunately, the higher-order merged cells were routinely captured by polarimetric radar. This allowed inferences to be made about the effects of cloud merging on precipitation production and storm electrification.

During the MCTEX, the most intense part of the island thunderstorm was usually preceded by a higher-order merger. As the gust front from a first-order merged cell spread radially along the surface, the strongest new convection was triggered along its intersection with the sea breeze front. The first-order merged cell usually originated along the sea breeze front, so the thrust of the new convection typically occurred where its gust front was perpendicular to the sea breeze front. The combination of mechanical lifting and enhanced moisture convergence along the sea breeze front provided the low-level support for deep tropospheric overturning. The storms usually appeared most intense between 0400 UTC and 0500 UTC (1330 and 1430 LST).

Without the dynamical support of upper-level wind shear, the heaviest precipitation eventually fell through the main updraft and stifled further growth. The rain-cooled air descended to the surface and spread out over a large portion of the islands. As new convection was triggered by the expanding gust front along its downshear edge (usually the western edge), the orientation of the thunderstorm complex shifted from a general east-west alignment to north-south. This usually occurred between 0430 and 0600 UTC.

3.2 23 November 1995 case study

3.2.1 Synoptic pattern

On 23 Nov. 1995, just to the west of the Tiwi Islands, an anticyclone at the surface was responsible for light southerly low-level winds. This flow converged with southeasterly winds east of Darwin, turned to the north, and merged with westerly equatorial flow west of New Guinea. At the 700-mb level (often considered the steering level for storms), the wind was south-southeast at about 10 m s^{-1}. A broad mid-level anticyclone just to the west of New Guinea was situated to the north of a 500-mb band of 5-10 m s^{-1} westerlies centered about 2° south of the islands. A major upper-level trough over western Australia was pushing east, forging brisk northwesterly flow over the Tiwi islands above 400 mb. These winds were associated with the strong subtropical jet ahead of the trough which had an entrance region about 8° south of the islands (Keenan et al., 1996a).

The thermodynamic profile shown in Fig. 3.3 was provided by a rawinsonde launched at 0106 UTC (1036 local standard time LST) from Maxwell Creek on Melville Island. This sounding indicated light westerly winds in the lowest 1 km with moderate southeasterly flow near 3 km AGL. Subsiding air in the mid-levels created a warm, dry layer between 4 and 6 km which inhibited deep convection early in the day. Above this temperature inversion, the winds were northwesterly, with speeds to 15-20 m s^{-1} in association with the entrance region of the jet stream over northern Australia. Except for the upper levels, the thermodynamic vertical profile was fairly typical for the tropics. Winds were light near the surface, with an easterly component near 700 mb. Evidence of a trade wind inversion existed just above the easterly trade wind.

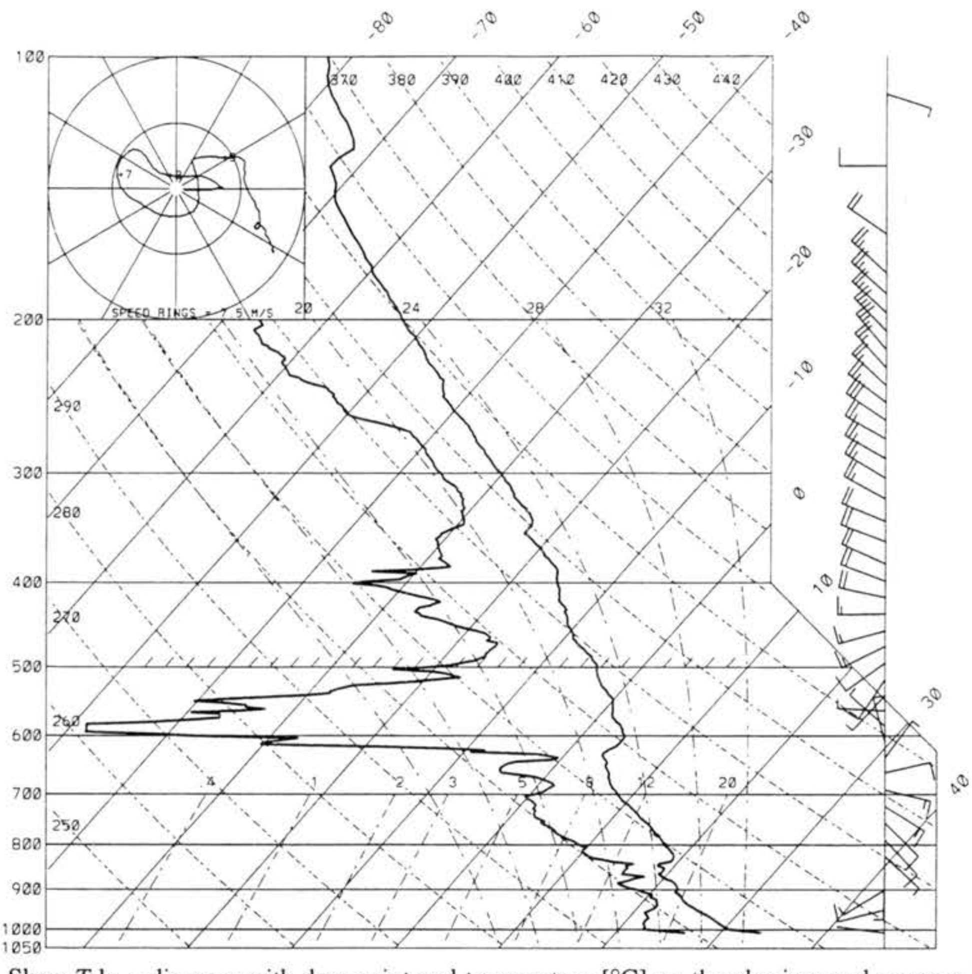

Fig. 3.3 Skew T-ln p diagram with dew point and temperature [°C] on the abscissa and pressure [mb] on the ordinate. Rawinsonde launched from Maxwell Creek, Melville Island, at 0106 UTC on 23 Nov. 1995. Horizontal wind barbs [knots] displayed on right side of figure. Full and half flags represent 10 kt and 5 kt, respectively.

By early afternoon, the atmosphere over the island interior had destabilized. Another island rawinsonde launched at 0304 UTC (skew-T not shown) indicated convective available potential energy CAPE

(500-m mixed layer) of 1508 $m^2 s^{-2}$ and a lifted index of -2°C. The combination of moderate instability and minimal low-level shear led to a high bulk Richardson number $\bar{R}$ (0.5-3 km mean density weighted shear) of 494.

R is the ratio of atmospheric instability to the low-level shear:

$$R = \frac{B}{1/2\ U^2}, \tag{3.1}$$

where B is the buoyant energy in the storm's environment (i.e. CAPE) and U is the difference between the density-weighted mean wind at 6 km and in the surface layer (taken as the 500-m mean wind). Keenan et al. (1990) chose 3 km for the upper boundary in their calculations of U because the 0.5-3 km layer better captured the low-level shear inherent between the trade wind and the near surface. This layer is very important in determining the structure and dynamical characteristics of storms. Weisman and Klemp (1982; 1984) found that unsteady, multicellular growth occurred most readily when R>30 and that supercellular growth was limited to environments for 10≤R≤40. According to their numerical modeling results and observations (Weisman and Klemp, 1982; 1984), an R of 494 favors unsteady, multicellular convective systems. The wind shear is not great enough to support long-lived convection since the main storm cell would tend to remain stationary while its gust front continued to spread at the surface. The cell would quickly find itself in the cold, stable environment behind the gust front, and further updraft development would cease. (Weisman and Klemp, 1986). High thermodynamic instability can compensate for lack of vertical wind shear and still promote short-lived strong convection with active downdrafts, cold pool generation, and unsteady redevelopment along gust fronts, as was the case for our case study days. Keenan et al.

(1990) found that the average November-December CAPE at Darwin, Australia (50 km to the south) from 1978-86 was 1420 $m^2 s^{-2}$ and R (0.5-3 km) was 759. The 23 Nov. indices were near these average values.

3.2.2 Early development over northeast Melville Is.

Cells over northeast Melville Island quickly overcame their convective inhibition and merged into an early afternoon thunderstorm complex. The early development of cells over extreme northeast Melville Island may have been modulated by large scale forcing beneath the left entrance region of the subtropical jet. Perhaps quasi-geostrophic lifting eroded the mid-level cap so that certain cells achieved their level of free convection much earlier than usual. After all, early convection was not limited to the island; it also occurred over the spine of Cape Van Diemen, a mainland peninsula 40 km to the east of Melville Is. Keenan and Brody (1988) found that 200-mb troughs and associated subtropical jet streaks could interact with and enhance convection in the Australian monsoon, leading to stronger convective banding to the east of the upper-level tropospheric feature. To what extent these findings apply to the pre-monsoonal period observed during the MCTEX is not certain. Clearly, these cells were in a most favored position over the Tiwi Islands due to the various small land protrusions and the off-shore flow of the gradient wind. Carbone et al. (1997) and Laird et al. (1995) also noted the importance of complex coastlines and narrow peninsulas (<20 km) in initiating early precipitating convection.

By 0200 UTC, two precipitating cells had formed over these favored spots along the far eastern coast of Melville Is. (cells 1 and 2 in Fig. 3.4a). Their radar-indicated cloud tops were 7-10 km AGL and they exhibited 40-50 dBZ maximum reflectivity. After ~30 minutes they deferred to new cells on their peripheries. One cell developed between the two original cells (cell 3), probably forced by the collision of downdraft outflows (Simpson, 1980). Another was triggered about 20 km to the southwest over another small peninsula (cell 4; Fig. 3.4a). By 0300 UTC (Fig. 3.4b), the cells grew to 12 km AGL, and they exhibited radial low-level convergence and cloud top divergence. Loops of radar reflectivity indicated unsteady cell development above the western edge of an emerging gust front. The entire system propagated inland with about 8-12 km spacing between successive precipitation cores (Fig 3.4c-e). Rapid intensification followed, as the storm reached 16 km AGL (with 40 dBZ at 6 km AGL) and produced cloud-to-ground (CG) lightning from 0316 to 0347 UTC. But after 0340 UTC, the leading edge of the gust front failed to force much new deep convection, and the storm soon collapsed, leaving behind a rain-cooled pool of air over northeast Melville Is. (Fig. 3.4f). As mentioned earlier, the sub-cloud boundary layer must be sufficiently mixed and moistened before deep convection can be sustained. Perhaps the lack of an adequate mixed layer in the early afternoon was responsible for the storm's demise. The gust front continued on its course, but was not very convectively active until it reached north central Melville Is. an hour later.

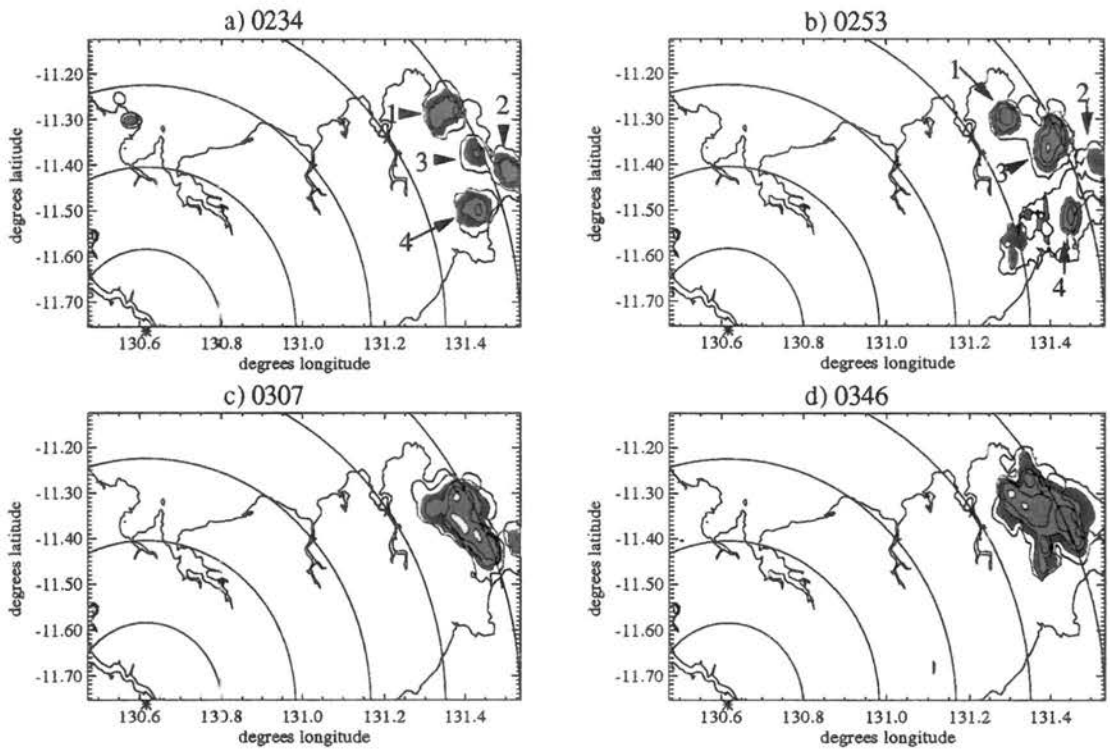

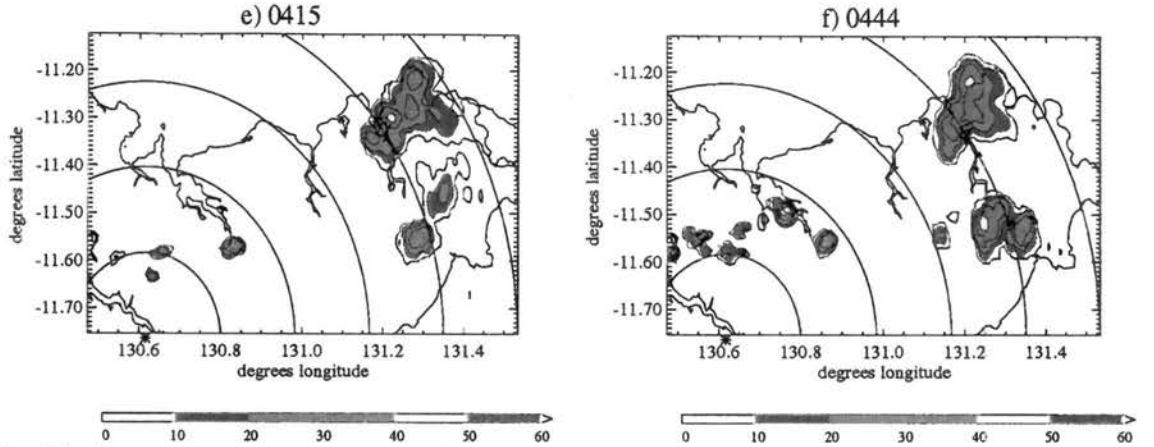

Fig. 3.4 Horizontal cross sections of Z_h [dBZ] over northeast Melville Island on 23 Nov. 1995. Asterisk denotes radar location, and radar range is contoured every 20 km.

3.2.3 Aircraft transects through boundary layer

A twin-engine Cessna C340 aircraft was deployed to monitor the boundary layer and sample temperature, humidity and winds during the MCTEX. Around 0330 UTC, with most of the island still free of deep convection, the aircraft traversed central Melville Island from north to south at an altitude of about 340 m (see Fig. 3.5). The south coast sea breeze front could be responsible for the convergent winds recorded at 0345 UTC, but the transition zone is not as sharply defined as the north coast sea breeze front. Seen clearly in the plan view of flight-level winds is the wind shift associated with the north coast sea breeze front (0338 UTC). Moist oceanic air with a northerly wind component and temperature (mixing ratio) of 28°C (18 g kg^{-1}) was converging with warmer (30°C) and drier (14 g kg^{-1}) island boundary layer air flowing from the west-southwest. The abrupt thermodynamic transition is evident in the time series of temperature and mixing ratio (Fig. 3.5). The horizontal distribution of temperature and moisture is also consistent with the warming and deepening of the mixed layer as it resided over the heated island. As maritime air was advected over the southern coast by the background flow, it encountered the warmer land surface. (Note the area of large moisture fluctuations from 0348 to 0351 UTC associated with turbulent mixing in the island boundary layer.) The mixed layer gradually warmed and moistened due to surface moisture flux and the steady influx of sea breeze air.

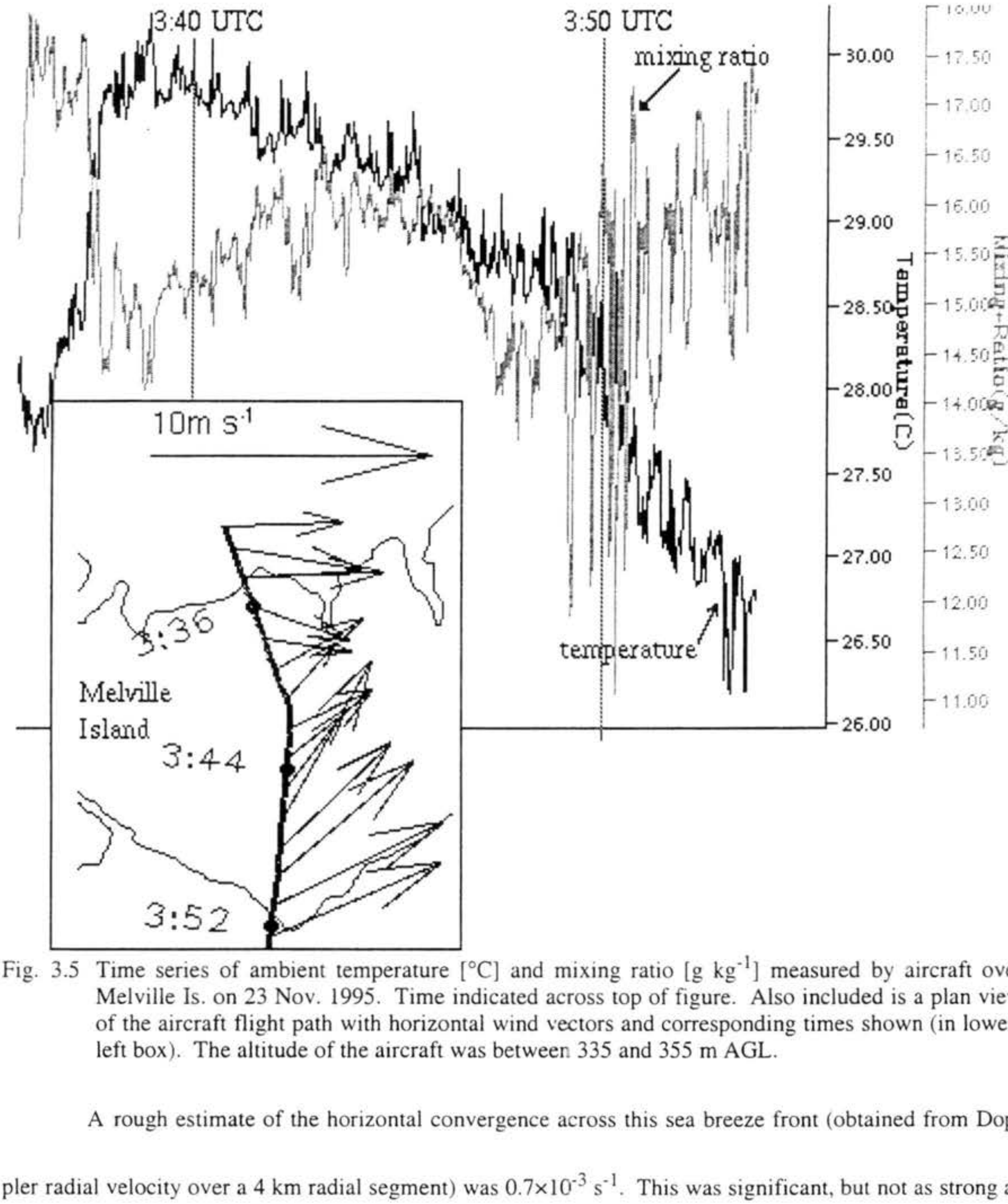

Fig. 3.5 Time series of ambient temperature [°C] and mixing ratio [g kg^{-1}] measured by aircraft over Melville Is. on 23 Nov. 1995. Time indicated across top of figure. Also included is a plan view of the aircraft flight path with horizontal wind vectors and corresponding times shown (in lower-left box). The altitude of the aircraft was between 335 and 355 m AGL.

A rough estimate of the horizontal convergence across this sea breeze front (obtained from Doppler radial velocity over a 4 km radial segment) was 0.7×10^{-3} s^{-1}. This was significant, but not as strong as the convergence estimated to exist along the edge of the expanding cold pool over northeast Melville Is. At 0326 UTC, radial velocities across this boundary spanned ±7 m s^{-1} over 5 km, resulting in 2.8×10^{-3} s^{-1}

radial convergence. Two hours later, the radial convergence near the north coast sea breeze reached a similar magnitude, partly due to the sea breeze and partly to the rapidly developing storms overhead.

3.2.4 Isolated cells over western half of islands

Unlike northeastern Melville, weather over the western half of the islands was relatively benign early in the afternoon. By 0317 UTC, a stationary cell formed over a small peninsula on the northwest coast of Melville Is., but quickly dissipated. Its evaporatively-cooled downdraft air probably reinforced the maritime air behind the northern coast sea breeze front. A time height section of this cell's radar reflectivity is shown in Fig. 3.6. This evolution was fairly representative of the short-lived precipitating cells scattered across the islands early in the day. The cells were fairly small but exhibited multicellular characteristics for some time. Usually the height of the 30 dBZ reflectivity surface never exceeded the -10°C level for more than a few minutes and they were rarely electrified to the point of producing lightning discharges. These single cells preceded significant merging and upscale development later in the day.

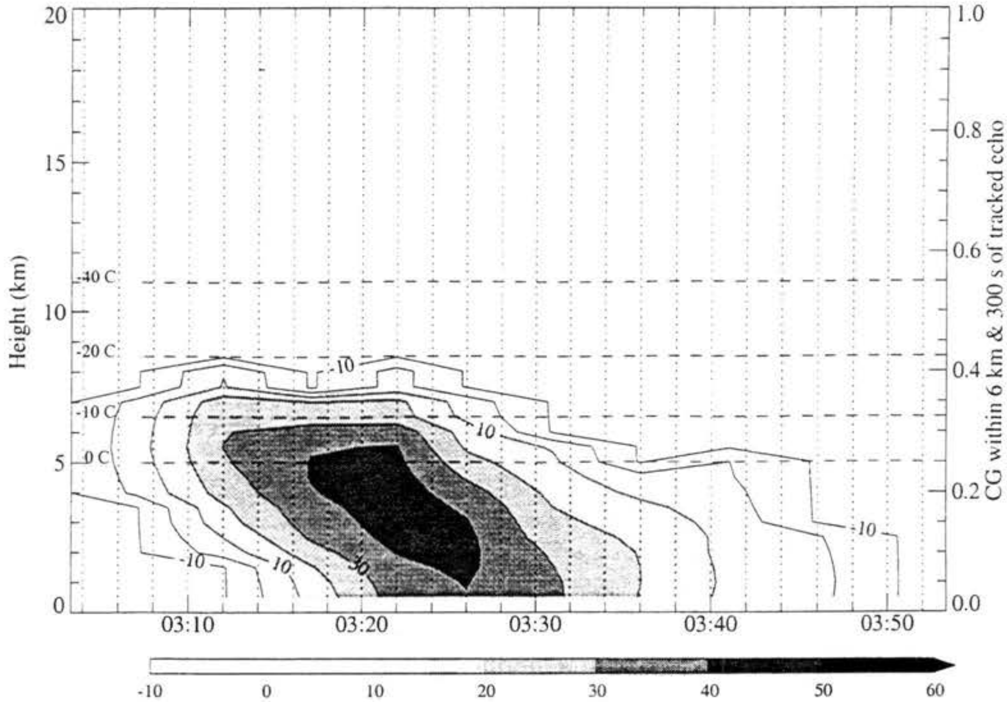

Fig. 3.6 Time height section of Z_h [dBZ] for a early afternoon cell that developed over a narrow peninsula of northwest Melville Is. (denoted P1 in Fig. 3.7) on 23 Nov. 1995. Environmental temperature is contoured with horizontal dashed lines.

Other precipitating cells developed just to the west of the radar in a region of enhanced low-level convergence between the west and south coast sea breezes. They propagated to the northeast with the synoptic flow at ~2 m s^{-1}. These cells only precipitated for ~30 minutes, but these shallow precipitating cells over Bathurst Is. appeared to generate cold pools of air which spread out radially along the surface. The edges of the cool pools were marked by a barely discernible enhancement in the reflectivity field that propagated outward from the precipitation echoes. The radar probably detected this feature due to elevated concentrations of airborne particulates and insects, and a sharper gradient of the radio refractive index along the boundary (Wilson and Schreiber, 1986). Carbone et al. (1997) observed that these shallow cool pools within the heated interior island boundary layer were 0.5-1% negatively buoyant with respect to the undisturbed island boundary layer. The RANK automated weather station (AWS; see Fig. 3.1 for locations) detected a 1-2°C temperature drop for a couple minutes when the edge of the clear-air reflectivity line was overhead (0541 UTC). The surface winds shifted from west to southwest and briefly gusted to 5 m s^{-1}. The MAXW AWS was affected by the rain-cooled air (no rain was recorded at either site, however) from 0420-0430 UTC. At this station, the temperature dropped by 3°C and the wind profiler detected a surge in southwest winds at 4 km elevation when the cells were directly above the site (0430 UTC).

Ignoring friction and Coriolis forces and using the Boussinesq approximation, it can be shown that the speed of a steady-state density current (c) with height h and a density exceeding that of the environment by $\Delta\rho$ is

$$c = k^* \left(gh\frac{\Delta\rho}{\rho_0}\right)^{1/2}, \tag{3.2}$$

where ρ_0 is the density of the environment and k* is $2^{0.5}$ (Houze, 1993). However, this theory is complicated by friction, viscosity, and detrainment at the head of the density current. To account for these effects, k* is usually replaced by k, an empirical value calculated from observed c, h, $\Delta\rho$ and ρ_0. Observed values of k are usually close to 0.8 (Wakimoto, 1982). If the density difference across the edge of the cool pool was 0.5-1%, and k was similar to that found in other studies (0.8-0.9; Simpson and Britter, 1980; Wakimoto, 1982), and the cool pool depth was 500 m, then the propagation speed of the current would be about 4 to 6 m s^{-1}. However eqn. 3.2 assumes the ambient flow parallel to the direction of propagation (U) is zero. A non-zero U cannot simply be added to c because of surface drag. The surface drag would increase when U is positive and decrease when U is negative. Based on the laboratory work of Simpson and Britter (1980), Seitter (1986) suggested that *0.62U* be added to c, where U is the ambient wind speed parallel to the gust-front motion (assuming k remains the same). Making this adjustment brings our estimate of cool pool front propagation speed to 7-10 m s^{-1}. This is slightly faster than the 3-7 m s^{-1} actually observed.

Perhaps the actual density current was shallower than 500 m, or maybe a smaller k should have been used. It is also possible that the radar signatures were merely lines of cumulus embedded in the mean flow that had no real relation to the gust fronts. Regardless, the precipitating cells must have modified the sub-cloud environment with their evaporatively-cooled downdrafts and they appeared to trigger deep convection when they approached the north coast sea breeze front.

3.2.5 First-order merger

Between 0400 and 0500 UTC the north sea breeze front was distinguishable by a double bulge pattern in the clear-air fields of reflectivity and radial velocity with the apex of each bulge serving as a favored site for subsequent cell initiation (Fig. 3.7). Observers did note cloud street-like organization of the radar echoes over the center of the Tiwi islands with some evidence for horizontal convective rolls (HCR's) aligned northwest to southeast intersecting the northern sea breeze front (BMRC, Nov. 1998). The west-northwest east-southeast alignment of these echoes was almost parallel to the subcloud-layer wind shear vector, and could be a sign that longitudinal rolls within the boundary layer modified the sea breeze. An observational study by Atkins et al. (1995) described the 3-D kinematic structure of such sea breeze front interactions. Atkins et al. found that HCR's over land were tilted and lifted by the front, enhancing vertical motion and cloud development at certain points along the sea breeze.

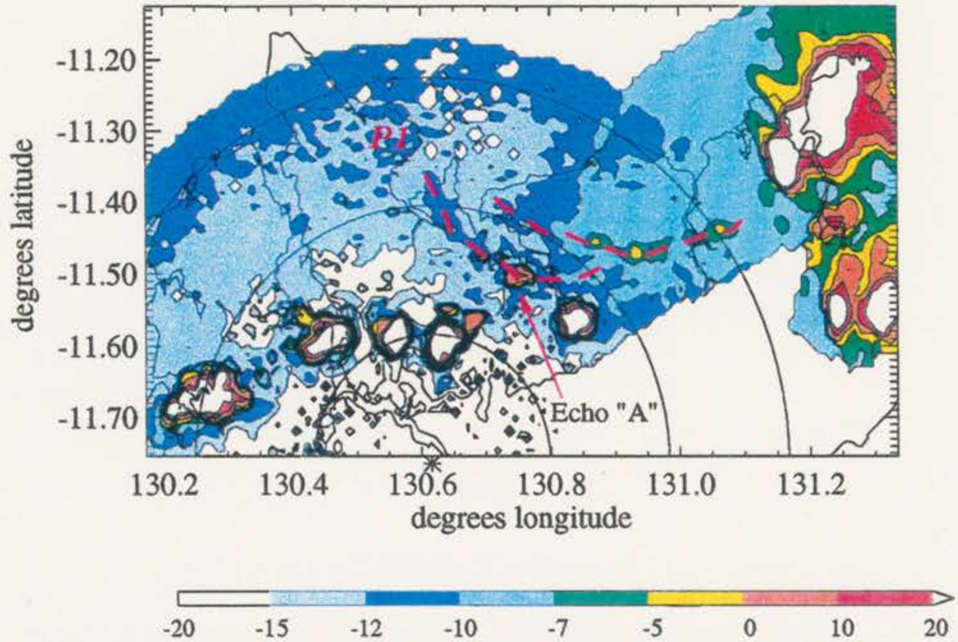

Fig. 3.7 Horizontal cross section of Z_h [dBZ] at 1.5 km AGL over northern Tiwi Islands at 0429 UTC on 23 Nov. 1995. The north coast sea breeze front is highlighted in red. The Z_h scale was shifted to lower reflectivities to accentuate the north coast sea breeze front echo. 20-km range rings centered on radar location (asterisk) and the coastlines of Bathurst and Melville Islands are delineated.

A time height section of horizontal reflectivity for the echo labelled "A" in Fig. 3.7 is provided in Fig. 3.8. As with the cell in Fig. 3.6, most of the precipitation initially developed below the freezing level, probably through warm-rain collision-coalescence processes. From 0405-0430 UTC, the updraft development stalled, as the bulk of the rain descended to the surface. By 0450 UTC, the cell was approached by shallow precipitating cells from the south and southwest. As the remnants of the precipitating cells approached the double bulge, a rejuvenated updraft was triggered between them, with enhanced outbound radar velocities suggesting brisk low-level inflow to cells along the sea breeze front and to cells a few kilometers to the south (0505 UTC). Over the next few minutes, the two updrafts merged as the southern cells, having unblocked access to island boundary air, grew and engulfed the sea breeze-cells (including echo A) to the north. The relative reflectivity minimum near 0520 UTC in Fig. 3.8 is due to a shift in focus to a cell at a slightly earlier developmental stage.

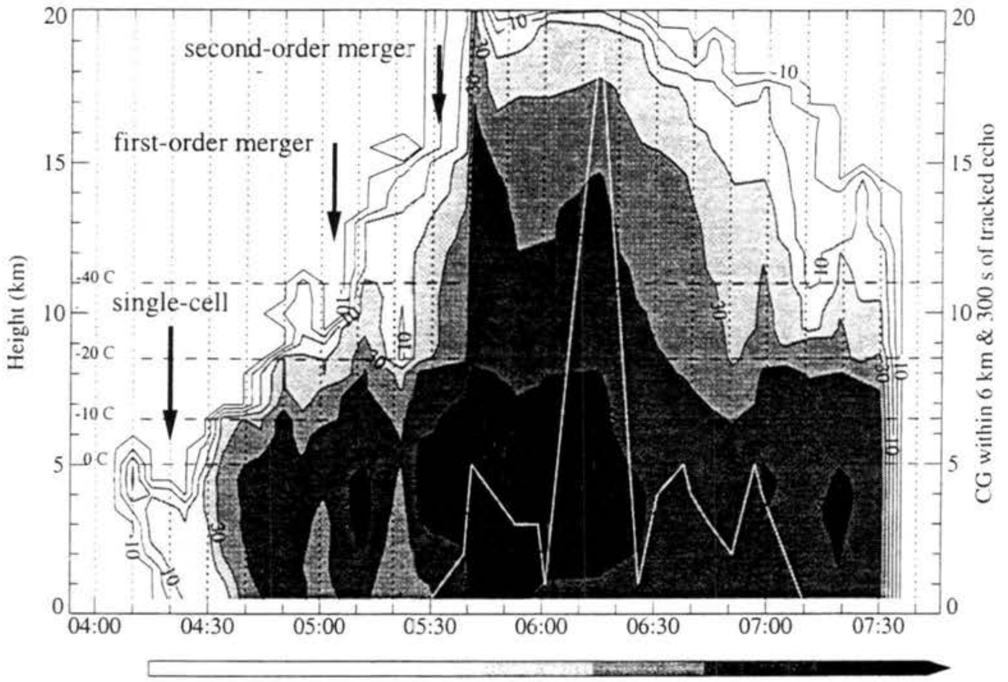

Fig. 3.8 Time height section of Z_h [dBZ] for echo "A" until 0515 UTC (23 Nov. 1995). Beyond 0515 UTC, second-order merged cells (echo "B") on the eastern flank of the downdraft from echo "A" are followed. Location of echo "A" is shown in Fig. 3.7 and "B" in Fig. 3.11. Environmental temperature is contoured with dashed horizontal lines. Thin white line is the total CG flashes detected within a prescribed time and distance from the tracked echo (discussed in Chapter 4).

The merger was coincident with a surge in radar cloud top height from 7 to 11 km altitude (0440-0455 UTC in Fig. 3.8). Several investigators have explored the reasons behind such growth (Lopez, 1978; Simpson, 1980). Above the mixed layer, moisture content drops off rapidly, and emerging updrafts find themselves in an unfavorable environment. If an updraft is too narrow, it quickly loses its buoyancy due to constant entrainment of relatively dry environmental air along its perimeter. Merging cells can protect each other from the environment, and therefore suffer less from entrainment compared to what they would as individual cells. The volumetric fraction of cloud exposed to the dry air shrinks, allowing more undiluted air parcels to fully realize their surface-based buoyancy in moist adiabatic ascent. Examination of maritime tropical soundings by Simpson et al. (1993) showed that the vertical distribution of CAPE did not allow more than weak-to-moderate updrafts in the lower parts of storms, but speeds as high as 40-60 m s^{-1}

could occur in the upper troposphere due to a deep, nearly dry-adiabatic layer between 400 mb and the tropopause (Webster and Houze, 1991; Golding, 1993; Simpson et al., 1993). If an air parcel broke through the trade inversion and withstood the drying effects of the environment near 600 mb (as shown in Fig. 3.3), it would accelerate rapidly, drawing upon the instability of the upper troposphere. In fact, analysis by Simpson et al. (1993) of 269 Darwin soundings (when island thunderstorms occurred) indicated that almost 60% of the CAPE resided above 400 mb.

Other studies strongly emphasized the importance of preexisting forcing on a horizontal scale of 30-300 km to the occurrence and organization of vigorous cumulus convection, both in the tropics and in Florida (e.g. Ogura et al., 1979; Simpson et al., 1980; Cooper et al., 1982). Such forcing existed along the north coast sea breeze front over the Tiwi Islands. A combination of downdraft outflow collisions and differential motion of cloud masses enhanced the low-level convergence and supported rapid storm growth after 0500 UTC.

3.2.6 Second-order merger

By 0512 UTC, additional rain developed over eastern Melville Island as precipitation filled in behind the gust front produced by the earlier northeastern Melville Is. storm. At the same time, heavy rain (Z_h>45 dBZ) approached the surface from the merged cells over north-central Melville Is.

Straddling the north coast sea breeze front, these merged cells produced a downdraft that forced new convective development on its east and west side. On the west side of the downdraft, the storm merged with additional convection occurring along the sea breeze front and generated an intense convective complex reaching 18 km AGL. To the east, the gust front from the merged cell over north central Melville Is. collided with the outflow from the earlier storm over far northeast Melville Island that was described in section 3.2.2. By 0539 UTC, the interaction of these two boundaries along the active sea breeze front triggered an intense storm with a radar cloud top to 20 km AGL! The time height evolution of reflectivity for this merged cell is shown in the latter times of Fig. 3.8.

When the aforementioned boundaries collided around 0540 UTC, the wedges of cool air generated a concentrated region of radial convergence near the surface. Radial velocity changed from 13 to -5 m s^{-1} over a 5-6 km radar ray segment, implying 3.6×10^{-3} s^{-1} radial convergence. As the storm matured, its downdraft surged to the southwest along the surface, while it ingested southwesterly low-level air just to the north of the gust front. The radially-aligned velocity couplet observed at 0540 UTC effectively rotated 90° relative to the radar beam so that a vigorous, 12 km wide, clockwise (cyclonic) rotation could be inferred at 0.5 km AGL by 0601 UTC (Fig. 3.9). This vertical (radial) vorticity persisted from the surface up to 5 km AGL. This rotation probably owed its intensity to vortex stretching above the interface of the opposing drafts. Its maximum strength, measured across 8 km, was 3.1×10^{-3} s^{-1}. Keenan et al. (1994a) performed a similar Doppler analysis of a 22 Nov. 1988 thunderstorm over Melville Is. during ITEX. They found a pair of counterrotating vortices with maximum intensity (2.4×10^{-3} s^{-1}) near 8 km elevation within a rapidly developing merged complex. Keenan et al. (1994a) ruled out the tilting of environmental horizontal vorticity into the vertical as a primary cause (Rotunno, 1981; Klemp and Rotunno, 1983; Simpson et al., 1986) since this explanation was inconsistent with the observed shear in the cloud layer. The radar-inferred mesocirculation observed by Keenan et al. (1994a) on 22 Nov. 1988 could merely have been convective-scale turbulence in the vicinity of a strong updraft (Keenan et al., 1994a). This does not appear to be the case for 23 Nov. 1995. Keenan et al. (1994b) noted that the structure of the planetary boundary layer is likely to be particularly complex where the interaction of storm induced outflows occurs. Investigators have shown that a growing updraft that moves over a pre-existing convergence line can concentrate the surface-based vorticity through vortex stretching (Wakimoto and Wilson, 1989; Brady and Szoke, 1989). Considering the spatial structure of the circulation, this is a plausible explanation for the mesovortex observed on 23 Nov. The width of the azimuthal shear couplet denoting the rotating air column was greatest near the surface and tapered with height, and the feature was also in the vicinity of what appeared to be a impressive updraft as evidenced by Fig 3.10b.

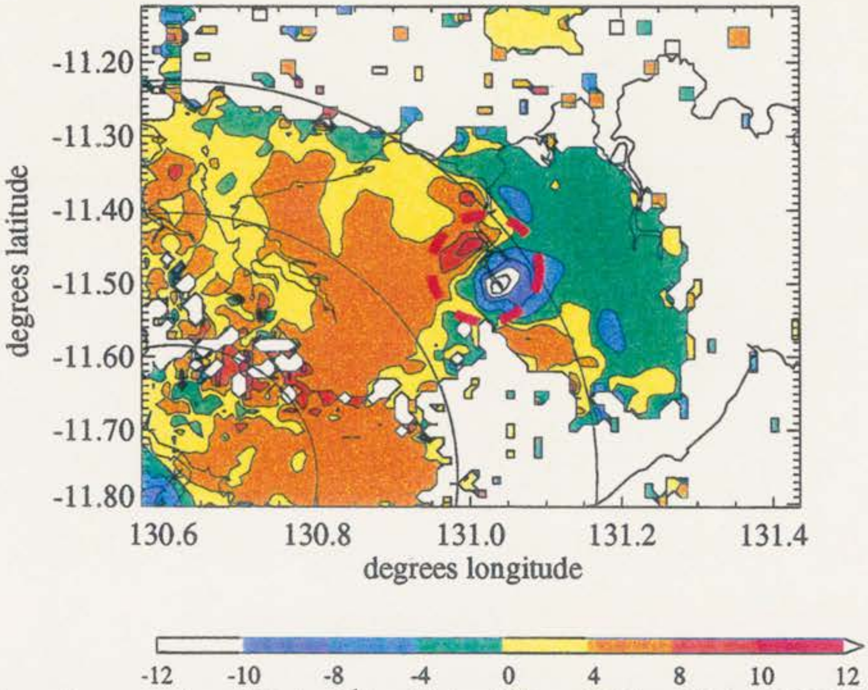

Fig. 3.9 Horizontal cross-section of V_r [m s^{-1}] at 0.5 km AGL on 23 Nov. 1995 at 0601 UTC. Region of intense radial vorticity is circled. This is the interface between two colliding gust fronts.

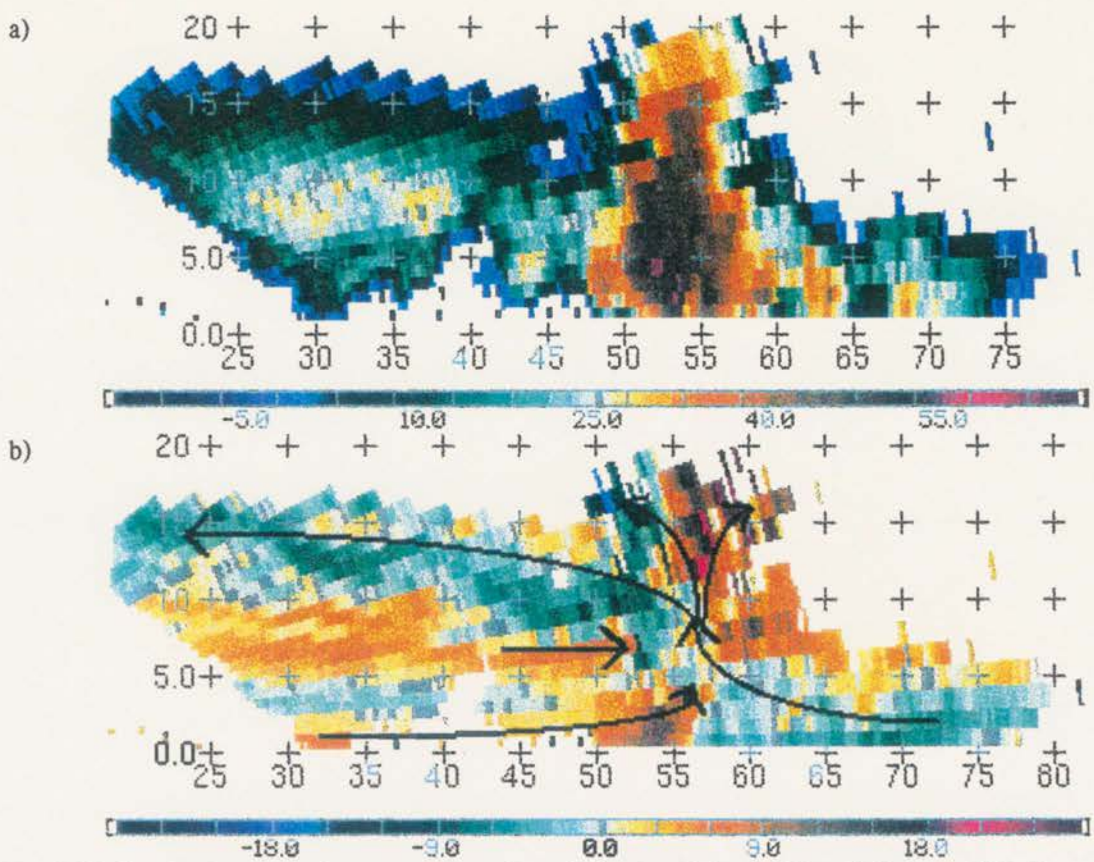

Fig. 3.10 C-pol radar vertical cross sections along 49° azimuth for 0541 UTC 23 Nov. 1995 (denoted by solid black line in Fig. 3.11). Elevation and range [km] are labelled. a) Z_h [dBZ] b) V_r [m s^{-1}] Cool colors denote movement towards the radar (to the left of the figure) and warm colors denote movement away from the radar (to the right).

Figure 3.11 shows a horizontal cross section of reflectivity at 2 km AGL depicting the two major convective systems over northern Melville Island at 0541 UTC. The eastern storm was explored with vertical radar cross sections at constant azimuth (Figs. 3.10a-b). Strong radial convergence was evident from the surface to 7 km. This, in addition to the divergent radial flow in the upper levels indicated a strong updraft. Above 11 km, the radially divergent outflow above the updraft was estimated at 3.6×10^{-3} s^{-1} over a horizontal span of 15 km. Note the reflectivities greater than 40 dBZ above the freezing level (~5 km). Near-zero values of Z_{DR} in this region (not shown) were indicative of frozen hydrometeors, and the high Z_h suggested that a large quantity of graupel particles were probably present.

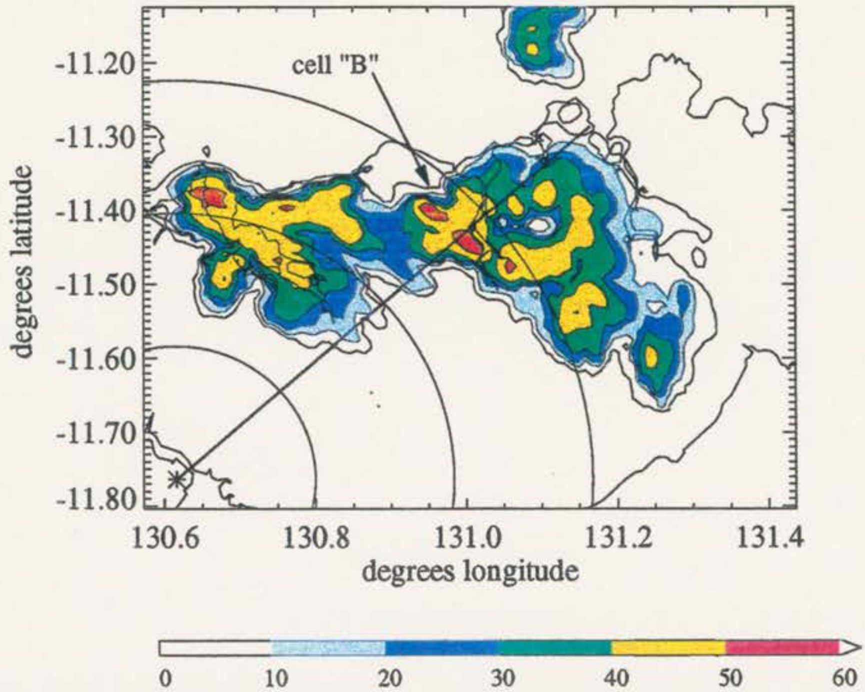

Fig. 3.11 C-pol horizontal reflectivity [dBZ] at 2 km AGL for 0541 UTC 23 Nov. 1995. The straight line extending from the radar site denotes the azimuth of the vertical cross sections shown in Fig. 3.10a-b. Asterisk denotes the radar location and the coastlines of Bathurst and Melville Islands are delineated.

3.2.7 Dissipative stage

After 0700 UTC, the main storms were separated from their buoyancy source by the ever-expanding downdraft. Deprived of their fuel, they rapidly weakened and collapsed. At this time, observers noted significant amounts of ice falling from the anvil, possibly being entrained into the updrafts (BMRC, Nov. 1998). Weak convection was promoted along the north and western edge of the spreading island-scale cold pool for two main reasons: this side of the cool pool continued to intercept unperturbed island boundary layer air, and it was also the side that benefited most from the environmental wind profile. The unperturbed boundary layer air was boosted to its level of free convection (1.5 km) by the wedge of cold air, but due to the strength of the cool pool and lack of upper-level wind support, the updrafts (Fig. 3.12) were severely tilted. The fact that convection was most prominent over the northwestern edge is consistent with the gust front theory offered by Rotunno et al. (1988; see Fig. 3.13). According to Rotunno et al.

(1988), the baroclinically-generated horizontal vorticity from the cold pool can cause buoyant updrafts along its edge to be tilted upshear and lean too far over the cold pool. For more vertically erect and stronger updrafts, the ambient wind shear must counteract the vorticity generated by the horizontal buoyancy gradient across the cold pool. This is conceptually illustrated in Fig. 3.13 and can help explain the prevalence of westward propagating squall lines in the presence of easterly trade winds over the Tiwi Islands. Along the eastern edge of the cool pool, the environmental shear did not counteract the horizontal vorticity generated by the density current, so the surface air parcels were probably swept behind the cold pool by a highly slanted updraft and entrained into its wake, never attaining their level of free convection.

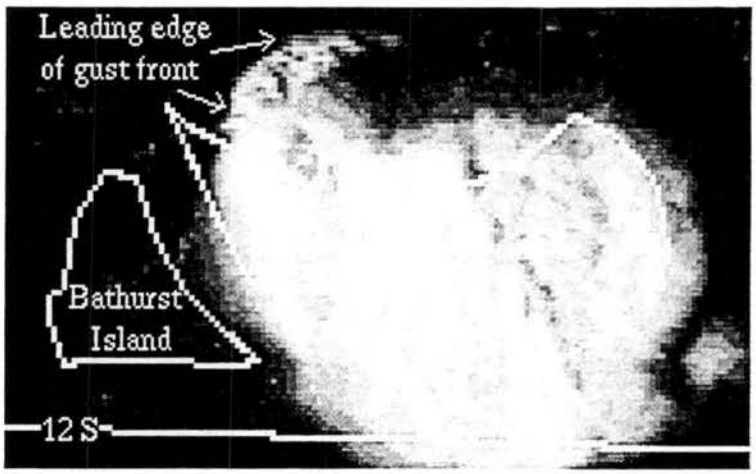

Fig. 3.12 Visible satellite image of Tiwi Islands at 0630 UTC 23 Nov. 1995 showing arc-shaped, convectively active leading edge of gust front over the ocean and northeast Melville Island. Brisk northwesterly upper-level flow sheared the anvil cloud top towards the southeast.

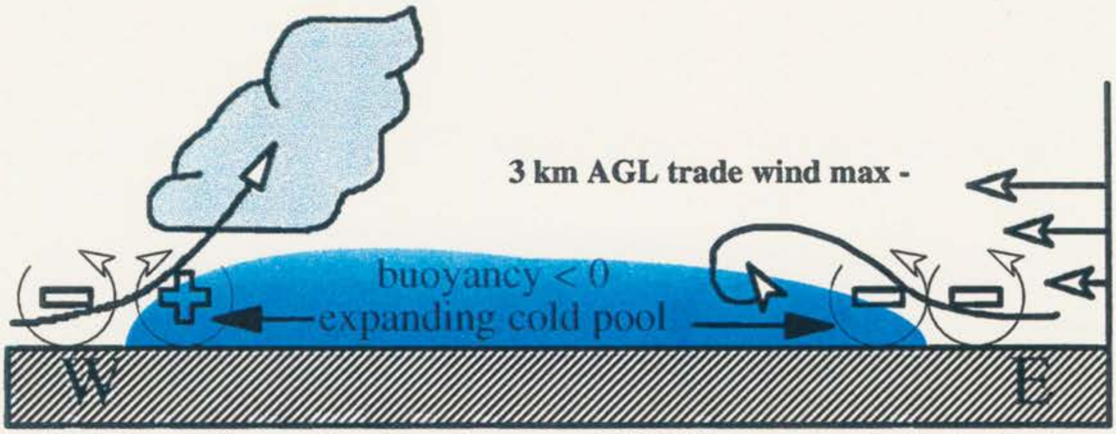

Fig. 3.13 Schematic diagram adapted from Rotunno et al. (1988) illustrating how the low-level trade wind shear (depicted in vertical profile on the right) may have promoted updraft development on the western edge of the strong cold pool.

3.3 27 November 1995 case study

3.3.1 Synoptic overview

We now shift our focus to the second case study day, providing a similar overview of environmental conditions and the lifecycle of convection. The Regional BMRC Analyses of Atmospheric Circulation during the MCTEX (Keenan et al., 1996a) showed that the dominant circulation feature on 27 Nov. was a strong upper-level anticyclone centered 2° north of the Tiwi islands. Strong 200-mb divergence was evident with this feature and its closed circulation extended down to 500 mb. At 700 mb, almost the entire northern coast of Australia was covered by a wide band of 5-10 m s^{-1} easterlies, and the surface flow varied from calm to light easterlies to the east of the Tiwi Islands (Keenan et al., 1996a).

The 2158 UTC Maxwell Creek rawinsonde (Fig. 3.14) detected northeasterly near-surface flow (5-10 kt) situated beneath stronger easterly flow at trade wind level (20 kt). Above that, the wind direction backed to the west and dropped to 5-15 kt between the 300 and 150-mb levels.

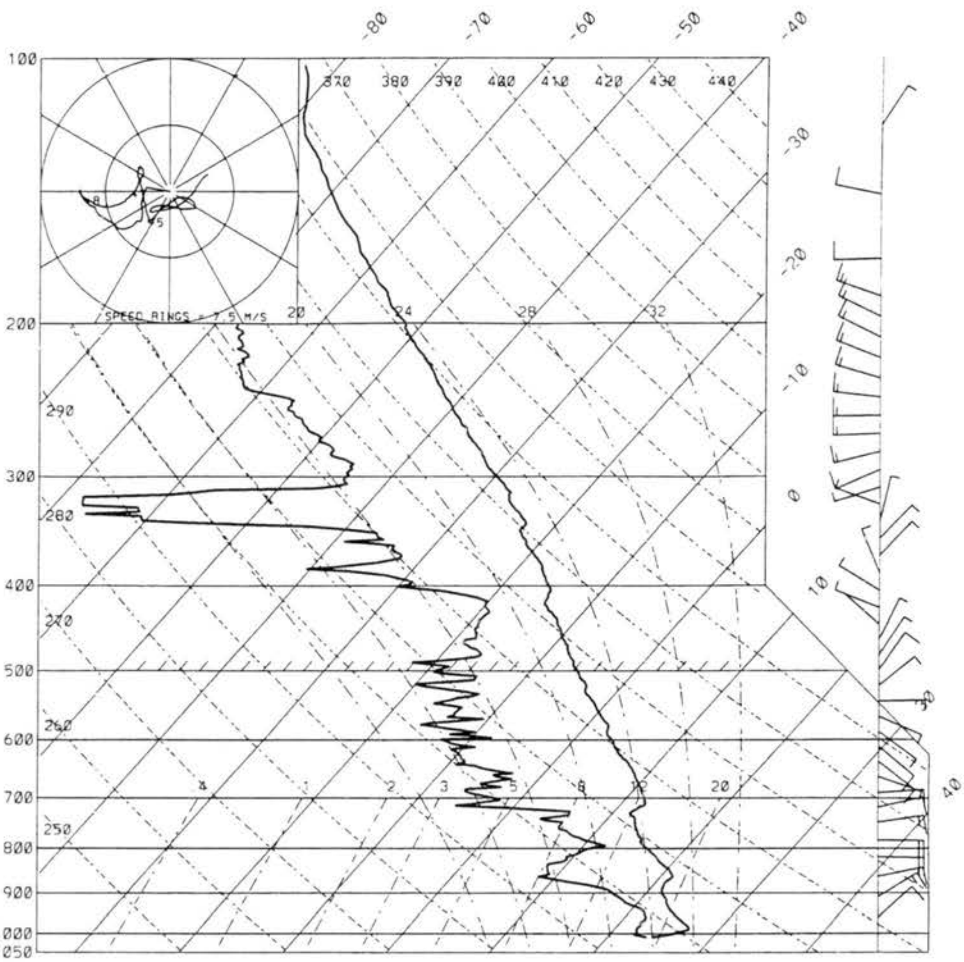

Fig. 3.14 As in Fig. 3.3 except for 2158 UTC on 26 Nov. 1995.

A nocturnal temperature inversion was still present at the surface, but abundant low-level moisture ensured some degree of instability. Lifted index and CAPE (500-m mixed layer) values were -3°C and 903 $m^2\ s^{-2}$, respectively. The bulk Richardson number (R; 0.5-3 km) was 108. Another sounding taken on 27 Nov. close to the time and location of the initial deep convection (0258 UTC) indicated a warmer and slightly drier surface mixed layer than at 2158 UTC, with very similar stability indices (e.g. LI was -2°C, CAPE 703 $m^2\ s^{-2}$, and R 112). This again suggested unsteady multicellular convection (Weisman and Klemp, 1982; 1984). As we will see later, this was indeed the preferred mode for the convection, and after cells merged along the southern coast sea breeze front, a squall line formed which rapidly propagated out to sea with the 850-700 mb steering flow. It is important to realize that pre-storm soundings are not wholly representative of the actual conditions experienced by the squall line, so one must be careful when applying the bulk Richardson number calculated from the environmental profile outside of the storm's immediate environment to the storm. By the time the squall line forms, the low-level flow may be significantly modified and complicated by outflows and pressure perturbations induced by the merged convective complex, making the pre-storm R less applicable. 27 Nov. had a lower R than 23 Nov. and this may have been manifested in the higher degree of storm organization (weak squall line) than observed on 23 Nov. (short-lived multicell). Apparently the vertical wind profile on 27 Nov. was sheared enough to push the updrafts downshear and lengthen the period over which the cells maintained their low-level convergence and fed on the high θ_e air ahead of the gust front. The gust front did not surge too far ahead of the updrafts.

Also apparent in the 2158 UTC sounding (Fig. 3.14) was the trade wind inversion near 3 km AGL, and another temperature inversion near 1.5 km AGL that may have been enhanced by the descending branch of the land breeze circulation. Surface winds, where they were strong enough to be detected by the AWS, were offshore and were consistent with such a circulation at the time of the sounding.

3.3.2 Storm evolution

Light northeasterly surface winds (<5 m s^{-1}) encouraged initial convective development over Bathurst Island. Crook (1997b) used a 3-D mesoscale numerical model to simulate the island convection for this particular MCTEX day and he successfully replicated the observed location and spatial structure of the initial storms over the southwest part of the islands. Additional simulations of this day were designed by Saito et al. (1997). Low-level air appeared to ride up and over the sea breeze front, reach its lifted condensation level, precipitate into the cool oceanic air behind the front, and trail off to sea. Holland and McBride (1989) similarly observed an evaporatively cooled downdraft from a cloud that had formed in rising continental air over a sea breeze front in northern Australia. It was entrained through the turbulent wake region behind the front and dropped deep into the sea breeze head (Holland and McBride, 1989). This process was favored over the southwest peninsula of Bathurst where the convex shape of the coastline and an accompanying inland bulge in the northwest Bathurst sea breeze maximized low-level convergence. Small cells embedded in the east-northeast flow developed sporadically across the northern part of the islands, and propagated towards the south coast sea breeze front.

A distinct reflectivity fine-line propagated out ahead of the precipitating cells. If the fine-line was associated with pools of cool air created by the evaporation of rain from the cells, then it should behave like a density current. Earlier, for 23 Nov., we estimated the speed for such a current, accounting for friction, viscosity, detrainment and ambient wind. In this case, with a 2 m s^{-1} background flow, and similar assumptions of depth, Froude number and density difference, the theoretical speed would be 5-6 m s^{-1}. The observed propagation speed was not too disparate (3-6 m s^{-1}), which lends credence to the hypothesis that the reflectivity signature is indeed the edge of an advancing shallow cool pool generated by the scattered precipitating cells approaching the southern coast.

The action quickly accelerated once these small showers and their accompanying thin reflectivity fine line converged with the well-defined southern sea breeze front. The updrafts penetrated through the freezing level, resulting in storm tops exceeding 12 km AGL by 0350 UTC.

By 0415 UTC, a wet microburst (Figs. 3.15 and 3.16) impacted the surface and enhanced convection on its western edge. Figures 3.15 and 3.16 show heavy precipitation juxtaposed with a high radial velocity differential (14 m s^{-1} per 3 km) 10 km north of the radar. The 0258 UTC sounding (not shown) indi-

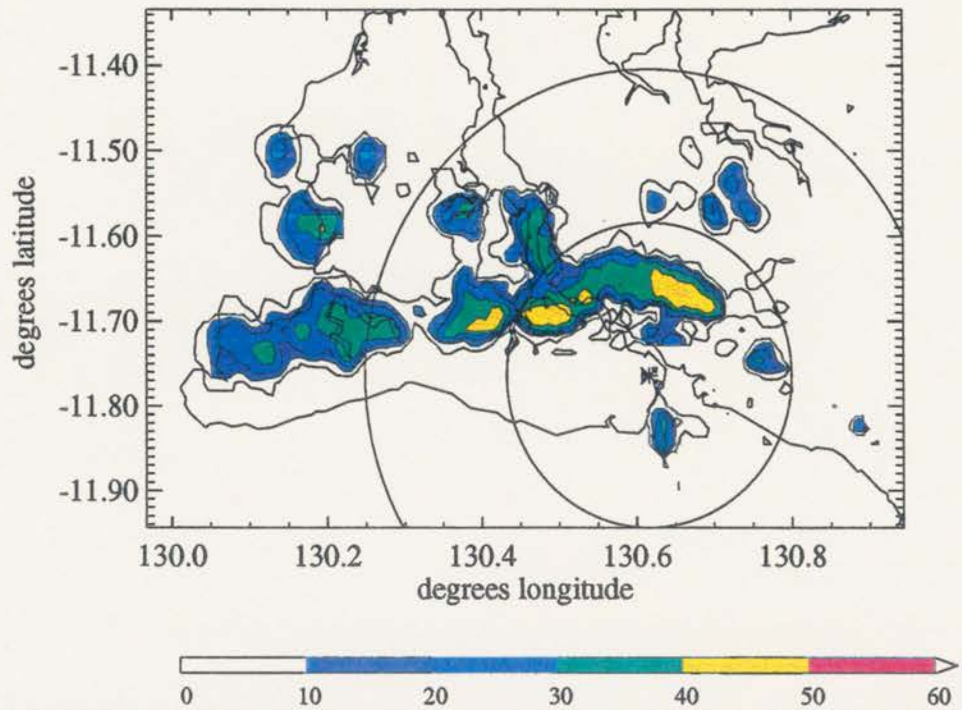

Fig. 3.15 Horizontal cross section of Z_h at 0 km AGL [dBZ] for 27 Nov. at 0420 UTC. Coastlines of Bathurst and Melville Islands shown, asterisk denotes radar location, and range ring spacing is 20 km.

cated a mixed layer from the surface to just above the 900-mb level. Nearly saturated conditions above this suggested a cloud layer to the 700-mb level. Assuming a continuous source of evaporating precipitation, the temperature of a downdraft originating from the cloud base should follow the wet-bulb temperature as it descends to the surface. By following a moist adiabat in the 0258 UTC sounding from cloud base to the surface, we estimated a temperature deficit of 6°C for air parcels within the microburst by the time they reached the ground. Compared with most microbursts studied to date, this event occurred in an environment with a relatively shallow and moist mixed-layer. Many studies of U. S. plains-type microbursts have shown the prevalence of a very dry, deep adibatic subcloud environment with dew-point depressions of

20°C (McCarthy and Wilson, 1984). Evaporative cooling within this dry layer is seen as crucial to maintaining the negative buoyancy of the microburst (Srivastava, 1985; Wakimoto, 1985). Keenan and Carbone (1992) observed a microburst event in the vicinity of Darwin, and noted that given the moist (precipitable water twice that of U. S. plains-type microburst producing storms), stable and shallow PBL observed in the tropical sounding, the role of water loading may assume relatively greater importance.

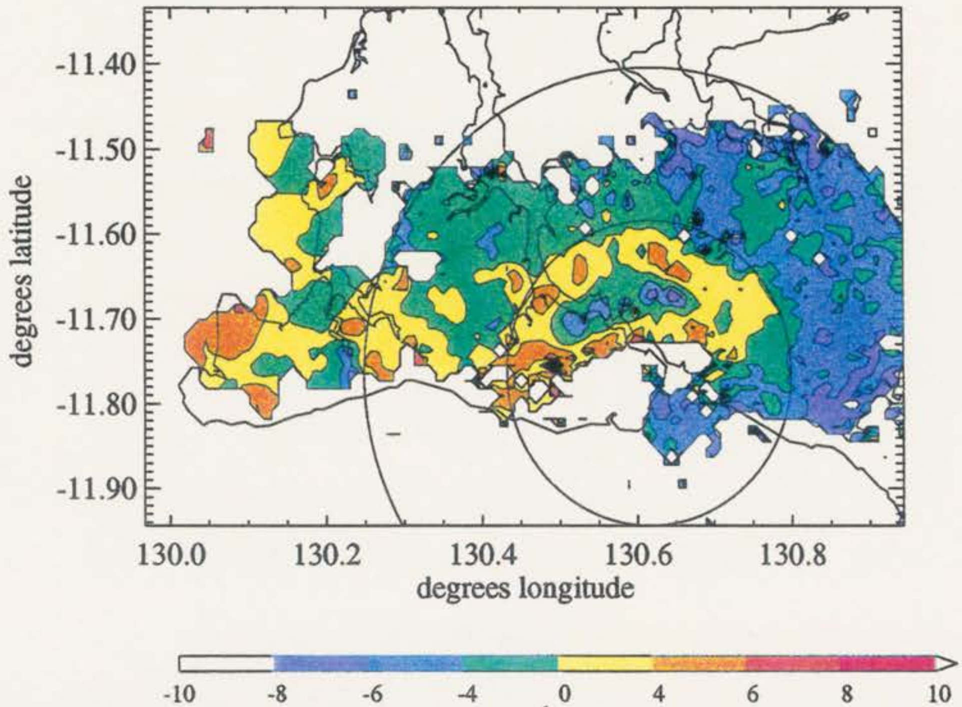

Fig. 3.16 As in Fig. 3.15 except for radial velocity [m s^{-1}]. Negative (positive) values denote air movement towards (away from) the radar.

The east-west aligned complex of cells eventually organized into a squall line that propagated to the west. Northeasterly surface winds kept the eastern edge of the cold pool quasi-stationary, but they continued to advect the convectively unstable boundary layer air from eastern Melville Is. over the edge of the cool pool. This fostered intermittent strong storms about 30 km north-northeast of the radar through 0800 UTC.

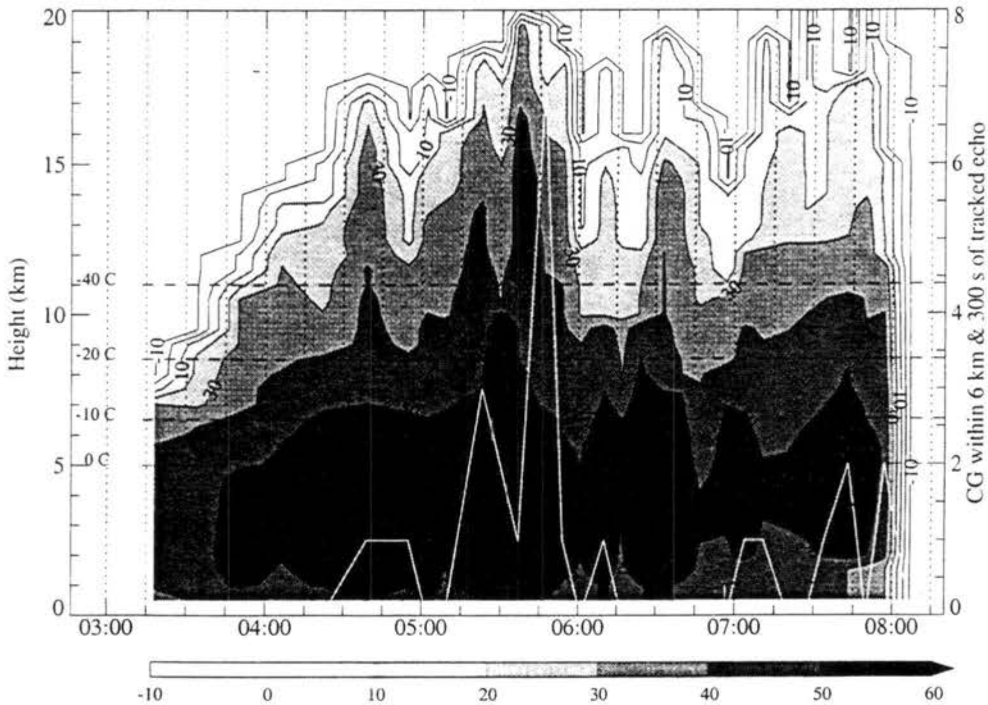

Fig. 3.17 Time height section of Z_h [dBZ] that follows cells in the most vertically developed sections of the thunderstorm complex that formed over southern Bathurst and Melville Islands on 27 Nov. 1995. Also shown (thin white line) are the number of CG flashes detected within a certain range and time of the cells.

A time height section of reflectivity from 0312-0800 UTC (Fig. 3.17) chronicles the vertical distribution of reflectivity in the stronger cells of the thunderstorm complex that bubbled westward along the sea breeze front over southern Bathurst Is. This was not a squall line in the classic sense with an uninterrupted north-south convective line. The convective elements were more disjointed, with separate cells forming above the westward moving gust front in discontinuous jumps. Usually the precipitation cores of successive cells were spaced by 8-14 km. Fig. 3.18 illustrates the scattered distribution of the convection. Fig. 3.19 explores one section of this developing thunderstorm complex with vertical cross-sections taken along the straight line in Fig. 3.18. These vertical cross sections of radial velocity and reflectivity were approximately parallel to the direction of storm propagation, and they exhibited some similarities to the Houze et al. (1989) conceptual model of a mesoscale convective system. Rear-to-front flow was evident in the radial velocity field from the surface to near the melting level (5 km AGL), extending from 10 to 40 km range (Fig. 3.19b). This circulation feature resembled the descending rear inflow jet often found within the trailing stratiform precipitation of mesoscale convective systems. Horizontal potential temperature gradients generated by a combination of latent heat release in the convective region and evaporative cooling in the stratiform region cause a horizontal pressure gradient and generate horizontal, line-parallel vorticity (Lafore and Moncrieff, 1989; Rasmussen and Rutledge, 1993). The rear inflow is a consequence of these processes. The relevance of this rear-to-front flow to the propagation and maintenance of north Australian squall lines was described by Keenan et al. (1992). Turning back to Fig. 3.19b, we see that the radial wind accelerated from 3 to 10 m s^{-1} before it encountered deep convective elements at a radar range of 35-40 km. It also appeared to reach the surface around 30-40 km range. The Rotunno and Klemp (1988) theory on the longevity of gust front convection is complicated by the presence of such a rear inflow jet. This stream of air has the same sign of horizontal vorticity as the advancing cold pool, so it can transfer mid-level easterly momentum to the surface and generate horizontal vorticity along the advancing gust front, adding to that already baroclinically produced by the cold pool (Lafore and Moncrieff, 1989; Keenan and Carbone, 1992). This boosts the forward momentum of the cold pool and adds to the rearward tilt of the updrafts. One can see in Fig. 3.19 that the height of the radar echo increases rearward, suggesting such a slanted updraft. At 35-40 range, the inbound low-level air near the front of the storm met the rear inflow jet and was swept to the upper levels where it spread laterally above 10 km AGL. The marginal deep-tropospheric wind shear precluded a forward overhanging anvil, a feature often observed in strong mid-latitude squall lines. Forward progress of individual elements was briefly more rapid, but the average motion of the entire system was about 10 m s^{-1} to the west. This reflected the environmental wind between 850 and 700 mb, similar to the findings of Keenan and Carbone (1992).

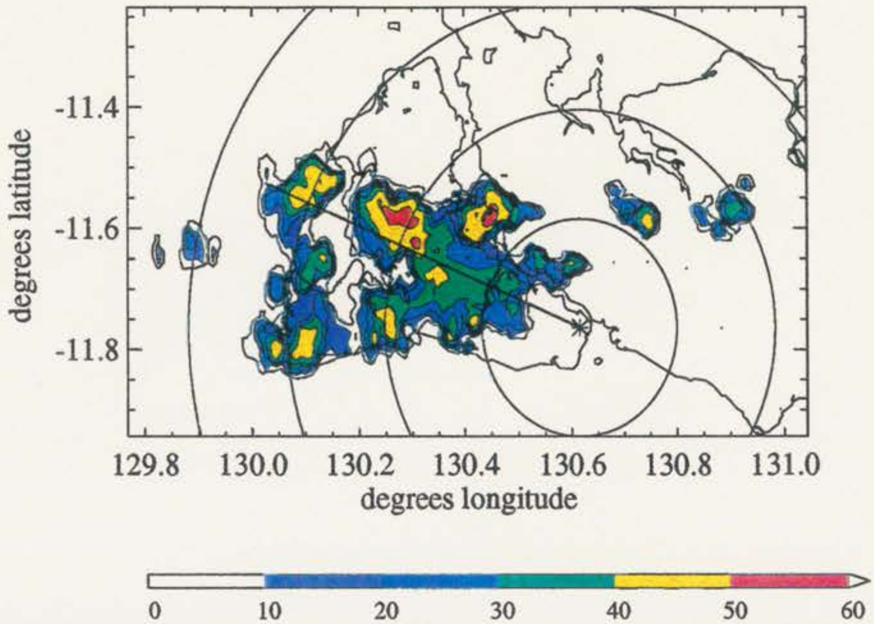

Fig. 3.18 Horizontal cross section of Z_h [dBZ] at 2 km AGL on 27 Nov. at 0509 UTC. Vertical cross sections in Figs. 3.19a-c are taken along solid black line at 292° azimuth. Coastlines of Bathurst and Melville Islands are delineated and an asterisk marks the radar location.

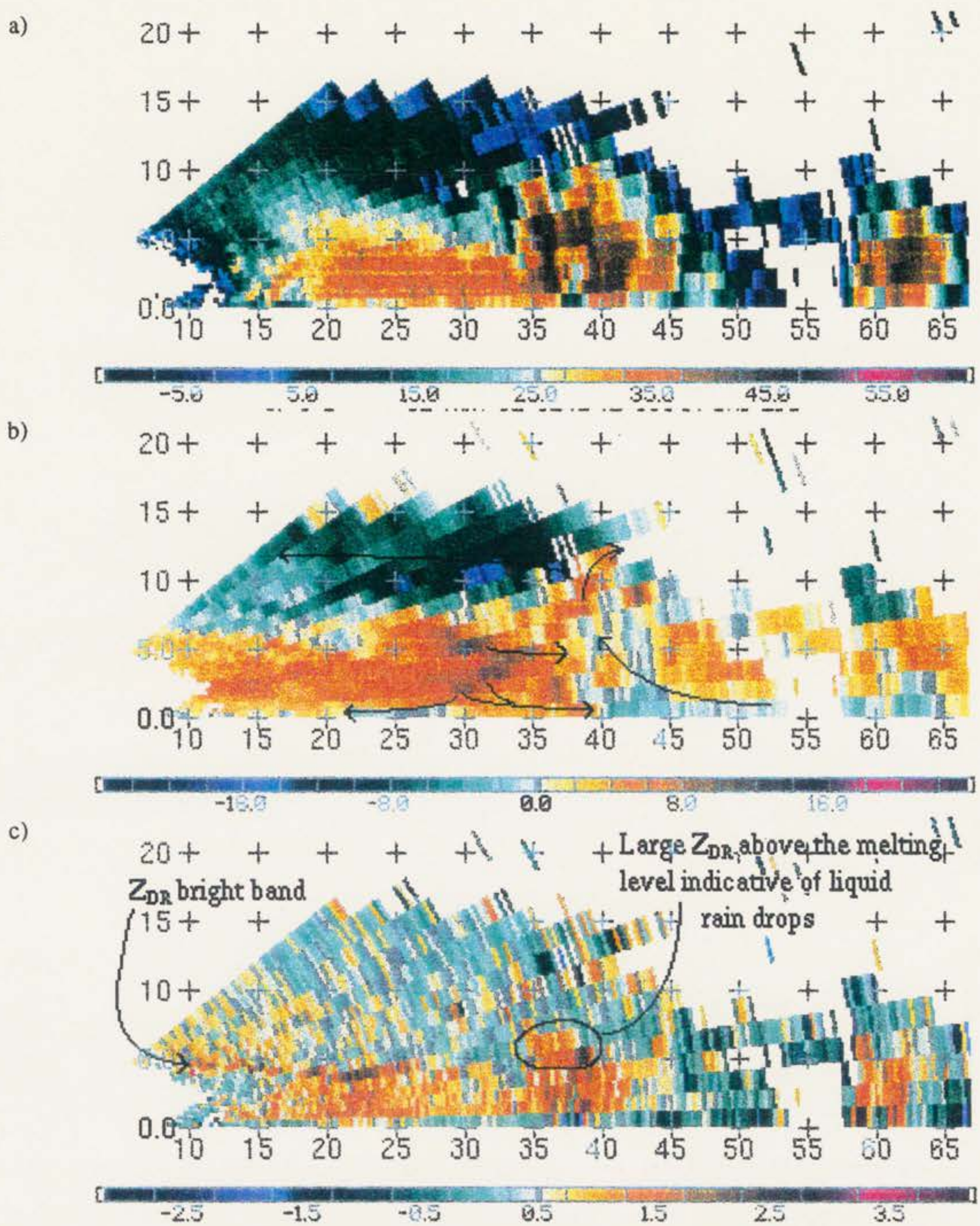

Fig. 3.19 C-pol radar vertical cross sections at 292° azimuth at same time as Fig. 3.18 (0509 UTC). a) Z_h [dBZ] b) V_r [m s^{-1}] Cool colors represent motion towards the radar (to the left of the figure). Warm colors signify motion away from the radar (to the right of the figure). c) Z_{DR} [dB] Sub-zero Z_{DR} values beyond 45 km range are probably due to differential attenuation.

CHAPTER 4

Precipitation and Electrical Trends

While Chapter 3 primarily dealt with radar and kinematic storm features on the scale of two or three convective elements spanning 5-20 km, this chapter takes a broader look at certain trends from an island-scale perspective. Radar estimates of rain mass flux and ice mass aloft were made in a bulk sense, often integrated over a large portion of the island domain. Rain mass flux estimates comprise the first part of the chapter. Then polarimetric data are used to infer microphysical characteristics of the precipitation. The temporal and spatial distribution of lightning (CG and total flashes) is then compared to the radar fields, and with merger processes in mind, inferences are drawn with regard to storm electrification theory.

4.1 Total storm rain mass flux

We already illustrated the deleterious effects of attenuation on horizontal reflectivity at C-band with our comparison of rain mass flux estimates before and after attenuation correction (section 2.3.4). Another potential problem that was likewise alleviated by dual-polarization measurands was beam blocking (Zrnic and Ryzhkov, 1996). Fig. 4.1 shows rain mass flux for the entire island domain as estimated by Z_h for two low levels: 0.5 and 1 km AGL. The 0.5-km level was most likely affected by beam blocking and therefore, was biased towards low rain rate estimates. Obstacles which partially blocked the radar beam at low elevation angles lowered precipitation estimates based exclusively on echo signal strength (i.e. Z_h) while having only a minor effect on estimates using Z_{DR}, Z_{DP} or K_{DP}. This is because the horizontally polarized beam loses approximately the same power as the vertically polarized beam when it intercepts ground targets. This phenomenon was borne out by precipitation estimates made at 0.5 and 1 km AGL with $R(K_{DP})$ as the primary algorithm (Fig. 4.2). Compared to Fig. 4.1, there was almost no difference between the rain flux estimates at the two vertical levels. If the rain rates actually did decrease significantly between 1 and 0.5 km elevation (possibly due to evaporation) then the same trend would be expected for estimates based on K_{DP}. Beam blocking became an issue at greater ranges since the near-surface estimates of rain rate required data from the lowest radar beam elevation angles. For example, within 40 km of the radar, the 0.5-km AGL rain rate was consistently higher for $R(Z_h)$ estimates than for $R(K_{DP})$ estimates (reasons for this are not clear). But beyond 40 km, the opposite was true, with $R(Z_h)$ accumulated rainfall consistently falling short of $R(K_{DP})$ values. Again, this was probably the influence of beam blocking in the lowest radar elevation angle.

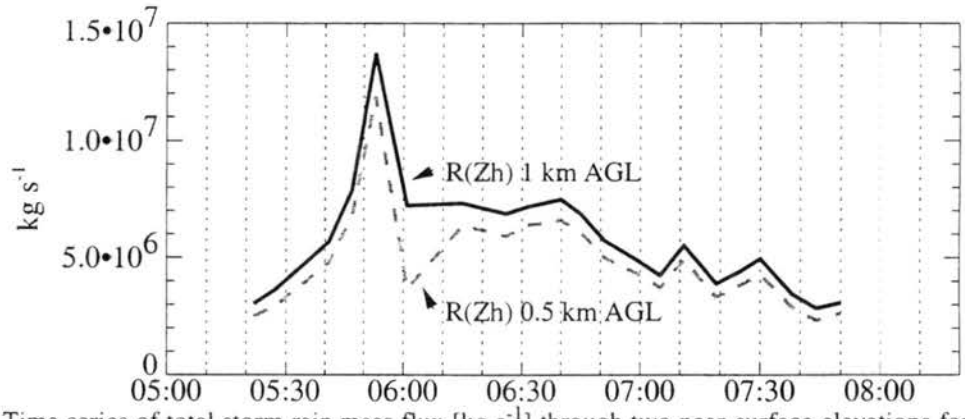

Fig. 4.1 Time series of total storm rain mass flux [kg s^{-1}] through two near-surface elevations for 23 Nov. Rain flux was estimated with the rainfall rate-reflectivity $R(Z_h)$ algorithm. Solid black line corresponds to 1 km AGL and dashed gray line corresponds to 0.5 km AGL.

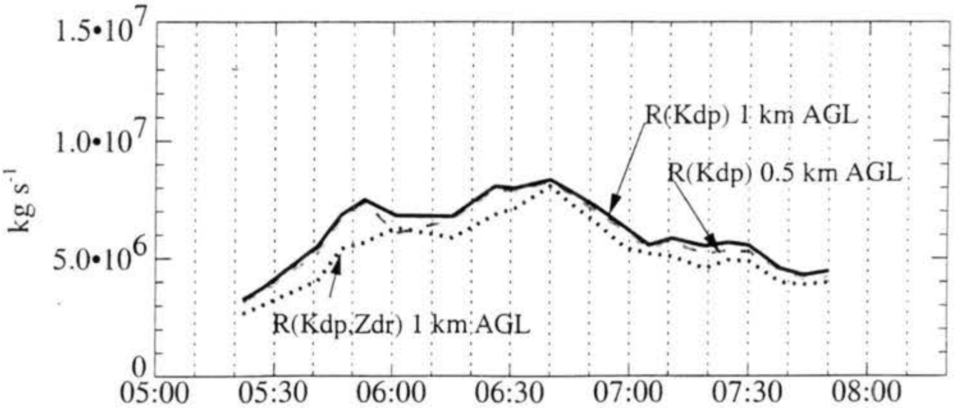

Fig. 4.2 As in Fig. 4.1 except solid black and dashed gray lines correspond to $R(K_{DP})$ estimates for 1 and 0.5 km AGL, respectively. Dotted line corresponds to the $R(K_{DP},Z_{DR})$ 1-km estimates.

The extreme peak in rain mass flux estimated by the $R(Z_h)$ algorithm early in the time series (Fig. 4.1) is notable because it translated to only a subtle maximum in the $R(K_{DP})$ time series (fig 4.2). High propagation differential phase shifts were measured behind (in a range sense) some very heavy rain cores in these radar volumes. This increased the sensitivity of the rain rate estimates to the chosen attenuation correction coefficient. Indeed, for this time (0553 UTC), the correction coefficient for horizontal attenuation a was quite high (0.17 dBZ per degrees of phase shift) compared to the average a for 23 Nov. (0.09 dBZ per degrees of phase shift). The linear regression used to estimate this a had one of the higher coefficients of determination (R^2=0.44) and a large number of samples, so 0.17 dBZ per degrees of phase shift was not replaced by a default average value (0.09 dBZ per degrees of phase shift). Admittedly, R^2 of 0.44 is still not indicative of a strong correlation, so the value of a is still not on solid statistical ground. Human error in the Ψ dealiasing process or the influence of extremely large raindrops (Mie scatterers) could have corrupted the calculated value of a. The actual value could be lower and bring the rain mass flux estimates using $R(Z_h)$ more in line with the $R(K_{DP})$ estimates. Of course the same could be said for all of the data in Fig. 4.1, but Mie scattering and human error were more likely an issue in the early stages when the rain cores were the most intense and the differential phase shifts were greatest. The values shown in Fig 4.2

were less sensitive to these attenuation issues since they relied heavily on attenuation-resistant K_{DP} for rain rate estimates.

Specific differential phase (K_{DP}) rain rate estimators hold several advantages over Z_h-based estimators, as summarized in section 2.3.2. The use of $R(K_{DP},Z_{DR})$ algorithms is not as well documented, but holds considerable promise due to the extra information Z_{DR} provides (Jameson, 1991) Although K_{DP} is relatively immune to variations in DSD (compared to Z_h), it is still a weak function of the median-volume drop size, D_0 (Ryzhkov and Zrnic, 1995a). Ryzhkov and Zrnic (1995a) found that the prime contributor to DSD induced errors in $R(K_{DP})$ was the uncertainty of D_0. By incorporating Z_{DR} into the R estimates, we better compensate for D_0 variation. As seen in Fig. 4.2, when the $R(K_{DP},Z_{DR})$ algorithm (eqn. 2.12a) was applied to our case study days, the rain mass flux trends were virtually identical to the trends derived from $R(K_{DP})$ (eqn. 2.12b). The flux magnitude was only slightly less. Therefore, unless otherwise noted, future references to radar rain rate estimates in this paper will imply rain rate estimates derived primarily from the $R(K_{DP}, Z_{DR})$ relation in eqn. 2.12a.

Using a simple $R(Z_h)$ relationship, Simpson et al. (1993) estimated the mean daily rainfall over the Tiwi Islands during the ITEX in 1988. Their 9-storm sample mean rainfall volume was 575×10^5 m^3, with a standard deviation of 246×10^5 m^3. Unfortunately, a direct comparison with estimates for 23 Nov. 1995 was not possible, since the early storm over northeast Melville Is. (0200-0400 UTC) and the first-order merger over north central Melville Is. (0445-0500 UTC) were only sampled with conventional, non-polarimetric radar scans (i.e. no Ψ, Z_{DR}, or $|\rho_{hv}(0)|$). The second-order merged cells that developed after 0500 UTC were measured dual-polarimetrically, so we can compare their estimated cumulative rainfall to the mean cumulative rainfall for second-order mergers estimated by Simpson et al. (1993). Simpson et al.

estimated 338×10^5 m^3 of rain was produced by second-order merged cells with a standard deviation of 302×10^5 m^3. Using all available polarimetric radar volumes (0522-0750 UTC), the accumulated rainfall for 23 Nov. was 489×10^5 m^3, well within the standard deviation of the Simpson et al. estimate. *Two* second-order merged cells contributed to this total and no attempt was made to remove contributions from isolated cells which formed after 0500 UTC. The estimated accumulated rainfall for our second case study day (27 Nov.) using all polarimetric radar volumes (0318-0950 UTC), was 529×10^5 m^3. If we limited the rain summation on 27 Nov. to times when a second-order merged cell existed (0537-0950 UTC), the total was 337×10^5 m^3, in good agreement with the estimates of Simpson et al. (1993).

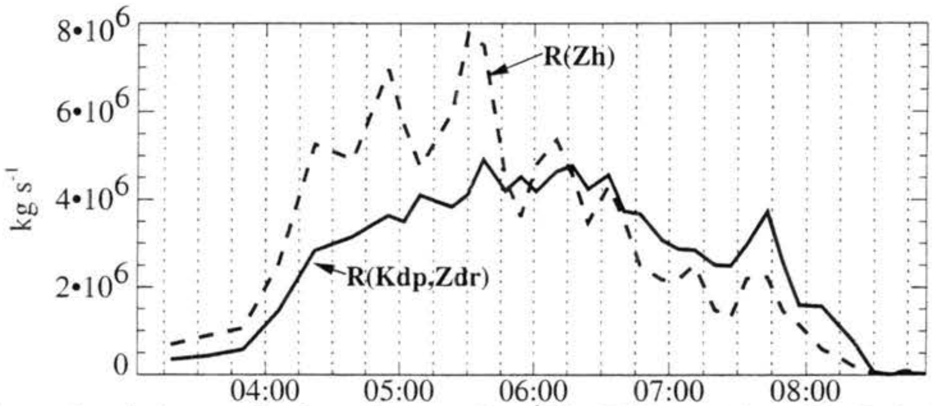

Fig. 4.3 Time series of rain mass flux for entire storm [kg s^{-1}] for 27 Nov. at 1 km AGL. Dashed line represents $R(Z_h)$ estimates and solid line represents $R(K_{DP},Z_{DR})$ estimates.

4.2 Cloud-to-ground (CG) lightning

No CG lightning flashes were detected near the shallow, precipitating cells that developed over the islands in the early morning and afternoon hours of 23 and 27 Nov. 1995. The CG-producing complex over far northeast Melville Island on 23 Nov. did occur relatively early, but it was not a shallow cell. The 40 dBZ horizontal reflectivity contour extended above 8 km AGL for at least 5-10 minutes. The fact that these early cells were not electrified to the point of producing lightning is consistent with the 59-day composite of ALDF-detected CG flash locations over Melville and Bathurst Islands compiled by Petersen

(1997). Petersen's (1997) composite of flash locations occurring between 0730 and 1130 LST highlighted the regions of low-level forcing associated with the land breeze and the collision of early sea breeze fronts along narrow peninsulas. These shallow isolated convective cells were rather weakly electrified compared to their afternoon counterparts, even though they produced heavy rain showers (Petersen, 1997). A number of factors could have facilitated warm-rain precipitation production in this tropical convection such as entrainment, water loading, low concentrations of cloud condensation nuclei, increased depth of the cloud below the freezing level and weak updraft speed in the low to mid-levels of the atmosphere. Most of the larger raindrops probably settled out of the cloud before they reached the -10°C level. The updrafts were evidently not strong enough to transport more than small graupel particles and ice crystals above this height. Hallett and Mossop (1974) and Koenig (1977) demonstrated that secondary ice processes such as rime-splintering may be important within *weak or dissipating* cloud circulations from -3 to -8°C. If small ice crystals proliferated above the freezing level in this manner, they could effectively short-circuit the NIC mechanism by glaciating all supercooled cloud liquid water. This process could be occurring in the quiescent early morning cells observed during the MCTEX.

Petersen's (1997) CG composite also illustrated the preponderance of CG's over the interior of the islands during the afternoon hours (1330-1730 LST). By this time, significant cloud merging and upscale development had typically occurred along the active sea breeze front. This convection was much more vertically-developed compared to the early morning cells, and radar observations suggested robust mixed-phase regions with large ice particles and supercooled water drops suspended above the 0°C level. This would be a favorable environment for electrical charge separation through NIC and would explain the bountiful CG strokes observed over the islands.

4.2.1 CG lightning and rainfall

Significant rainfall occurred after the peak CG activity, especially for 23 Nov. (see Fig. 4.4). For 23 Nov., the rain mass flux peak lagged the CG flash rate by about 19 minutes. After rising in tandem with the overall CG flash rate from 0522-0620 UTC, the rain mass flux continued to increase while the CG flash rate plummeted from 12 to 4 flashes min^{-1}. Following the peak estimated rainfall production at 0640 UTC, the precipitation rate remained fairly high through the end of the observation period (0750 UTC). However, during this period the CG rate decreased sharply.

To quantify the correlation between CG lightning flash rate and rain mass flux (RMF), the coefficient of determination was calculated (R^2). R^2 lies in the interval $0 \leq R^2 \leq 1$, with $R^2=0$ indicating no linear correlation between the two variables and $R^2=1$ indicating a perfect linear relation. If R^2 were close to one, then the excellent linear relation between the two variables would suggest that flash rate could be used as a predictor of RMF with great accuracy (and vice versa). However, a high R^2 would still not necessarily denote a causative relationship. The use of R^2 implies a best-fit line for (flash rate, RMF) data pairs. A R^2 of 0.6 would imply that the sum of squares of deviations about the best fit line is 60% less than the sum of squares of deviations about $\bar{y}$. A lower sum of squares of deviations implies a better correlation.

This statistical method has its weaknesses because it does not account for possible non-linear relationships between the two variables and it is not resistant to outliers (Wilks, 1995). However, the R^2 value will provide a benchmark for comparing various strengths of relationships. If two variables consistently increase and decrease with each other in time, then they will be positively correlated. They will exhibit a R^2 that is higher than the case of two variables that are intermittently positively and intermittently negatively correlated. R^2 will also be sensitive to the extent that the largest values of one variable are coincident with the largest values of the other variable.

The coefficient of determination (R^2) between CG lightning flash rate and RMF was 0.12. R^2 was maximized if a time lag of 19 minutes was applied to the rain mass flux data. In this case, R^2 topped out at 0.45.

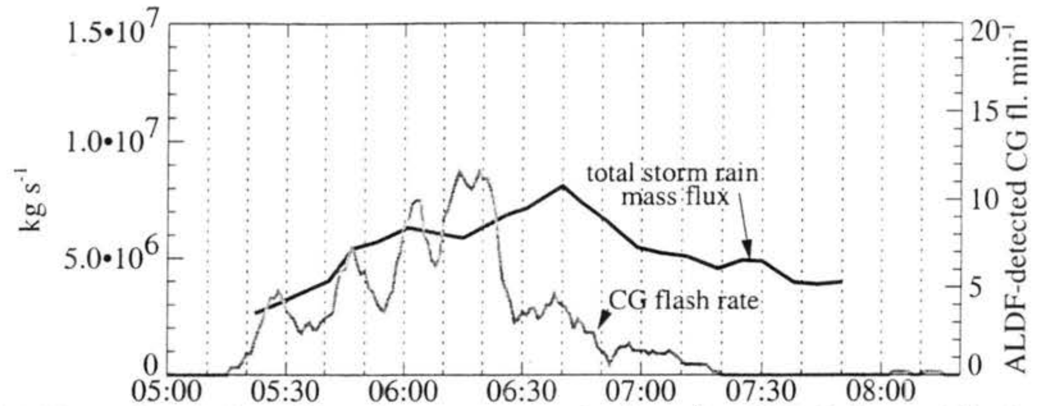

Fig. 4.4 Time series of 1 km AGL total storm rain mass flux [kg s^{-1}] and CG flash rate within the radar domain for 23 Nov. 1995. Rain estimates are only plotted at times associated with dual-polarimetric radar volumes (0522-0750 UTC). In this figure and in subsequent figures, the lightning flash rate is a 5-minute running average of 1-min flash rates.

On 27 Nov., the trends of CG flash rate and estimated rain mass flux were well correlated in time, with no significant time lag between the two time series (Fig. 4.5). However, as with 23 Nov., rapid changes in the CG flash rate were not accompanied by rapid changes in rain mass flux. The relative smoothness of the rain mass flux time series was partly due to the 6-10 minute temporal resolution of the radar data, but since the point-to-point variation (on a 6-10 minute time scale) was fairly small, this suggests a relatively steady production of rain in comparison to the CG flash rate. R^2 was 0.39 in this case, and was maximized with no time lag.

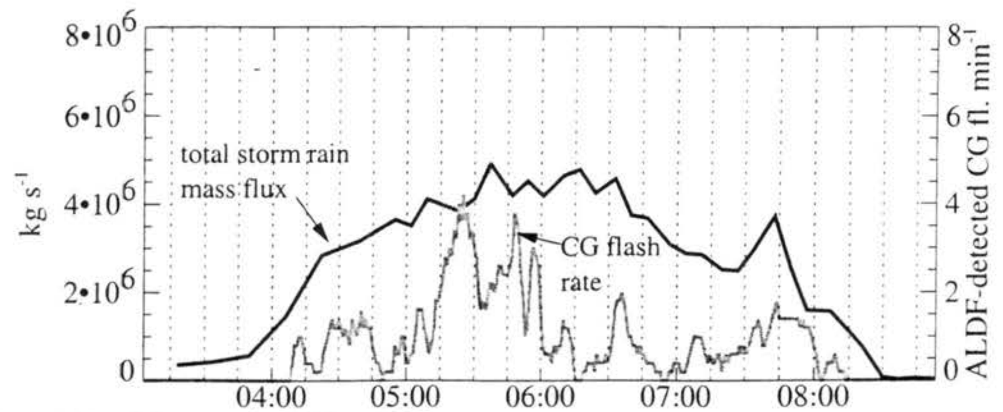

Fig. 4.5 As in Fig. 4.4 except for 27 Nov. 1995 case.

The relation between rain mass flux and electrical activity is not flushed out by cloud-to-ground flash measurements alone since CG flashes are only part of the electrical picture. Low CG flash rates do not necessarily coincide with suppressed in-cloud (IC) lightning activity. In our case study days, however, microphysical evidence suggested that IC flashes were not exceptionally numerous during episodes of low CG flash rates. In most instances, CG flash rates within the range of the flat plate antenna were correlated with the total flash rate (IC and CG) detected by the antenna. This subject will be explored further in section 4.3.

4.2.2 Correlation of CG lightning with precipitation in mixed-phase region

Unlike rain mass flux, the graupel mass in the mixed-phase region between 0 and -40°C (estimated from polarimetric radar) closely followed the CG flash rate. These findings are illustrated by the time height sections shown in Fig. 4.6 and 4.7. R^2 between total graupel mass in the mixed-phase region and the 5-min running average of CG flash rates for 23 Nov. was 0.75. R^2 topped out at 0.80 with a CG flash rate lag of 5-8 min. (i.e. graupel mass peaked before CG flash rate by 5-8 min.). For 27 Nov., the maximum R^2 for the same two fields (Fig. 4.7) occurred at zero time lag with an R^2 of 0.67. These R^2 values indicate that CG production was more closely linked to the amount of graupel in the mixed-phase region than to the low-level rain mass flux. This is consistent with past studies that found a significant correlation between CG activity and the thunderstorm precipitation ice phase (Carey and Rutledge, 1996), and found only conditional success linking CG activity to surface rainfall (e.g. Williams et al., 1992; Petersen, 1997).

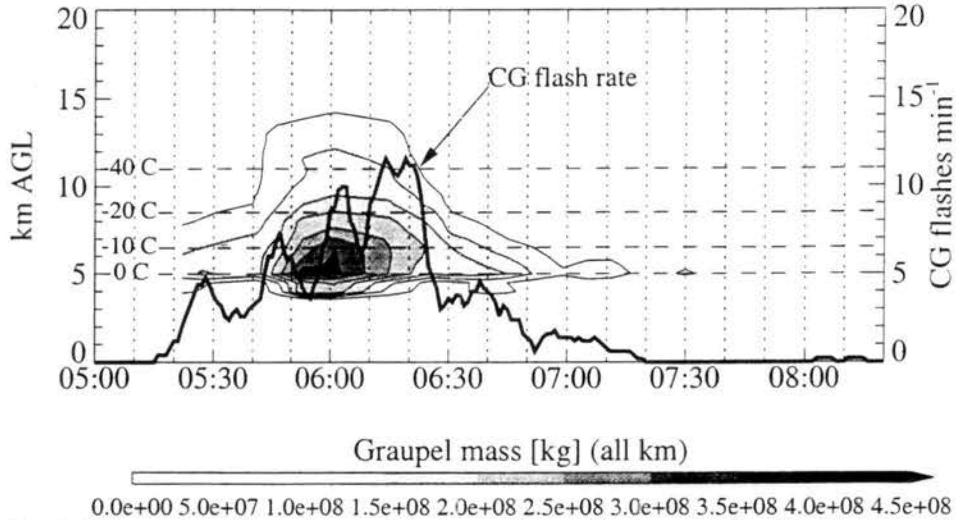

Fig. 4.6 Time height section of large ice particle (graupel) mass [kg] per 0.5-km thick horizontal slab (contoured) for 23 Nov. 1995. Environmental temperature is contoured with horizontal dashed lines. CG flash rate within radar domain indicated by solid line.

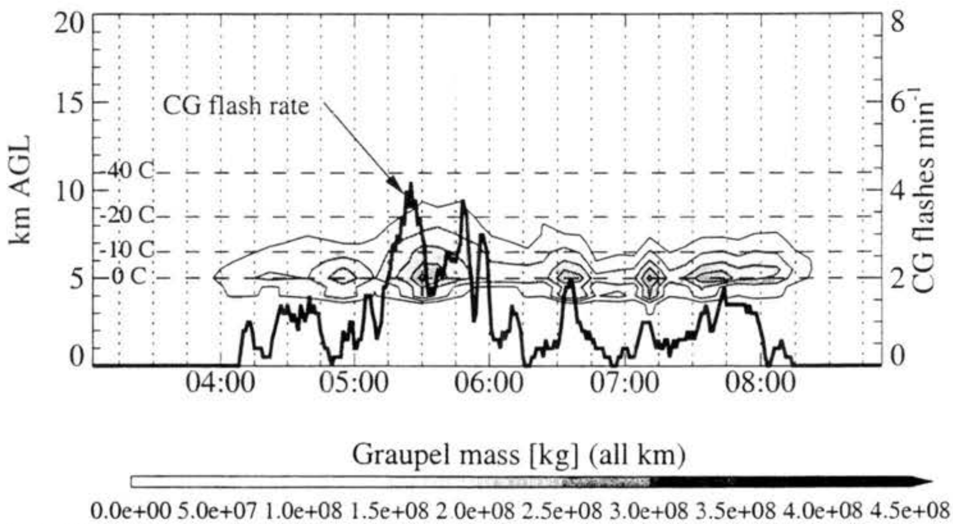

Fig. 4.7 As in Fig. 4.6 except for 27 Nov. 1995 case.

In addition to the graupel mass in the mixed-phase region, the precipitation-sized liquid water mass in the mixed-phase region was also estimated for each polarimetric radar volume. A time series was constructed for 23 Nov. and is shown in Fig. 4.8. The time series indicated that the evolution of supercooled precipitation-sized liquid water was very similar to that of graupel mass for the same day, and that the CG flash rate once again lagged this precipitation field (R^2 was 0.60 at zero lag and 0.73 at -9 min. lag).

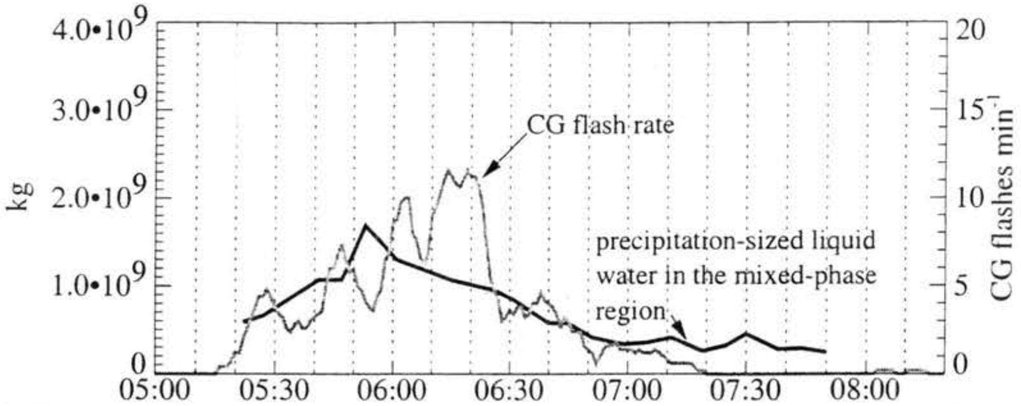

Fig. 4.8 Time series of precipitation-sized liquid water mass [kg] above the freezing level in the entire radar domain for 23 Nov. 1995 (solid black). CG flash rate within the radar domain is in solid gray.

A similar time series was constructed for 27 Nov. (shown in Fig. 4.9). The massive injection of supercooled raindrops above the freezing level around 0745 UTC was probably a real event, but the magnitude of the peak is questionable. By this radar volume time, the leading edge of the squall line to the west was already 100 km from the radar. With low-level radar scans spaced by about 1.6° in elevation, the vertical resolution of radar data at 110 km range was greater than 3 km. The trend in the vertical distribution of liquid water mass after 0645 UTC (time-height section in Fig. 4.10) suggested that the precipitation estimates suffered from poor vertical resolution at larger ranges. Due to the poor vertical resolution at great ranges, the high reflectivity and differential reflectivity associated with the heavy rain below the freezing level contaminated a large number of grid points above the melting level. There probably was much less precipitation-sized liquid water above the melting level than suggested. The computer program that converted the radar data from polar to Cartesian coordinates used an elevation radius of influence of 2°. This also "smeared" the radar data in the vertical, especially at distant ranges. The 23 Nov. data did not suffer noticeably from poor vertical resolution since the event was much closer to the radar.

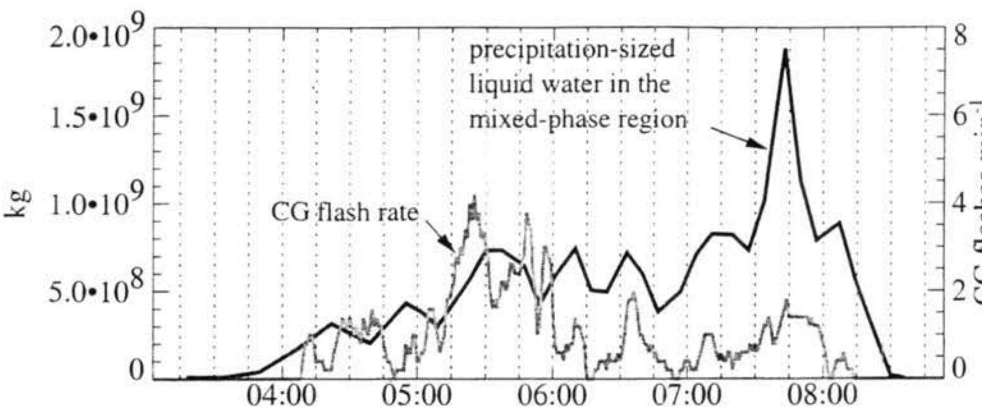

Fig. 4.9 As in Fig. 4.8 except for 27 Nov. 1995 case.

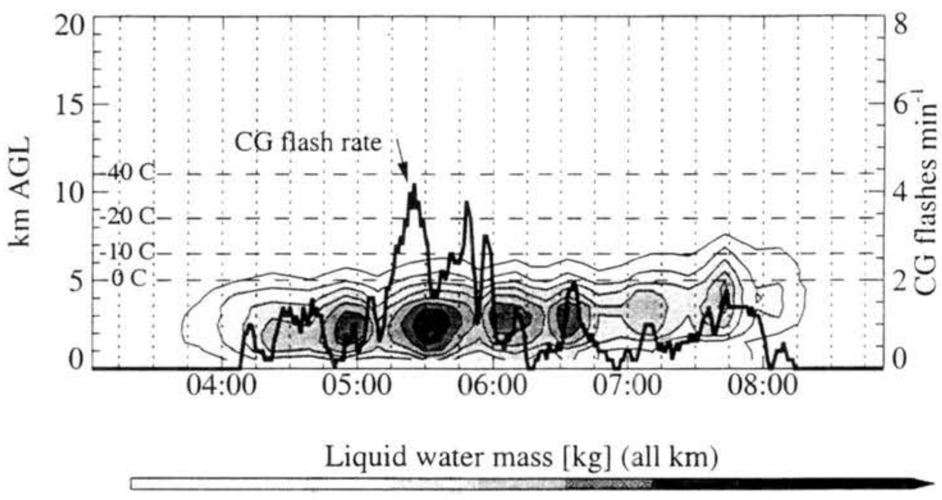

Fig. 4.10 Time height section of precipitation-sized liquid water mass [kg] per 0.5-km thick horizontal slab (contoured) within the radar domain for 27 Nov. 1995. Environmental temperature contoured with horizontal dashed lines. CG flash rate indicated by solid line. Note the tendency for the liquid water to rise in elevation towards the end of the day. As explained in the text, this may be a radar artifact.

Since high concentrations of graupel were correlated to peaks in CG flash rate, this suggests a precipitation-based electrification. The precipitation-sized liquid water above the freezing level can be considered a tracer for graupel. Since precipitation liquid water content matched well with graupel mass in the mixed-phase region, it is proposed that graupel was formed by the lofting and freezing of supercooled water drops.

4.2.3 Positive CG's

Positive CG's were not very common during the MCTEX. The fraction of positive CG's to all CG's was only 0.02. This low fraction was consistent with other observational studies in the tropics and supported the general tendency for the percentage of positive CG flashes to increase with latitude (Baral and Mackerras, 1993; Mackerras and Darveniza, 1994). The reason for the smaller fraction of positive CG in the tropics is not clear, but it may be related to the increased separation of the positive charge region from the ground due to the higher tropopause, or to weak vertical wind shear in comparison to higher latitudes.

Insight into the charge structure of the tropical thunderstorm was provided by the ground flash locations of positive CG discharges on 23 Nov. On this day, the positive CG flashes were typically displaced to the southeast of the negative CG flash locations. Considering that strong upper-level winds from the northwest sheared the thunderstorm anvil towards the southeast, it may be possible that the positive CG's originated from the reservoir of positive charge typically found in the upper-levels of the cloud. (Note the displacement of the anvil to the southeast in the visible satellite image in Fig. 3.12). This supported the conceptual dipole model of the thunderstorm charge structure. In the presence of wind shear, the positively-charged ice crystals in the upper-levels would be displaced southeastward relative to the low levels of the cloud and therefore would no longer be shielded from the ground by the lower negative charge. This would facilitate electrical breakdown between the anvil and the surface. This "tilted dipole" theory has been forwarded by several investigators as an explanation for positive CG flashes (e.g. Brook et al., 1982; Engholm et al., 1990; MacGorman and Nielsen, 1991; Carey and Rutledge, 1998). The following figures appear to support this explanation, assuming that the flash channels were more-or-less vertically oriented, or only slightly tilted. Fig. 4.11 indicates 3 positive CG's displaced downwind from the main storm, possibly discharging from the anvil. The same pattern is evident from 0601 to 0606 UTC in Fig. 4.12. A similar pattern emerged between 0655 and 0710 UTC, when 5 positive CG's were detected downwind (southeast) of the north-central Melville cells (not shown).

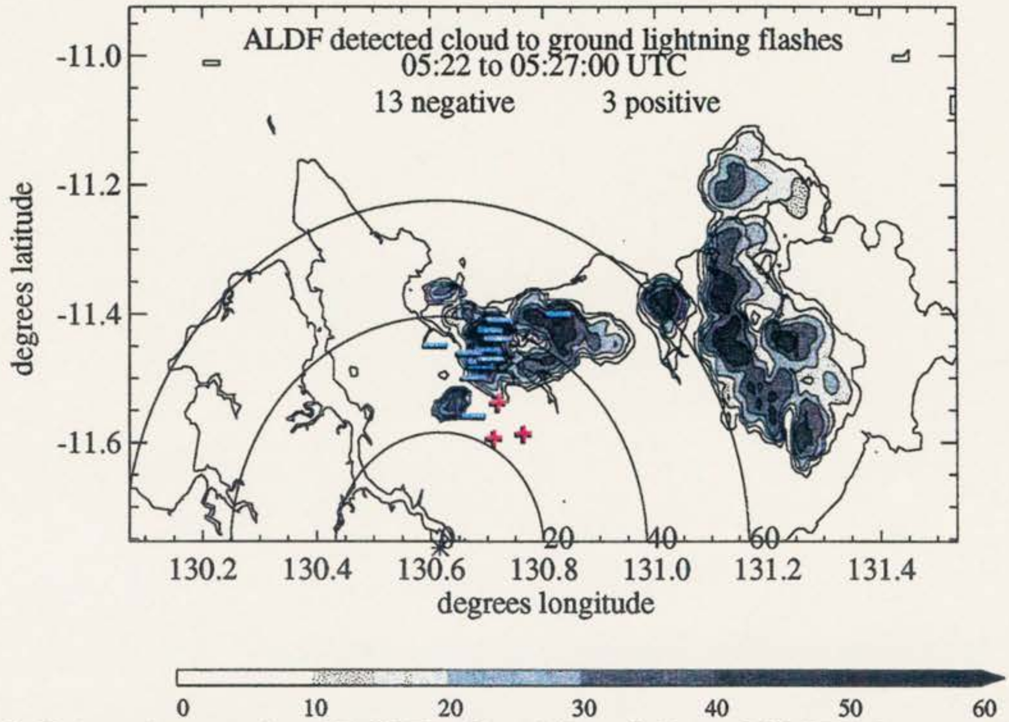

Fig. 4.11 Horizontal cross section of Z_h [dBZ] at 2 km AGL on 23 Nov. at 0522 UTC. Locations of negative (blue minuses) and positive (red pluses) CG flashes are shown for the indicated time interval. Asterisk denotes radar location and range rings are spaced every 20 km.

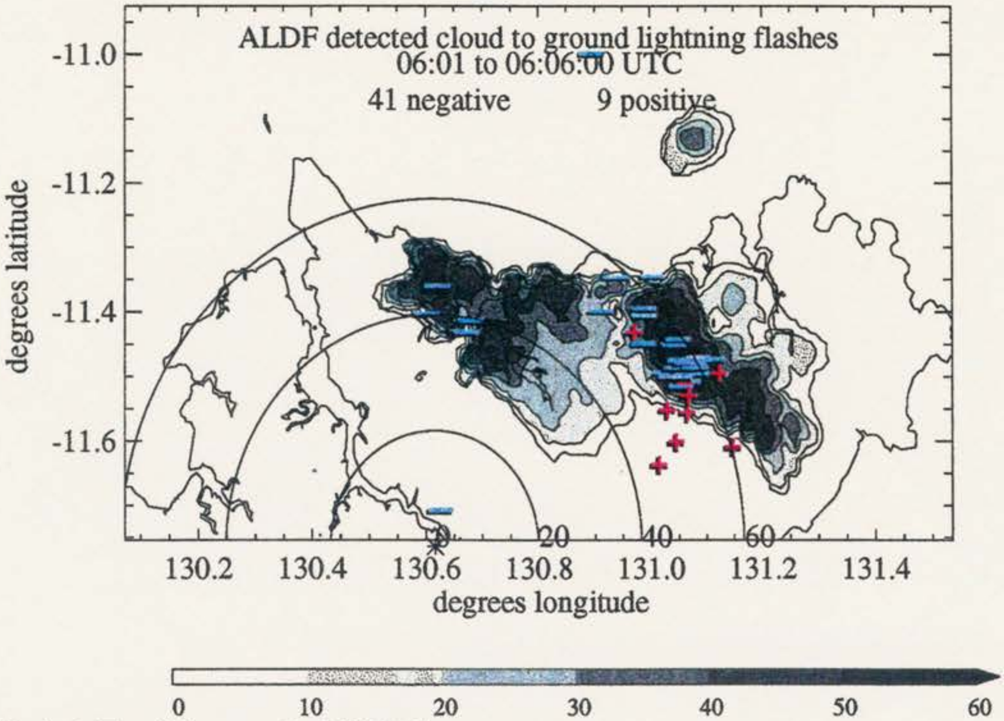

Fig. 4.12 As in Fig. 4.11 except for 0601 UTC.

Most of the remaining positive CG's were located in the midst of heavy convective precipitation, coexisting with numerous negative flashes. Here, it was less plausible to attribute the positive CG's to the storm-relative horizontal displacement of positively charged ice crystals in the upper levels of the storm. Several alternative explanations for positive CG's have been proposed. Marshall and Winn (1982, 1985) and Jayaratne and Saunders (1984; 1985) described how graupel can charge positively in an environment warmer than the charge reversal temperature (near -10°C), and create a lower positive charge region through non-inductive charging. The laboratory work of Takahasi (1978) suggested that this "charge reversal" would occur at any temperature if the liquid water content were high enough (i.e. >4 g m^{-3}). Several investigators (e.g. Williams et al., 1991; MacGorman and Nielsen; 1991; MacGorman and Burgess, 1994) postulated that ice particles charged in such a manner in the lower parts of the cloud could initiate positive ground flashes. However, this "inverted dipole" can form only if the ice crystals rebound from the larger graupel particles after collision. If the graupel particles are experiencing wet growth, then the colliding ice crystals would probably stick to the graupel and NIC would cease (Saunders and Brooks, 1992). Carey and Rutledge (1998) showed that an "inverted dipole" (in which positive charge was carried by the large ice particles) was not a likely mechanism for the positive CG lightning observed in a severe NE Colorado hailstorm. In the Carey and Rutledge case study, heavy precipitation and positive CG lightning were spatially and temporally anti-correlated.

Perhaps the numerous negative CG's facilitated the positive CG's observed within heavy precipitation cores during the MCTEX. Negative CG's could neutralize much of the negative charge in the lower levels of the storm, thereby exposing the upper positive charge to the surface (Pierce, 1955). Another possible mechanism involves the enhanced precipitation current to the ground within heavy rainfall (Carey and Rutledge, 1998). Predominately negatively charged drops may transport a significant amount of negative charge to the surface, adding an extra sink for the lower negative charge. The positively-charged ice crystals in the upper levels of the storm could then be "unshielded" from the ground following the rapid loss of negatively charged raindrops. This would increase the likelihood of positive ground flashes. In the MCTEX, heavy rain rates (i.e. >100 mm hr^{-1}) were often collocated with positive CG flashes, making this a plausible explanation. However, without knowing the vertical extent of the positive CG flash channels, we can not definitively say which is the best explanation for the positive CG's detected in MCTEX thunderstorms.

Only 5 positive CG's were detected in the 27 Nov. storm, and each flash was situated near a heavy convective core. None were associated with the stratiform precipitation region trailing the weak squall line that formed over southern Bathurst Is. As during other MCTEX days, the electric field mill sensor indicated net positive charge aloft during this period. Observational studies have shown that this is often a preferred region for positive cloud-to-ground discharges. The appearance of the prerequisite positive charge aloft could be due to the advection of positively charged ice crystals from the upper levels of the leading convective line and/or in-situ charging within the stratiform anvil (for discussion on this topic, see Rutledge and MacGorman, 1988; Rutledge et al., 1993; Stolzenburg et al., 1994; Rutledge and Petersen, 1994). During the MCTEX, there were few examples of positive CG flashes within the trailing stratiform precipitation of squall lines.

4.3 Total flash rate

In-cloud (IC) lightning flashes typically occur more frequently than cloud-to-ground (CG) lightning flashes. Since the main negative charge layer in a thunderstorm is usually closer to the upper positive charge region than to the ground, the electric field (modulated by conductivity of the intervening air) is typically greater between the two charge centers and promotes IC over CG lightning. IC lightning usually begins before CG activity, so it can be the first indicator of significant electrical charge separation at work in a developing storm. For this reason the flat plate data set (in conjunction with multiparameter radar data) was a valuable resource for testing precipitation-based theories of cloud electrification.

Some past studies related convective cloud top height to flash rate (Williams, 1985; Price and Rind, 1992; 1994). More success has been found with correlating flash rate and the degree of convective vigor in the mixed-phase region, as inferred by high reflectivity at temperatures colder than 0°C (e.g. Michimoto, 1991; Zipser, 1994; Petersen et al., 1996). Carey and Rutledge (1996) and Goodman et al. (1988) used dual-polarimetric radar to make more quantitative measurements of ice-phase precipitation, comparing lightning flash rates to the estimated volume of large ice particles in the mixed-phase region of the storm. Some storms are very tall, but do not contain updrafts strong enough or wide enough to drive electrification mechanisms to the point of causing lightning. These cells cannot support a large number of supercooled water drops and graupel particles above the freezing level and are often entirely glaciated. They do not have much radar-inferred ice and raindrop mass concentrated above the freezing level. This type of convection is characteristic of tropical oceanic convection (Black et al., 1993; Zipser, 1994). This decoupling of electrical activity and cloud top height renders electrical parameterizations based on cloud top height useless (e.g. Price and Rind, 1992) on a case-by-case basis. For these reasons, we examined the trend in observed flash rates over the Tiwi Islands and compared it to radar estimates of large ice particles and precipitation-sized supercooled liquid water in the mixed-phase region of the storms.

The flat plate antenna located at the C-pol radar site detected electrostatic field excursions associated with both CG flashes and in-cloud (IC) flashes, providing an estimate of the total lightning flash rate for storms within the detection radius of the antenna. The electrostatic field strength from an electric dipole varies roughly as the inverse cube of the distance from the dipole. This results in a fairly sharp drop-off in detection efficiency beyond 40 km range for the flat plate antenna.

4.3.1 23 November total flash rate

Figure 4.13 shows a time height section of graupel mass for 23 Nov., estimated by the C-pol radar. Superimposed on the graph is the total flash rate as detected by the flat-plate antenna. Consistent with the NIC theory, the appearance of large graupel mass above the freezing level was coincident with the first surge in flash rate from 0520 to 0530 UTC. Before this time, aside from the 13-km high storm over north-east Melville, most of the precipitation was confined below 7 km, probably formed through warm-rain processes. According to NIC theory, which requires ice particle interactions in the presence of supercooled water to separate electrical charge, lightning should not occur under the absence of ice. The flat plate antenna record is consistent with this since flashes were not detected until the storms were significantly above the freezing level. The first surge in flash rate from 0520 to 0530 UTC was associated with the first and second-order cell mergers that took place over north-central Melville Island about 40 km north of the radar (Fig. 4.13). The flash rate continued to rise after 0540 UTC while the mixed-phase graupel mass trailed off. This was not consistent with NIC theory, which would predict the lightning production rate to follow the total graupel mass--perhaps lagging total graupel mass by 10-15 minutes to account for the sedimentation time required to separate the oppositely-charged graupel particles and small ice crystals within the updraft. It is important to realize, however, that this second surge in flash rate began at the same time that the intense second-order merged cell developed about 60 km to the northeast of the radar. Perhaps the flat plate antenna detected a significant number of flashes from this more distant, but more powerful storm. To investigate this possibility, the graupel mass in the mixed-phase region was compared to the total flash rate without limiting the radar estimates of precipitation to regions within a certain range of the flat plate. The results are shown in Fig. 4.14. As indicated by this figure, the correlation between estimated graupel mass and flash rate is much improved by increasing the radar range limit. This is because most of the deep convection was located on the fringe of or beyond the estimated detection range of the flat-plate antenna. Fig. 4.15 shows a map of cumulative rainfall for 23 Nov. (0522-0750 UTC). This map illustrates the problem at hand. Assuming the heaviest precipitation was associated with the deepest convection, one can see that these vigorous storms were beyond the unambiguous detection range of the flat-plate (i.e. 30-35 km). Including radar data within radar ranges spanning 40 to 60 km greatly impacts the magnitude of estimated graupel mass in the mixed-phase region. Therefore, even though the peak lightning flash rate was not correlated with the peak estimated graupel mass in the mixed-phase region in Fig. 4.13, this is not convincing evidence against NIC theory. Since most of the convective complex occurred outside of 40 km range, and the flash rates detected by the flat plate were still very high, this suggests that including radar data from beyond 40 km is warranted. Exactly how much beyond 40 km is debatable, but expanding the radius of influence did bring the evolutions of the two fields virtually in phase with each other (Fig. 4.14), which precludes us from abandoning a precipitation-based explanation for the observed electrical behavior of the storm.

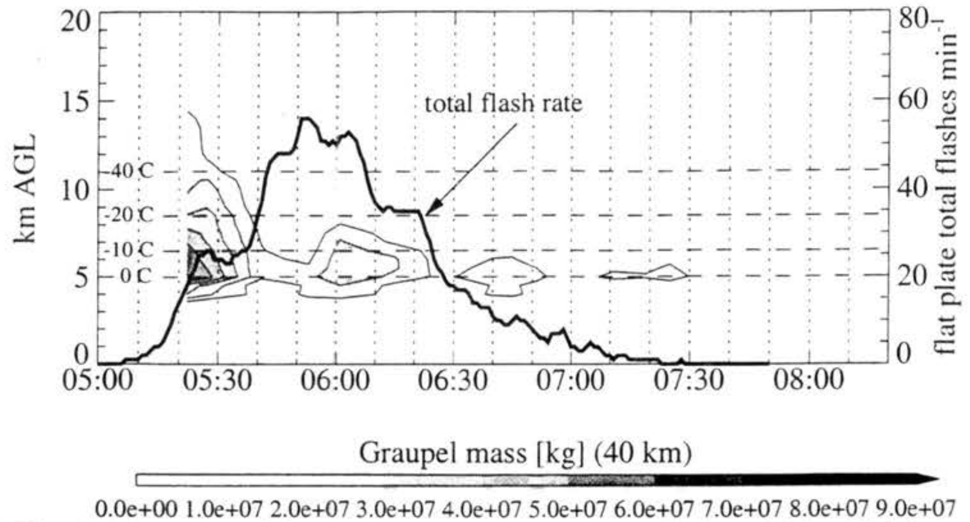

Fig. 4.13 Time height section of C-pol radar-estimated graupel mass [kg] per 0.5-km thick horizontal slab within 40 km of the flat plate antenna (contoured) for 23 Nov. 1995. Total flash rate shown by solid line.

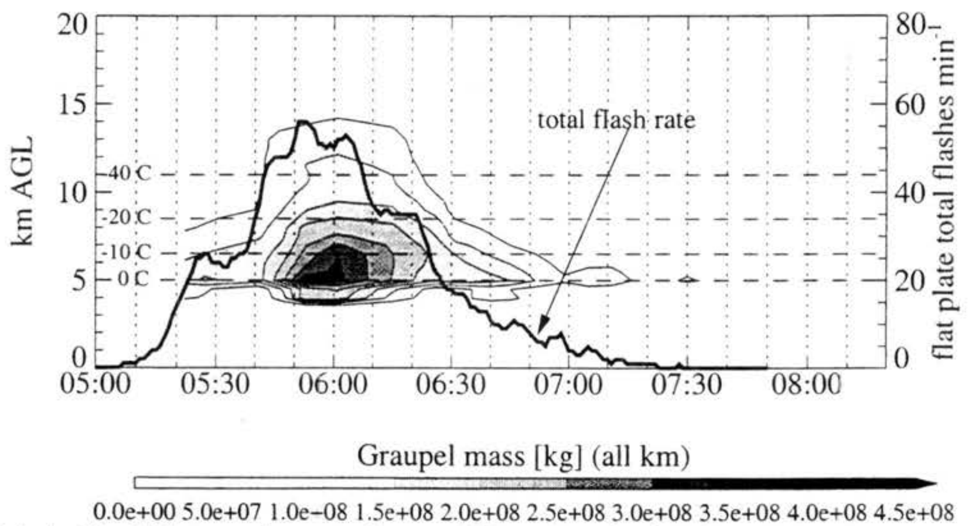

Fig. 4.14 As in Fig. 4.13 except for graupel mass within entire radar domain.

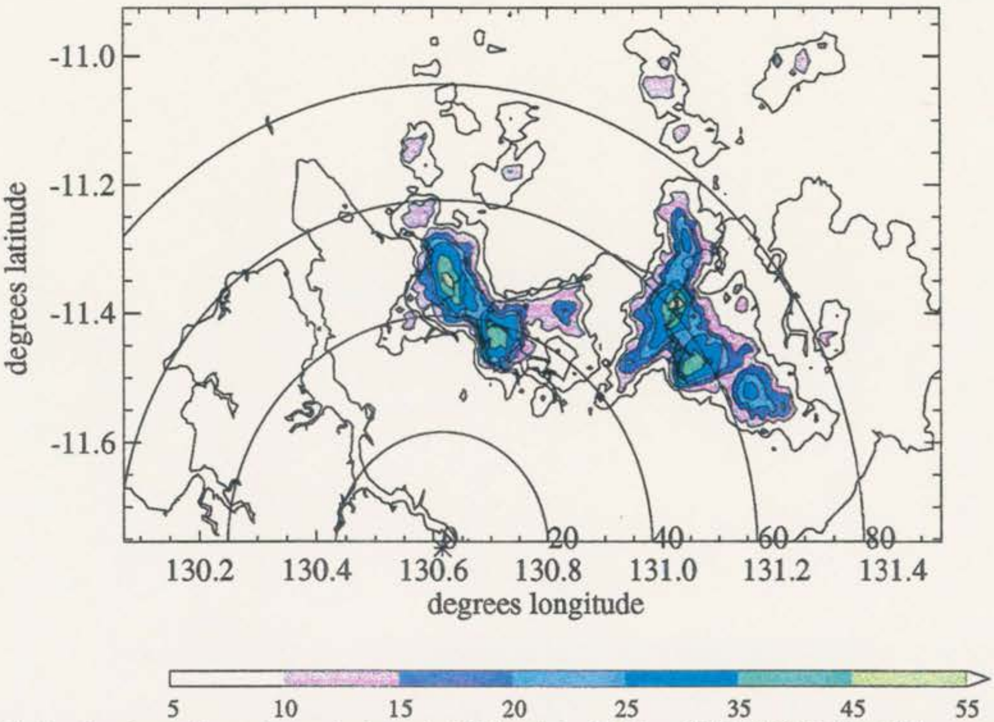

Fig. 4.15 C-pol radar-estimated cumulative rainfall [mm] for 23 Nov. 0522-0750 UTC. 20-km range rings centered on radar location (asterisk) with coastlines of Bathurst and Melville Islands indicated.

4.3.2 27 November total flash rate

Figure 4.16 depicts the relation between total flash rate and total graupel mass in the mixed-phase region near the flat plate antenna (similar to Fig. 4.13) for 27 Nov. The total graupel mass distribution was somewhat sensitive to how far from the radar one chose to incorporate the radar data, but unlike 23 Nov., the temporal spacing of the graupel maxima was not too sensitive to the chosen range. Fig. 4.16 illustrates that from 0400-0500 the total lightning production, as measured by the flat plate antenna, was correlated with the estimated graupel mass in the mixed-phase region. For subsequent times, the relation was less clear. The total flash rate began an exceptional rise at 0615 UTC and remained above 20 flashes min^{-1} until 0633 UTC. The absolute peak of 45 flashes min^{-1} was by far the greatest of the day. There was virtually no increase in storm graupel mass, however. The total flash rate record appears to stand by itself during this time, and is not consistent with most radar data.

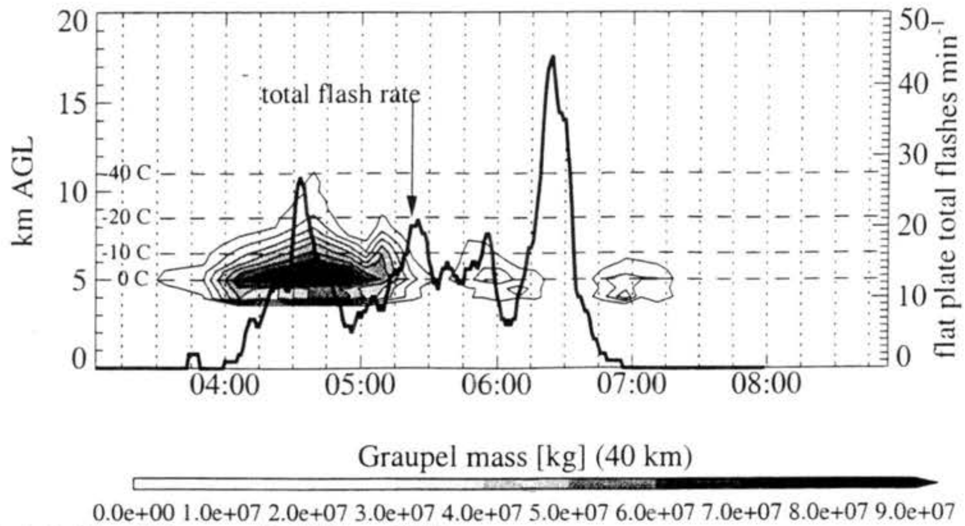

Fig. 4.16 As in Fig. 4.13 except for 27 Nov. 1995 case.

There was short-lived deep convection within the range of the flat plate antenna during this time, but the cells were narrow, and did not appear capable of producing a large quantity of lightning, as the flat plate record would suggest. For this reason, the flat plate record is suspect. It was not ignored however, because there was no hard evidence of rain-contamination (no rain was reported by observers or registered by the AWS) and there was a thunderstorm in the vicinity. The ALDF network did detect several CG's from these cells, but not an inordinate amount (as shown by the total CG flash rate trend in Fig. 4.7). Therefore, if the total flash rate count was indeed real from 0615-0635 it was largely due to in-cloud flashes. What could cause such a large surge in the in-cloud flash rate?

Some authors have attributed exceptionally high IC:CG flash rate ratios to an intense updraft (e.g. MacGorman et al., 1989; MacGorman and Nielsen, 1991). Instead of residing at their normal elevation, the negatively charged particles are lofted to higher levels, and cannot interact as easily with the ground through CG lightning. The closer proximity of the main negative layer to the upper-level positive charge and the smaller breakdown field at higher altitudes in the storm would encourage more rapid IC flash production. It seems unlikely that the storms over western Melville Island were capable of producing such an elevated electrical charge structure. No significant graupel mass was observed in the mixed-phase region of the storm which suggests that there was no significant layer of negative charge in the mixed-phase region that could participate in vigorous IC flash production.

Another possible explanation involves the thunderstorm anvil that was generated by the deep convection to the west of the radar. At that time, the anvil was spreading over the radar site and over the cells that could have been responsible for the in-cloud lightning detected by the flat plate. It has been suggested that over the lifetime of a thunderstorm, the tendency to shift from primarily IC production to more CG production is due to the formation of lower positive charge (Jayaratne and Saunders, 1984; Williams et al., 1989) and/or due to a tendency for the storm to gain net negative charge with time. The latter explanation applies when positive charge is lost from the upper levels of the storm (Solomon and Baker, 1994). This positive charge loss could be attributed to the divergent outflow near the top of the storm advecting positive charge away from the storm cells or to the tendency of negative ions to more readily attach to and neutralize the positively-charged part of the cloud due to the increase of air conductivity with height (Krehbiel, 1986). If the main positive charge reservoir dissipated as a result of these processes, then the electric field below the main negative charge region could become comparable to that above the charge region (especially if lower positive charge developed), thereby increasing the probability of ground flashes. Now consider the advection of the anvil over the storm cells. Assuming that the ice crystals in the anvil were positively charged, as is usually the case, this could augment the electric field above the main negative charge region in the isolated cells and facilitate in-cloud flashes. Importing this positive charge aloft could stimulate more electrical discharges between the main negative charge and the upper levels of the storms.

An actual electricity-based explanation for the estimated total flash rate peak seems inappropriate, however, mainly because the storms did not look like the most impressive convection of the day on radar.

The ground flash activity was not distinctive at this time, apart from its tendency to follow the surges in estimated graupel mass in the mixed-phase region. Possible non-lightning explanations for such a dramatic flash rate increase include problems with the flash count algorithm and/or rain contamination. Perhaps the antenna was affected by rain while the AWS did not intercept enough precipitation to activate the tip bucket (0.2 mm per tip). If the flat plate antenna was indeed rained upon, the water could short circuit the metal plate and cause erratic voltage fluctuations to be mistaken for lightning flashes by the post-processing flash count algorithm. This phenomenon was observed on several other MCTEX days when rain fell on the flat plate antenna.

4.4 Impact of mergers on electrical activity

The first incidence of lightning in a storm cell was always preceded by significant cloud top growth and the formation of some graupel aloft. The enhanced vertical growth was usually a result of a first or second-order cloud merger. Not all the merged cells produced lightning, but if they produced 40 dBZ precipitation above 10 km AGL, this virtually ensured at least one CG discharge. The flat plate antenna probably captured the initial electrical discharge on 27 Nov., but was not in a position to capture the total lightning trends associated with cloud mergers for the rest of 27 Nov. or for 23 Nov.

The ALDF network covered the entire island, so at least CG flashes were consistently captured during the course of cloud mergers. The exponential increase in CG production associated with the first and second-order mergers is apparent in the time height sections of reflectivity shown in Figs. 3.8 and 3.17. These figures followed the development of individual cells as they merged and evolved over the Tiwi Islands, and they indicated the number of CG flashes detected within 6 km of the cell and within 5 minutes of the start of each radar volume. On 23 Nov., the CG flashes were initiated just after the cell underwent a second-order merger (~0530 UTC). For 27 Nov., the ground flashes started soon after the second-order merger around 0420 UTC. Possible microphysical explanations for this will be discussed in Chapter 5. After the second-order mergers, the CG flash rates surged briefly, and then settled back to intermediate values. The convective intensity pulsed every 1/2 hour or so after that and produced similar pulses of CG activity.

CHAPTER 5

Summary and Discussion

The MCTEX provided a unique opportunity to explore the dynamical and electrical structure of tropical island thunderstorms during the transition season in the Maritime Continent. Convective initiation processes were explored, and the interaction between cool pools and the sea breeze front was investigated. The convective evolution of island thunderstorms was also documented in the context of cloud merging. Precipitation and electrical time series of the storms were produced and analyzed for two case study days. This yielded additional evidence supporting the non-inductive graupel-ice charging theory, or NIC theory.

A diurnally forced thunderstorm complex was observed every MCTEX day between 21 November and 3 December 1995. Even when monsoon conditions prevailed, with nocturnal oceanic convective systems propagating over the islands, the islands still were a site for afternoon convection. These instances usually resulted in late-developing and less vigorous complexes. The amount of low-level precipitable water also strongly regulated the intensity of the afternoon thunderstorms.

A dual-polarization C-band Doppler radar gathered kinematic and microphysical data over the Tiwi Islands and permitted a detailed study of diurnally-forced thunderstorms for two case study days during the MCTEX. First, C-pol radar data was corrected for precipitation attenuation using a method that relied on propagation differential phase shift, similar to Ryzhkov and Zrnic (1995b). In some cases, attenuation accounted for an almost 50% drop in estimated rain mass flux using a Z_h-based rain rate relationship.

Rain mass flux estimates that incorporated dual-polarization measurands (e.g. K_{DP}, Z_{DR}) were much less sensitive to attenuation by precipitation.

5.1 Convective organization

Nocturnal radiational cooling of the islands produced a weak temperature inversion with nearly saturated conditions near the surface by morning. The boundary layer over the Tiwi's recovered rapidly once solar heating began. By afternoon, a well-mixed adiabatic layer about 1-2 km deep developed with a shallow superadiabatic layer near the ground.

C-pol radar and satellite pictures indicated boundary layer organization in the form of horizontal convective rolls (HCR's) over the islands on some days. In accordance with dynamical theory, these longitudinal cloud lines were aligned almost parallel to the low-level shear vector and were observed on days having a distinct jet-like vertical profile in the trade wind. Some evidence of interaction with the sea breeze front was apparent on 23 Nov.

The isolated precipitating cells of early morning and afternoon rarely had 30 dBZ reflectivity above the freezing level for more than a couple minutes, but they exhibited reflectivities as high as 50 dBZ in the warmer parts of the cloud. Entrainment, weak low-level updrafts, a high 0°C level, and a low concentration of cloud condensation nuclei characteristic of maritime environments probably made them efficient warm-rain producers. When the cells originated over the leeward coast sea breeze front, they dissipated quickly atop the cooler oceanic air and dropped their precipitation behind the front. The rain-cooled downdrafts probably reinforced the maritime characteristics of the air mass behind the sea breeze front. When the shallow cells developed over the island interior, they sometimes produced reflectivity signatures suggestive of weak cool pools situated beneath them. The edges of these features propagated ahead of the precipitating cells, but their speed was slightly slower than expected from density current theory.

Consistent with past studies, the most active convection was initiated over the sea breeze front for which the environmental flow was offshore. This is where the convergence due to the sea breeze circulation was maximized. An aircraft transect of Melville Is. at 340 m altitude revealed a 3 K virtual temperature (1% density) discontinuity across the leeward coast sea breeze front. Over the island interior, the evolution of the mixed layer was also illustrated. As the cool moist oceanic air mass flowed inland over the windward coast, it mixed with the relatively dry island air. Continued residence time over the heated island resulted in steady warming of the boundary layer, with a gradual rebound of moisture as the air approached the leeward coast sea breeze front. This was probably due to strong evapotranspiration over the islands.

The 23 Nov. 1995 case was characterized by light westerly surface flow in the morning, with strong northwesterly winds above 7 km AGL. A combination of moderate afternoon instability and low environmental wind shear resulted in a bulk Richardson number (R) of 494. According to the observational and modeling work of Weisman and Klemp (1982; 1984), this favored unsteady multicellular development of convection.

Early development over far northeastern Melville Is. was probably aided in part by convergence of the sea breeze and the synoptic air flow, and partly by the dynamical forcing associated with the upper-level trough just to the southwest of the Tiwi Is. It is postulated that upward motion induced by quasi-geostrophic forcing over this region lowered the convective inhibition sufficiently to trigger earlier-than-usual deep convection. The inertial instability of the upper-level wind field may have aided in the ventilation of the mature thunderstorm, but this could not be verified with the available data.

The upscale development of this early convection was based on the merging of isolated precipitating cells that formed over narrow peninsulas where opposing sea breezes collided. The spatial distribution of the new cells suggested that cloud bridging occurred above colliding downdrafts from the isolated cells

(Simpson, 1980). Once the cells merged, the focus of new development shifted to the leading edge of the developing gust front spreading to the west, above which new cells were triggered every 8-12 km. Deep convection ceased soon afterward, as the cold pool propagated into the island interior. The island boundary layer still was not well-moistened, and this may have caused the convective intensity to decrease temporarily along the leading edge of the gust front. Once the gust front collided with another active gust front over north-central Melville Is., a second-order merged storm emerged with storm tops to 20 km. The low-level forcing was also enhanced by the presence of the north coast sea breeze front.

The low-level convergence along the sea breeze front did not appear to generate the necessary low-level convergence to generate deep convection on its own. Doppler velocity estimates of radial convergence across the north coast sea breeze front indicated values on the order of 10^{-3} s^{-1}. Similar estimates across the edge of the gust front in far northeastern Melville Is. suggested convergence values 3 times greater than that found along the north sea breeze front. This illustrated the potency of early afternoon cool pools. The leeward coast sea breeze front was almost always the site of the first deep convection of the day, but it was only after the approach of an early-afternoon cool pool from the island interior that the deep convection truly proliferated.

Lacking high resolution measurements and radar coverage, some past observational studies suggested the initiation of Tiwi Island thunderstorms followed the collision of the north and south coast sea-breezes (Keenan et al., 1989; Keenan and Carbone, 1992). The modeling results of Golding (1993) even supported this. But upon closer inspection, it is clear that most of the time the windward coast sea breeze front never actually reached the opposite sea breeze front in a recognizable state. The first deep convection was usually triggered between the leeward sea breeze front and the approaching pockets of downdraft air originating from shallow precipitating cells embedded within the low-level flow. The windward coast sea breeze front may play a role in triggering these shallow cells by focusing low-level convergence, but its presence was often masked by the cells, and the maritime air mass behind the front was heavily modified by the time it approached the opposite-coast sea breeze.

On 23 Nov., the strong updraft above the boundary of two converging downdrafts stretched the low-level vorticity created at the surface. The width of the vortex was 12 km at the surface and tapered with height, eventually losing its character above 5 km elevation. In his numerical simulation of the 22 Nov. 1988 Tiwi island thunderstorm, Golding (1993) noted the presence of vortices on the order of $10^{-3}\ s^{-1}$, but they were transient in nature and smaller than those deduced by radar. This feature on 23 Nov. 1995 was too coherent to be dismissed as convective-scale turbulence, as proposed by Keenan et al. (1994) who observed radial shear in the mid-levels of the 22 Nov. 1988 storm. The existence of such rotation in island thunderstorms has dynamical implications. Intense rotation induces vertical acceleration towards the level where the circulation is strongest. This is due to the low-pressure perturbation created near the center of the vortex. On Nov. 23, the vortex was strongest near the surface which would imply a downward-directed contribution to the vertical acceleration above the vortex. The approximate magnitude of the pressure perturbation would be on the order of -1 mb. In the mid-latitudes, supercell mesocyclones dynamically lift the air beneath the strongest part of the mesocyclone through the same mechanism.

Additional mesoscale dynamics could have modulated the storm behavior on 23 Nov. The strong vertical wind shear between 7 and 11 km (4.5 m s^{-1} per km) could have created a high pressure perturbation on the upshear side and low pressure perturbation on the downshear side of the cell, which could have forced vertical accelerations on the flanks of the storm and affected its propagation and evolution.

Soon after the second-order merged storms over northern Melville Is. reached maximum strength, they became outflow-dominated. This was consistent with the high R value. Convection was restricted to the northwestern half of the expanding cold pool due to its continued access to untapped island boundary layer air and the dynamical support of the low-level wind profile. Although the updrafts of the new convection were highly sheared, they were not as sheared as the updrafts on the eastern edge of the island-scale cold-pool. The cells on the northwestern half were aided by the horizontal vorticity of the environmental flow which opposed the baroclinic generation of vorticity by the density current-like cold-pool (Rotunno et al., 1988). It was only here that the updrafts were not completely shunted back behind the advancing wedge of cold air and quickly detached from the high θ_e surface air.

The second case study day, 27 Nov. 1995, was characterized by weak deep tropospheric wind shear and light northeasterly surface flow. The surface flow focused convective development over the southwest sea breeze front.

A strong, wet microburst occurred 10 km north of the radar. The relatively moist and shallow mixed layer present over the islands suggested that water loading played a large role in comparison to the role it plays in typical upper Great Plains U. S. microbursts, where evaporative cooling accounts for most of the downdraft's negative buoyancy. The high reflectivity in the downdraft core was indicative of very heavy rain and supported this claim.

Once the 27 Nov. storm cells merged along the southern coast sea breeze front, they produced a strong downdraft that organized the system into a disjointed north-south oriented squall line. The trailing stratiform precipitation region and the line-perpendicular circulations were consistent with the conceptual model of a typical mesoscale convective system. The squall line discontinuously propagated to the west with an average velocity matching the 850-700 mb steering flow. Evident in the Doppler velocity field was a rear-to-front downdraft in the stratiform region and a highly sloped front-to-rear updraft in the convective region. The downshear tilt of the updrafts was to be expected with the high R value (112), however, the fact that R was lower than 23 Nov. matched well with the higher degree of convective organization observed on 27 Nov. On 23 Nov., the cold-pool was too strong to allow any deep convection to thrive along the edge of the main gust front. On 27 Nov., the instability was not as great and the cold pool was not as strong. Therefore, the updrafts began to organize into a mini-squall line as they propagated towards the ocean west of Bathurst Is.

Once again, convection was favored on the downshear side of the expanding cold-pool. Even though the eastern edge of the cold-pool that covered Bathurst Is. was interacting with untapped island boundary-layer air to its east, there still was no enhancement of thunderstorm cells as they propagated westward over the dome of cold air. They appeared to intensify briefly as they intercepted the boundary, but then they dissipated readily once they moved into the cooler air. This was consistent with the hypothesis that the low-level shear was too large on the eastern edge of the expanding cold-pool to promote deep, upright convection (in the presence of an easterly trade wind maximum).

5.2 Precipitation and electrical trends

The effects of beam blocking were drastically reduced by using dual-polarization derived estimates of rain rate. A significant bias was found in calculations of total storm rain mass flux when the rain rate estimates were based only on horizontal reflectivity, Z_h. The rain estimates were especially low at greater ranges, where the lowest elevation angle radar sweeps were utilized for surface rain rate estimates. Dual-polarization estimates based heavily on $R(K_{DP}, Z_{DR})$ and/or $R(K_{DP})$ algorithms were not affected nearly as much by beam blocking.

On the whole, the various rain rate estimation techniques produced similar magnitudes of total storm rain mass flux. As mentioned earlier, the techniques that used dual-polarimetric measurands were relatively insensitive to precipitation attenuation effects. On the other hand, the technique based solely on

$R(Z_h)$ was indeed affected by attenuation. When heavy precipitation occurred along significant portions of the radar beam, large propagation differential phase shifts resulted. Accordingly, Z_h and Z_{DR} required large corrections for horizontal and differential attenuation. This made the total storm rain mass flux very sensitive to the chosen attenuation correction coefficients (*a* and *b*). During one of the more intense stages of the 23 Nov. storm, the $R(Z_h)$ method produced suspiciously high estimates of total rain mass flux. These exceptional departures of the $R(Z_h)$ estimates from the dual-polarimetric estimates of rain mass flux were attributed to the difficulty in attaining a proper horizontal reflectivity attenuation correction coefficient (*a*) during the most intense stage of the storm. Although there were a couple exceptions, on average, the precipitation attenuation correction for Z_h did bring the $R(Z_h)$ estimates closer to the estimates derived from polarimetric methods.

Carey et al. (1999, manuscript to be submitted to *J. Appl. Meteor.*) found that large drop cores in MCTEX convection required extra attenuation correction. Carey et al. showed the coefficients *a* and *b* are nearly constant for small-to-moderate drops (e.g., $0.5<Z_{DR}<2$ dB), but actually increase with Z_{DR} for drop size distributions characterized by $Z_{DR}>2$ dB. Carey et al. therefore applied a 'large drop correction' to regions of large drops. This 'large drop correction' utilized enhanced attenuation correction coefficients (a* and b*) derived from simulations of scattering from large drops. The correction improved the internal consistency among the polarimetric variables and reduced the bias and standard error of the cumulative radar rainfall estimator $R(Z_h)$ (Carey et al., 1999, manuscript to be submitted to *J. Appl. Meteor.*).

Daily accumulated rain mass for all convection and for second-order merged cells was estimated. The amounts compared favorably with previous estimates for Tiwi Is. thunderstorms by Simpson et al. (1993).

5.2.1 Relation to CG flash rates

The physical basis for a relation between CG lightning and rainfall production rests on the ice phase. Graupel-ice crystal collisions are required to electrify the cloud to the point of producing lightning. Therefore, lightning is related to rainfall only to the extent that the rainfall was derived from ice-based precipitation, specifically, frozen graupel particles. Consider a precipitating cloud with no significant graupel mass. In this case, lightning and rainfall would be completely uncorrelated, due to the absence of lightning. If the fractional contribution of the ice phase to the total rainfall was high, then a better correlation between lightning and rainfall would be expected.

The rain mass flux was somewhat correlated with CG flash production, but specific types of mixed-phase precipitation were better correlated with CG flash rate (see Table 5.1). When dual-polarization radar measurements suggested elevated graupel mass in the mixed-phase region (i.e. between 0 and -40°C) the CG lightning flash rates increased. CG flash rates peaked just after or very close to the time that graupel mass in the mixed-phase region peaked. This suggests that ice-phase interactions were crucial to CG lightning development.

The 5-8 minute lag between graupel mass aloft and CG flash rates may signify that CG's were associated with the descent of graupel through the melting level. Carey and Rutledge (1996) found a similar relation between graupel and CG's in a multi-cell thunderstorm observed along the Front Range of Colorado. Carey and Rutledge postulated that the CG's were induced by a lower positive charge center that developed as graupel particles fell below the level of charge reversal. A lower positive charge would increase the electric field below the main negative charge layer and could provide a downward bias to the stepped leader, thus promoting cloud-to-ground flashes. The time lag of the precipitation fields on 23 Nov. in Table 5.1 were consistent with this hypothesis. Carey and Rutledge estimated that NIC would reverse the charge of a graupel particle about 4 minutes after it fell through the level of charge reversal. This is consistent with the 5 to 8 minute lag found between CG activity and peak mixed-phase graupel mass. Various laboratory studies have suggested that the level of charge reversal lies somewhere between -10 and -22°C (Takahashi, 1978; Jayaratne et al., 1983; Saunders et al., 1991) or 7-9 km AGL in the tropics. Falling from a height of 7 km, a graupel particle would take about 20 minutes to reach the surface as a large raindrop. Therefore, the 14 to17 minute lag of rain mass flux (relative to graupel mass) in the 23 Nov. case is also consistent with the hypothesis that the CG's were associated with the fallout of graupel particles. The similar evolution of precipitation-sized liquid water in the mixed-phase region suggests that a large percentage of graupel was probably composed of frozen raindrops.

Table 5.1 Coeffient of determination (R^2) between CG flash rate and C-pol radar-derived precipitation quantities

	23 November 1995 zero lag R^2, max. R^2, lag time	27 November 1995 zero lag R^2, max. R^2, lag time
precipitation-sized liquid water mass in mixed-phase region	0.60, 0.73, -9 min.	0.24, 0.24, 0 min.
graupel mass in mixed-phase region	0.75, 0.80, -5 to -8 min.	0.67, 0.67, 0 min.
rain mass flux at 1 km AGL	0.12, 0.45, 9 min.	0.39, 0.39, 0 min.

The excellent correlation between mixed-phase graupel mass and CG flash rate for the 27 Nov. case is illustrated in Fig. 4.7. Each small peak in graupel mass was matched with elevated CG rates. As mentioned earlier, the radar estimates of precipitation-sized liquid water mass in the mixed-phase region were probably erroneously high after 0645 UTC due to poor vertical resolution at large ranges (see Fig. 4.9). By ignoring the suspect times, the maximum R^2 value improved from 0.24 at 0 lag to 0.39 at 1 minute lag.

Many of the positive CG flashes that were detected on 23 Nov. were displaced downshear from the main cluster of negative CG flashes. This suggested that the thunderstorm charge distribution followed the conventional electric dipole model, with a layer of negatively charged graupel particles beneath an upper region of positively charged ice crystals. The northwesterly upper-level winds advected the anvil towards the southeast, away from the lower negative charge, and exposed the positive charge to the surface. This in turn, encouraged more positive discharges from the anvil to the ground.

Additional positive ground flashes were detected within heavy precipitation with no bias towards downshear displacement. Various explanations for these discharges were proposed including 1) the "inverted dipole" mechanism (MacGorman and Nielsen, 1991; Williams et al., 1991), 2) the "unshielding" of upper-level positive charge from the ground through neutralization of the negative charge layer by negative CG flashes (Pierce, 1955) and 3) the destruction of the lower negative charge layer and "unshielding" of upper-level positive charge through an enhanced precipitation current associated with rain fall rates greater than 100 mm hr^{-1} (Carey and Rutledge, 1998).

During the MCTEX, positive CG flashes within the trailing stratiform portion of squall lines were uncommon. However, the surface field mill often indicated net positive charge aloft during this final stage of thunderstorm development. The polarity of the electric field gradually switched from foul-weather to fair-weather as the convective region of the storm dissipated or propagated away from the field mill. This slow oscillation of the surface electric field was probably a segment of the end-of-storm-oscillation (EOSO) also noted by other investigators (e.g. Moore and Vonnegut, 1977; Marshall and Lin, 1992; Williams et al., 1994). The magnitude of the electric field was moderate (1-2 kV m^{-1}) with few positive CG's observed within the stratiform region of the MCTEX storms. Maybe the squall lines were too short-lived and weak to create much positive charge in the anvil through in-situ mechanisms involving a well-established mesoscale updraft. By the time most mesoscale convective systems matured, they already were on the verge of propagating off of the Tiwi Islands. After they left the influence of the islands they often decayed rapidly over the cooler ocean waters. The positive charge region might also be too distant from the surface due to the high melting level and tropopause height found in the tropics.

5.2.2 Relation to total flash rate

C-pol radar and a collocated flat plate antenna provided information on the relationship between mixed-phase precipitation and total lightning flash rate. In early stages of thunderstorm development, the total flash rates were well correlated with the radar data. Radar-inferred graupel and supercooled raindrop amounts rose and fell along with total flash rates. For both days, lightning was only detected in developing cells slightly after the appearance of large ice particles above the freezing level (as estimated by C-pol radar). This is consistent with NIC theory, which calls for relatively high graupel particle concentrations before significant charging can occur in a storm.

On 23 Nov., sensitivity tests revealed that the dual-polarization radar estimates of precipitation mass were highly sensitive to the chosen range limit. The strongest convection occurred just beyond the traditional outer limit of the flat plate detection radius, so it is difficult to decide how much of the precipitation was associated with the lightning flashes detected by the flat plate. Since most of the convective complex occurred outside of 40 km range, the high flash rates detected by the flat plate suggested that radar data from beyond 40 km should be included. For 23 Nov., depending on whether a 40 or 50 km range restriction was applied, the maximum correlation between total flash rates and mixed-phase graupel precipitation improved from 0.43 at -20 min. lag to 0.64 at zero lag. Due to the location of the storm, inferences about the role of NIC are difficult to make. If the radar analysis is limited to 40 km range, the NIC mechanism cannot explain the second major surge in total flash rate. However, expanding the range brings the total flash rate and mixed-phase precipitation fields in phase with each other and provides support for the NIC theory.

On 27 Nov. the upward spike in flash rate during the later stages of the afternoon is also inconsistent with the estimated graupel mass near the radar. Several explanations were offered for this radical departure from expected lightning behavior. High IC flash rates have been attributed to extreme updrafts in which the lower negative charge layer is elevated higher than usual, thus hindering CG discharges and promoting IC discharges. Another possible explanation involves the anvil canopy that spread over the cells. The anvil originated from a squall line to the west. Perhaps additional positive charge on the ice crystals in the anvil enhanced the electric field between the lower negative charge layer and the upper levels, providing an impetus for increased IC flash rates. Another explanation which seems likely, considering the modest appearance of the candidate thunderstorm cells, is unrelated to thunderstorm electrification. The flat plate data may have been contaminated by rain that was not detected by the AWS. Rainwater on the instrument could saturate its circuitry and cause the estimated total lightning flash rate to escalate, as observed on other MCTEX days.

5.2.3 Relation to mergers

The multiplicative effect of cloud mergers on electrical activity (illustrated by Figs. 3.8, 3.17, 4.14) could be attributed to several factors that influence the rate of non-inductive charging. First, consider a single graupel particle with radius R falling through a population of ice crystals (Fig. 5.1). Suppose that on average, q coulombs of charge are separated per graupel-ice particle collision via NIC transfer. The charging rate (dQ/dt) for the graupel particle can be expressed as

$$\frac{dQ}{dt} = \pi R^2 VnqE \quad , \tag{5.1}$$

where V is the graupel fall velocity relative to the ice crystals, and E the collision/separation efficiency. The charging rate for a single graupel particle is directly proportional to n, the number concentration of ice crystals. The total charging rate for multiple graupel particles would be proportional to the number concentration of graupel particles (N).

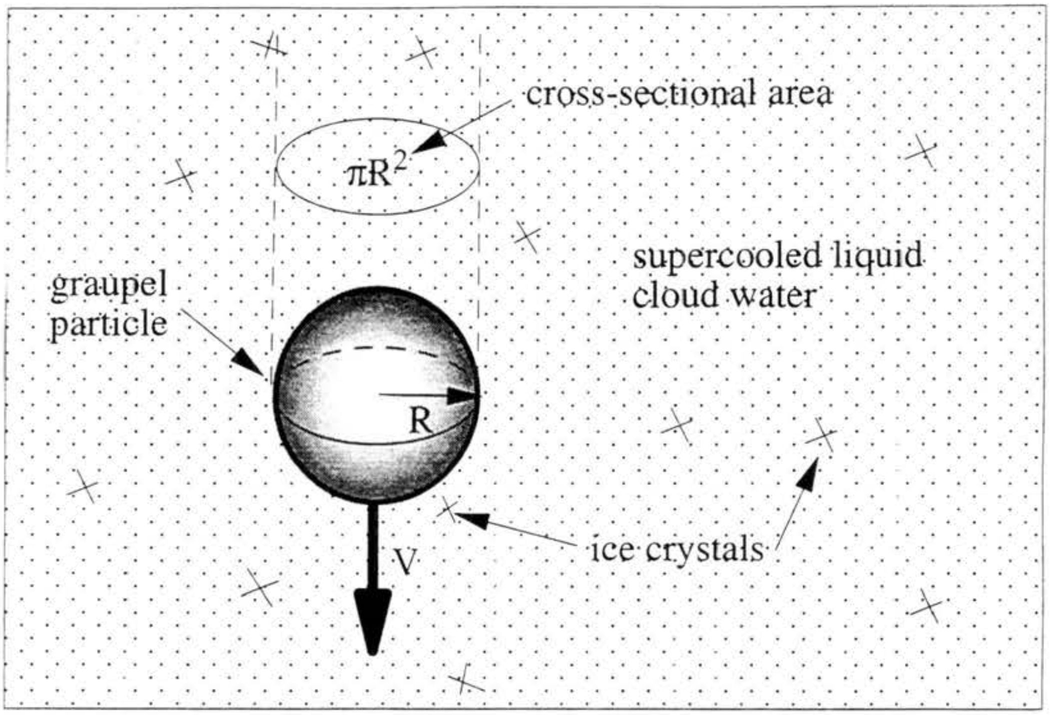

Fig. 5.1 Schematic diagram of a riming graupel sphere falling through a population of ice crystals. In a unit time, the graupel particle sweeps out a volume equal to its cross-sectional area times its fall-speed ($\pi R^2 V$). The rate of graupel-ice crystal collision/separations is proportional to the number concentration of ice cystrals and $\pi R^2 VE$, where E is the probability that an ice crystal in the path of the graupel particle will collide with and separate from the graupel particle.

Therefore, cloud mergers could promote enhanced electrification through NIC in a number of ways. First of all, merged convective systems convert a larger fraction of surface-based CAPE to updraft kinetic energy because they are less prone to the effects of entrainment compared to isolated convective cells. The increased updraft speeds could increase the volume of the region above the freezing level in which the NIC mechanism operates. The latent heat of fusion released during the glaciation process could also augment the updraft speed. The enhanced updraft speeds also would lead to higher liquid water contents which could in turn favor an increase of q (Takahashi, 1978). Second, the convection from the previous generation of cells could provide copious amounts of ice crystals (higher n in eqn. 5.1) to the mixed-phase region of the storms, thus effectively "jump-stating" the charging mechanism. The precipitation-sized ice mass *not* attributed to graupel (ice crystals and snow aggregates) did not increase as sharply as the graupel and supercooled water did following the first cloud mergers. It took a while longer to create a large mass of small ice particles. By the time of the second-order mergers, however, the concentration of small ice particles was greater, and this would have allowed the graupel particles to charge more rapidly (assuming a continued influx of supercooled water). Also, the larger updrafts within the merged cells could loft more supercooled water above the freezing level and easily produce higher amounts of graupel from frozen rain drops. This would increase N in eqn. 5.1. Lightning production appeared to be especially sensitive to the amount of graupel in the mixed-phase region. As soon the bulk of the graupel fell out, the lightning rate dropped sharply. This drop in lightning rate occurred despite the continued rise in estimated small ice particle mass.

5.3 Future work

The MCTEX produced a wealth of information about tropical island thunderstorms and some data still remains to be utilized. Additional case studies similar to those pursued in this thesis could improve understanding of precipitation attenuation at C-band. Perhaps the correction method could be refined, or perhaps the correction coefficients themselves could reveal microphysical qualities of the thunderstorms, such as the evolution of their drop size distribution. The radar rain rate estimates could also be compared with "ground-truth" data from the surface rain gauge network. MCTEX days for which it rained heavily over the D-scale rain gauge network would be especially useful. The radar could then be calibrated and the various polarimetric radar algorithms compared and improved.

The MCTEX had only one flat plate antenna at a fixed location, so the ability to measure total lightning flash rates was sometimes hampered. Often, the major convection was located beyond the flat plate detection radius or on the boundary. Some MCTEX days offered less ambiguous flash rate data than the case study days chosen for this thesis, and this may allow the effect of cloud mergers on total flash rate to be investigated more rigorously. The IC to CG flash ratio could also be tracked more accurately with better flat plate coverage. The upcoming TRMM/Brazil field project in Amazonia (Jan.-Feb. 1999) will improve upon the MCTEX situation by using a network of flat plates. These instruments will be sensitive to about 100 km range and will be fitted with rigid canopies to combat rain-contamination.

Flat plate antennas and CG direction finder networks cannot describe the vertical structure of the lightning flashes. Knowing the vertical structure of lightning would provide clues about charge distribution and the origin of negative and positive CG's. Valuable information about the spatial charge distribution of tropical thunderstorms could be obtained with a network of field mills, similar to that used by Koshak and Krider (1989), or with 3D mapping technologies such as LDAR (Maier et al., 1995).

CHAPTER 6

REFERENCES

Atkins, N. T., R. M. Wakimoto, and T. M. Weckworth, 1995: Observations of the sea-breeze front during CaPE. Part II: Dual-Doppler and aircraft analysis. *Mon. Wea. Rev.*, **123,** 944-969.

Avila, E. E., and G. M. Caranti, 1994: A laboratory study of static charging by fracture in ice growing by riming. *J. Geophys. Res.*, **99,** 10611-10620.

Aydin, K., H. Direskeneli, and T. A. Seliga, 1987: Dual polarization radar estimation of rainfall parameters compared with ground-based disdrometer measurements: 29 October 1982, central Illinois experiment. *IEEE Trans. Geosci. Remote Sens.*, **25,** 834-844.

Aydin, K., V. Giridhar, 1992: C-band dual-polarization radar observables in rain. *J. Atmos. Oceanic Tech.*, **9,** 383-390.

Aydin, K., Y. Zhao, and T. A. Seliga, 1989: Rain-induced attenuation effects on C-band dual-polarization meteorological radars. *IEEE Trans. Geosci. Remote Sens.*, **27,** 57-66.

BMRC, Nov. 1998: BMRC MCTEX Experimental Summary, http://www.BoM.GOV.AU/bmrc/meso/Project/research/summary.htm#23nov

Baker, M. B., and J. G. Dash, 1994: Mechanism of charge transfer between colliding ice particles in thunderstorms. *J. Geophys. Res.*, **99,** 10621-10626.

Balakrishnan, N., and D. S. Zrnic, 1990: Estimation of rain and hail rates in mixed-phase precipitation. *J. Atmos. Sci.*, **47,** 565-583.

Baral, K. N., and D. Mackerras, 1993: Positive cloud-to-ground lightning discharges in Kathmandu thunderstorms. *J. Geophys. Res.*, **98,** 10331-10340.

Barnes, S. L., 1980: Report on a meeting to establish a common Doppler radar data exchange format. *Bull. Amer. Meteor. Soc.*, **61,** 1401-1404.

Battan, L. J., 1973: *Radar Observation of the Atmosphere.* Techbooks, 324 pp.

Black, R. A., J. Hallett, and C. P. R. Saunders, 1993: Aircraft studies of precipitation and electrification in hurricanes. *Proc.*, 17th Conf. on Severe and Local Storms and Conf. on Atmos. Elec., Oct. 4-8, St. Louis, MO, J20-J25.

Brady, R. H., and E. J. Szoke, 1989: Case study of nonmesocyclone tornado development in northeast Colorado: similarities to waterspout formation. *Mon. Wea. Rev.*, **117,** 843-856.

Bringi, V. N., K. Knupp, A. Detwiler, L. Liu, I. J. Caylor, and R. A. Black, 1997: Evolution of a Florida thunderstorm during the Convection and Precipitation/Electrification Experiment: the case of 9 August 1991. *Mon. Wea. Rev.*, **125,** 2131-2160.

Bringi, V. N., V. Chandrasekar, N. Balakrishnan, and D. S. Zrnic, 1990: An examination of propagation effects in rainfall on radar measurements at microwave frequencies. *J. Atmos. Oceanic Tech.*, **7,** 829-840.

Brook, M., M. Nakano, P. Krehbiel, and T. Takeuti, 1982: Electrical structure of the Hokuriku winter thunderstorms. *J. Geophys. Res.*, **87,** 1207-1215.

Brown, R. G., and C. S. Bretherton, 1997: A test of the strict quasi-equilibrium theory on long time and space scales. *J. Atmos. Sci.*, **54,** 624-638.

Buechler, D. E., P. D. Wright, and S. J. Goodman, 1990: Lightning/rainfall relationships during COHMEX. *Preprints,* 16th Conf. on Severe Local Storms, Kananaskis Park, AB, Canada, Amer. Meteor. Soc., 710-714.

Bureau of Meteorology, Nov. 1998: http://www.bom.gov.au/climate/averages/tables/cw_014142.shtml

CEPEX Experiment Design, 1993: Center for Clouds, Chemistry and Climate, Scripps Institute of Oceanography, Univ. of California, San Deigo.

Carbone, R. E., T. D. Keenan, J. W. Wilson, and J. M. Hacker, 1997: Boundary layer structures and the role of breezes in forcing deep island convection. Submitted to 28th Conf. on Radar Meteor., Sept. 7-12, Austin, TX.

Carey, L. D., S. A. Rutledge, W. A. Peterson, and T. D. Keenan, 1997b: C-Band polarimetric radar and electrical observations of a maritime continent thunderstorm. *Preprints,* 22nd Conf. on Hurricanes and Tropical Meteor., May 19-23, 1997, Fort Collins, CO, 384-385.

Carey, L. D., S. A. Rutledge, and T. D. Keenan, 1997a: Correction of attenuation and differential attenuation at S- and C-band using differential propagation phase. *Preprints,* 28th Conf. on Radar Meteor., Sept. 7-12, Austin, TX.

Carey, L. D., and S. A. Rutledge, 1996: A multiparameter radar case study of the microphysical and kinematic evolution of a lightning producing storm. *Meteor. Atmos. Phys.*, **59,** 33-64.

Carey, L. D., and S. A. Rutledge, 1998: Electrical and multiparameter radar observations of a severe hailstorm. *J. Geophys. Res.*, **103,** 13979-14000.

Chandrasekar, V., V. N. Bringi, and D. S. Zrnic, 1990: Error structure of multiparameter radar and surface measurements of rainfall. Part III: Specific differential phase. *J. Atmos. Oceanic Tech.*, **7,** 621-629.

Chiba, O., 1997: Variability of the sea-breeze front from sodar measurements. *Boundary-Layer Meteor.*, **82,** 165-174.

Christian, H. J., R. J. Blakeslee, and S. J. Goodman, 1989: The detection of lightning from geostationary orbit. *J. Geophys. Res.*, **94,** 13329-13337.

Conway, J. W., and D. S. Zrnic, 1993: A study of embryo production and hail growth using dual-Doppler and multiparameter radars. *Mon. Wea. Rev.*, **121,** 2511-2528.

Cooper, H. J., M. Garstang, and J. Simpson, 1982: Diurnal interaction between convection and peninsular-scale forcing over south Florida. *Mon. Wea. Rev.*, **110,** 486-503.

Cressman, G. P., 1959: An operational objective analysis system. *Mon. Wea. Rev.*, **87,** 367-374.

Crook, N. A., 1997a: Simulation of convective storms over the Tiwi Islands and comparison with observations from MCTEX. BMRC Research Report No. 4. BMRC GPO Box 1289K, Melbourne, Australia, 7-10.

Crook, N. A., 1997b: Simulation of convective storms over the Tiwi Islands and comparison with observations from MCTEX. *Preprints,* 22nd Conf. on Hurricanes and Tropical Meteor., May 19-23, 1997, Fort Collins, CO, 376-377.

Doviak, R. J., and D. S. Zrnic, 1984: *Doppler Radar and Weather Observations.* Academic Press, 458 pp.

Doviak, R. J., and D. S. Zrnic, 1993: *Doppler Radar and Weather Observations.* 2nd ed. Academic Press, 562 pp.

Engholm C. D., E. R. Williams, and R. M. Dole, 1990: Meteorological and electrical conditions associated with positive cloud-to-ground lightning. *Mon. Wea. Rev.*, **118,** 470-487.

Gamache, J. F., F. D. Marks, Jr., and R. W. Burpee, 1987: EMEX data report: The equatorial mesoscale experiment. NOAA/Atlantic Oceanographic and Meteorological Laboratory, 4301 Rickerbacker Causeway, Miami, Florida, 33149.

Golding, B. W., 1993: A numerical investigation of tropical island thunderstorms. *Mon. Wea. Rev.*, **121,** 1417-1433.

Golestani, Y., V. Chandrasekar, and V. N. Bringi, 1989: Intercomparison of multiparameter radar measurements. *Proc.*, 24th Conf. Radar Meteor., Tallahassee, FL, Amer. Meteor. Soc., 309-314.

Goodman, S. J., 1995: Lightning Imaging Sensor (LIS) science team meeting. *Earth Observer,* **7,** 3-6.

Goodman, S. J., D. E. Buechler, P. D. Wright, and W. D. Rust, 1988: Lightning and precipitation history of a microburst-producing storm. *Geophys. Res. Lett.*, **15,** 1185-1188.

Gorgucci, E., and G. Scarchilli, 1994: A robust estimator of rainfall using differential reflectivity. *J. Atmos. Oceanic Tech.*, **11,** 586-592.

Hallett, J., and S. C. Mossop, 1974: Production of secondary ice particles during the riming process. *Nature*, **249,** 26-28.

Hartmann, D. L., H. H. Hendon, and R. A. Houze, Jr., 1984: Some implications of the mesoscale circulations in tropical cloud clusters for large-scale dynamics and climate. *J. Atmos. Sci.*, **41,** 113-121.

Helmis, C. G., 1987: Observations of sea breeze fronts near the shoreline. *Boundary-Layer Meteor.*, **38,** 395-410.

Hildebrand, P. H., 1978: Iterative correction for attenuation of 5 cm radar in rain. *J. Appl. Meteor.*, **17,** 508-514.

Hitschfeld, W., and J. Borden, 1954: Errors inherent in the radar measurment of rainfall at attenuating wavelengths. *J. Meteor.*, **11,** 58-67.

Holland, G. J., J. L. McBride, R. K. Smith, D. J. Jasper, and T. D. Keenan, 1986: The BMRC Australian Monsoon Experiment. AMEX. *Bull. Amer. Meteor. Soc.*, **67,** 1466-1472.

Holland, G. J., and J. L. McBride, 1989: Quasi-trajectory analysis of a sea breeze front. *Quart. J. Roy. Meteor. Soc.*, **115,** 571-580.

Holle, R. L., and S. P. Bennett, 1997: Lightning Ground Flashes Associated with Summer 1990 Flash Floods and Streamflow in Tucson, Arizona: An Exploratory Study. *Mon. Wea. Rev.*, **125,** 1526-1536.

Houze, R. A., Jr., 1989: Observed structure of mesoscale convective systems and implications for large-scale heating. *Quart. J. Roy. Meteor. Soc.*, **115,** 425-461.

Houze, R. A., Jr., 1993: *Cloud Dynamics.* Academic Press, 573 pp.

Houze, R. A., Jr., S. A. Rutledge, M. I. Biggerstaff, and B. F. Smull, 1989: Interpretation of Doppler weather radar displays of midlatitude convective systems. *Bull. Amer. Meteor. Soc.*, **70,** 608-619.

Houze, R. A., Jr., S. G. Geotis, F. D. Marks, and A. K. West, 1981: Winter monsoon convection in the vicinity of North Borneo. Part I: Structure and time variation of the clouds and precipitation. *Bull. Amer. Meteor. Soc.*, **109,** 1595-1614.

Hubbert, J., V. N. Bringi, L. D. Carey, and S. Bolen, 1998: CSU-CHILL polarimetric radar measurements from a severe hail storm in eastern Colorado. *J. Appl. Meteor.*, **37,** 749-775.

Illingworth, A. J., and J. Latham, 1977: Calculations of electric field structure and charge distributions in thunderstorms. *Quart. J. Roy. Meteor. Soc.*, **103,** 281-295.

Jameson, A. R., 1985: Microphysical interpretation of multiparameter radar measurements in rain, Pt. 3, Interpretation and measurement of propagation differential phase shift between orthogonal linear polarizations. *J. Atmos. Sci.*, **42,** 607-614.

Jameson, A. R., 1987: Relations among linear and circular polarization parameters measured in canted hydrometeors. *J. Atmos. Oceanic Tech.*, **4,** 634-645.

Jameson, A. R., 1991: A comparison of microwave techniques for measuring rainfall. *J. Appl. Meteor.*, **30,** 32-54.

Jameson, A. R., 1992: The effect of temperature on attenuation-correction schemes in rain using polarization propagation differential phase shift. *J. Appl. Meteor.*, **31,** 1106-1118.

Jameson, A. R., and J. H. Dave, 1988: An interpretation of circular polarization measurements affected by propagation differential phase shift. *J. Atmos. Oceanic Tech.*, **5,** 405-415.

Janowiak, J. E., A. F. Krueger, and P. F. Arkin, 1985: Atlas of outgoing longwave radiation derived from NOAA satellite data. NOAA Atlas No. 6. U.S. Dept. of Commerce, Washington, D. C.

Jayaratne, E. R., C. P. R. Saunders, and J. Hallett, 1983: Laboratory studies of the charging of soft-hail during ice crystal interactions. *Quart. J. Roy. Meteor. Soc.*, **109,** 609.

Jayaratne, E. R., and C. P. R. Saunders, 1984: The "rain-gush", lightning, and the lower positive charge center in thunderstorms. *J. Geophys. Res.*, **89,** 11816-11818.

Jayaratne, E. R., and C. P. R. Saunders, 1985: Reply. *J. Geophys. Res.*, **90,** 10755.

Keenan, T. D., B. Ferrier, and J. Simpson, 1994a: Development and structure of a maritime continent thunderstorm. *Meteor. and Atmos. Phys.*, **53,** 185-222.

Keenan, T. D., B. R. Morton, M. J. Manton, and G. J. Holland, 1989: The Island Thunderstorm Experiment (ITEX): a study of tropical thunderstorms in the maritime continent. *Bull. Amer. Meteor. Soc.*, **70,** 152-159.

Keenan, T. D., B. R. Morton, X. S. Zhang, and K. Nyguen, 1990: Some characteristics of thunderstorms over Bathurst and Melville islands near Darwin, Australia. *Quart. J. Roy. Meteor. Soc.*, **116,** 1153-1172.

Keenan, T. D., G. J. Holland, S. A. Rutledge, J.Simpson, J. McBride, J. Wilson, M. Moncrieff, R. Carbone, W. Frank, B. Sanderson, N. Tapper, and J. Hallett, 1994b: Science plan Maritime Continent Thunderstorm Experiment (MCTEX), BMRC Research Report, **44,** 61 pp.

Keenan, T. D., K. Glasson, F. Cummings, T. S. Bird, J. Keeler, and J. Lutz, 1998: The BMRC/NCAR C-band polarimetric (C-POL) Radar System. *J. Atmos. Oceanic Tech.*, **15,** 871-886.

Keenan, T. D., K. Puri, G. Mills, and R. Bowen, 1996a: Regional BMRC analyses of atmospheric circulation during MCTEX. BMRC Research Report, **57,** 67 pp.

Keenan, T. D., P. May, D. S. Zrnic, L. D. Carey, and S. A. Rutledge, 1997: Tropical rainfall estimation during the Maritime Continent Thunderstorm Experiment (MCTEX) using a C-band polarimetric radar. *Preprints,* 22nd Conf. on Hurricanes and Trop. Meteor., May 19-23, Ft. Collins, CO, Amer. Meteor. Soc., 386-387.

Keenan, T. D., R. E. Carbone, S. A. Rutledge, J. Wilson, G. J. Holland, and P. May, 1996b: The Maritime Continent Thunderstorm Experiment (MCTEX): Overview and initial results. *Preprints,* 7th Conf. on Mesoscale Processes, Sept. 9-13, Reading, UK, Amer. Meteor. Soc., 326-328.

Keenan, T. D., R. J. Potts, and J. Wilson, 1991: The Darwin Area Forecasting Experiment: description and preliminary results. *Australian Meteor. Mag.,* **39,** 211-222.

Keenan, T. D., and L. R. Brody, 1988: Synoptic-scale modulation of convection during the Australian summer monsoon. *Mon. Wea. Rev.,* **116,** 71-85.

Keenan, T. D., and R. E. Carbone, 1992: A preliminary morphology of precipitation systems in tropical northern Australia. *Quart. J. Roy. Meteor. Soc.,* **118,** 283-326.

Klemp, J. B. and R. Rotunno, 1983: Study of the tornadic region within a supercell thunderstorm. *J. Atmos. Sci.,* **40,** 359-377.

Koenig, L. R., 1977: Rime-splintering hypothesis of cumulus glaciation examined using a field-of-flow cloud model. *Quart. J. Roy. Meteor. Soc.,* **103,** 585-606.

Koshak, W. J., R. J. Blakeslee, and J. C. Bailey. 1998: Lightning radio source retrieval using Advanced Lightning Direction Finder (ALDF) networks. *J. Geophys. Res.,*submitted.

Koshak, W. J., and E. P. Krider, 1989: Analysis of lightning field changes during active Florida thunderstorms. *J. Geophys. Res.,* **94,** 1165-1186.

Krehbiel, P. R., 1986: The electrical structure of thunderstorms. In *The Earth's Electrical Environment,* National Academy Press, Washington, D.C., 90-113.

Krider, E. P., R. C., Noggle, and M. A. Uman, 1976: Wideband magnetic direction finder for lightning return strokes. *J. Appl. Meteor.,***15,** 301-306.

Krishnamurti, T. N., M. Kanamitsu, W. J. Koss, and J. D. Lee, 1973: Tropical east-west circulations during the northern winter. *J. Atmos. Sci.,* **30,** 780-787.

Kuettner, J. P., 1971: Cloud bands in the earth's atmosphere: observations and theory. *Tellus,* **23,** 404-425.

Lafore, J.-P., and M. W. Moncrieff, 1989: Numerical investigation of the organization and interaction of the convective and stratiform regions of tropical squall lines. *J. Atmos. Sci.,* **46,** 521-544.

Laird, N. F., D. A. R. Kristovich, R. M. Rauber, H. T. Ochs, III, and L. J. Miller, 1995: The Cape Canaveral sea and river breezes: kinematic structure and convective initiation. *Mon. Wea. Rev.,* **123,** 2942-2956.

Lau, K.-M., C. P. Chang, and P. H. Chan, 1983: Short-term planetary-scale interactions over the tropics and mid-latitudes. Part II: Winter-MONEX period. *Mon. Wea. Rev.*, **111,** 1372-1388.

Lau, K.-M., and L. Peng, 1987: Origin of low frequency (intra-seasonal) oscillations in the tropical atmosphere. Part I: The basic theory. *J. Atmos. Sci.*, **44,** 950-972.

LeMone, M. A., 1973: The structure and dynamics of horizontal roll vortices in the planetary boundary layer. *J. Atmos. Sci.*, **30,** 568-581.

Lopez, R. E., 1978: Internal structure and development processes of c-scale aggregates of cumulus clouds. *Mon. Wea. Rev.*, **106,** 1488-1494.

MacGorman, D. R., D. W. Burgess, V. Mazur, W. D. Rust, W. L. Taylor, and B. C. Johnson, 1989: Lightning rates relative to tornadic storm evolution on 22 May 1981. *J. Atmos. Sci.*, **46,** 221-250.

MacGorman, D. R., and D. W. Burgess, 1994: Positive cloud-to-ground lightning in tornadic storms and hailstorms. *Mon. Wea. Rev.*, **122,** 1671-1697.

MacGorman, D. R., and K. E. Nielsen, 1991: Cloud-to-ground lightning in a tornadic storm on 8 May 1986. *Mon. Wea. Rev.*, **119,** 1557-1574.

Mackerras, D., and M. Darveniza, 1994: Latitudinal variation of lightning occurrence characteristics. *J. Geophys. Res.*, **99,** 10813-10821.

Madden, R. A., and P. R. Julian, 1994: Observations of the 40-50-day tropical oscillation: A review. *Mon. Wea. Rev.*, **112,** 814-837.

Maier, L. M., C. Lennon, P. Krehbiel, M. Stanley, and M. Robison, 1995: Comparison of lightning and radar observations from the KSC LDAR and NEXRAD radar systems. *Preprints,* 27th Conf. Radar Meteor., Amer. Meteor. Soc., 648-650.

Marshall, J. S., and W. Palmer, 1948: The distribution of raindrops with size. *J. Meteor.*, **5,** 165-166.

Marshall, T. C., and W. P. Winn, 1982: Measurements of charged precipitation in a New Mexico thunderstorm: Lower positive charge centers. *J. Geophys. Res.*, **87,** 7141-7151.

Marshall, T. C., and W. P. Winn, 1985: Comments on "The 'rain gush,' lightning, and the lower positive center in thunderstorms. *J. Geophys. Res.*, **90,** 10753-10754

Mason, P. J., and R. I. Sykes, 1982: A 2-D numerical study of horizontal roll vortices in an inversion-capped planetary boundary layer. *Quart. J. Roy. Meteor. Soc.*, **108,** 801-823.

McCarthy, J., and J. W. Wilson, 1984: The microburst as a hazard to aviation: structure, mechanisms, climatology and nowcasting. *Preprints,* 2nd International Symposium on Nowcasting, 3-7 Sept., 1984, Norrkoping, Sweden, 21-30.

Michimoto, K., 1991: A study of radar echoes and their relation to lightning discharge of thunderclouds in the Hokuriku District. Part I: Observation and analysis of thunderclouds in summer and winter. *J. Meteor. Soc. Japan,* **69,** 327-335.

Miller, M. J., and A. K. Betts, 1977: Travelling convective storms over Venezuala. *Mon. Wea. Rev.,* **105,** 833-848.

Mitsumoto, S., U. Hiromasa, and H. Ozoe, 1983: Laboratory experiment on the dynamics of the land and sea breeze. *J. Atmos. Sci.,* **40,** 1228-1240.

Moore, C. B., and B. Vonnegut, 1977: The thundercloud. In *Lightning, Vol. 1: Physics of Lightning,* R. H. Golde, ed., Academic Press, 64-98.

Nicholls, M. E., R. A. Pielke, and W. R. Cotton, 1991: A two-dimensional numerical investigation of the interaction between sea breezes and deep convection over the Florida Reninsula. *Mon. Wea. Rev.,* **119,** 298-323.

Ogura, Y, Y.-L. Chen, J. Russell, and S.-T. Soong, 1979: On the formation of organized convective systems observed over the eastern Atlantic. *Mon. Wea. Rev.,* **107,** 426-441.

Oye, R., and R. E. Carbone, 1981: Interactive Doppler editing software. *Preprints,* 20th Conf. on Radar Meteor., Boston, MA, Amer. Meteor. Soc., 683-689.

Petersen, W. A., 1997: Multi-Scale Process Studies in the Tropics: Results from Lightning Observations. Ph.D. Dissertation, Dept. Atmospheric Science, Colorado State University, Fort Collins, Colorado.

Petersen, W. A., S. A. Rutldege, and R. E. Orville, 1996: Cloud-to-ground observations from TOGA COARE: selected results and lightning location algorithms. *Mon. Wea. Rev.,* **124,** 602-620.

Petersen, W. A., and S. A. Rutledge, 1998: On the relationship between cloud-to-ground lightning and convective rainfall. *J. Geophys. Res.,* **103,** 14025-14040.

Pielke, R. A., 1974: A three-dimensional numerical model of the sea-breeze phenomenon over south Florida. *Mon. Wea. Rev.,* **102,** 115-139.

Pierce, E. T., 1955: The development of lightning discharges. *Quart. J. Roy. Meteor. Soc.,* **81,** 229-240.

Price, C., and D. Rind, 1992: A simple lightning parameterization for calculating global lightning distributions. *J. Geophys. Res.,* **97,** 9919-9933.

Price, C., and D. Rind, 1994: Possible implications of global climate change on global lightning distributions and frequencies. *J. Geophys. Res.,* **99,** 10823-10831.

Pruppacher, H. R., and K. V. Beard, 1970: A wind tunnel investigation of the internal circulation and shape of water drops falling at terminal velocity in air, *Quart. J. Roy. Meteor. Soc.,* **96,** 247-256.

Puri, K., 1987: Some experiments on the use of tropical diabatic heating information for initial state specification. *Mon. Wea. Rev.*, **115,** 1394-1406.

Rabin, R. M., R. J. Doviak, and A. Sundara-Rajan, 1982: Doppler radar observations of momenutum flux in a cloudless convective layer with rolls. *J. Atmos. Sci.*, **39,** 851-863.

Ramage, C. S., 1968: Role of a tropical "maritime continent" in the atmospheric circulation. *Mon. Wea. Rev.*, **96,** 365-370.

Randell, S. C., S. A. Rutledge, R. D. Farley, and J. H. Helsdon, Jr., 1994: A modeling study of the early electrical development of tropical convection: Continental and oceanic (monsoon) storms. *Mon. Wea. Rev.*, **112,** 1852-1877.

Rasmussen, E. N., and S. A Rutledge, 1993: Evolution of quasi-two-dimensional squall lines. Part I: Kinematic and reflectivity structure. *J. Atmos. Sci.*, **50,** 2584-2606.

Rasmusson, E. M., and P. A. Arkin, 1985: *Interannual climate variability associated with the El Nino/Southern Oscillation. Coupled Ocean-Atmosphere models.* Amsterdam: Elsevier Science Publishers B. V., 697-725.

Reynolds, S. E.. M. Brook, and M. F. Gourley, 1957: Thunderstorm charge separation, *J. Meteor.*, **14,** 426-436.

Riehl, H., 1979: *Climate and weather in the Tropics.* Academic Press, 611 pp.

Rotunno, R., 1981: On the evolution of thunderstorm rotation. *Mon. Wea. Rev.*, **109,** 577-586.

Rotunno, R., J. B. Klemp, and M. L. Weisman, 1988: A theory for strong, long-lived squall lines. *J. Atmos. Sci.*, **45,** 463-485.

Rutledge, S. A., E. R. Williams, and T. D. Keenan, 1992: The Down Under Doppler and Electricity Experiment (DUNDEE): Overview and Preliminary results. *Bull. Amer. Meteor. Soc.*, **73,** 3-16.

Rutledge, S. A., E. R. Williams, and W. A. Petersen, 1993: Lightning and electrical structure of mesoscale convective systems. *Atmos. Res.*, **29,** 27-53.

Rutledge, S. A., and D. R. MacGorman, 1988: Cloud-to-ground lightning activity in the 10-11 June 1985 mesoscale convective system observed during the Oklahoma-Kansas PRE-STORM project. *Mon. Wea. Rev.*, **116,** 1393-1408.

Rutledge, S. A., and L. D. Carey, 1997: Lightning and mixed phase microphysics in tropical convection: A multiparameter radar study. *Preprints,* 28th Conf. on Radar Meteor., Sept. 7-12, Austin, TX.

Rutledge, S. A., and W. A. Petersen, 1994: Vertical radar reflectivity structure and cloud-to-ground lightning in the stratiform region of MCS's: Further evidence for in-situ charging in the stratiform region. *Mon. Wea. Rev.*, **122,** 1760-1776.

Ryzhkov, A., and D. S. Zrnic, 1995a: Comparison of dual-polarization radar estimators of rain. *J. Atmos. Oceanic Tech.*, **12,** 249-256.

Ryzhkov, A., and D. S. Zrnic, 1995b: Precipitation and attenuation measurements at a 10-cm wavelength. *J. Appl. Meteor.*, **34,** 2121-2134.

Ryzhkov, A., and D. S. Zrnic, and D. Atlas, 1997: Polarimetrically tuned R(Z) relations and comparison of radar rainfall methods. *J. Appl. Meteor.*, **36,** 340-349.

Sachidananda, M., and D. S. Zrnic, 1985: Z_{DR} measurement considerations for a fast scan capability radar. *Radio Sci.*, **20,** 907-922.

Saito, K., T. D. Keenan, G. J. Holland, and K. Puri, 1997: Numerical simulation of tropical diurnal thunderstorms over the Tiwi Islands. *Preprints,* 22nd Conf. on Hurricanes and Tropical Meteor., May 19-23, 1997, Fort Collins, CO, 378-379.

Saunders, C. P. R., W. D. Keith, and R. P. Mitzeva, 1991: The effect of liquid water on thunderstorm charging. *J. Geophys. Res.*, **96,** 11007-11017.

Saunders, C. P. R., and I. M. Brooks, 1992: The effects of high liquid water content on thunderstorm charging. *J. Geophys. Res.*, **96,** 14671-14676.

Scarchilli, G., E. Gorgucci, V. Chandrasekar, and T. A. Seliga, 1993: Rainfall estimation using polarimetric techniques at C-band frequencies. *J. Appl. Meteor.*, **32,** 1150-1160.

Schreiber, W. E., 1986: Case studies of thunderstorms initiated by radar-observed convergence lines. *Mon. Wea. Rev.*, **114,** 2256-2266.

Seitter, K. L., 1986: A numerical study of atmospheric density current motion including the effects of condensation. *J. Atmos. Sci.*, **43,** 3068-3076.

Sellers, W. D., 1969: A global climatic model based on the energy balance of the Earth-atmosphere system. *J. Appl. Meteor.*, **8,** 392-400.

Shih, S. F., 1988: Using lightning for rainfall estimation in Florida. *Trans. Amer. Soc. Agric. Eng.*, **31,** 750-755.

Simpson J. E., and R. E. Britter, 1980: Laboratory model of an atmospheric mesofront. *Quart. J. Roy. Soc.*, **106,** 485-500.

Simpson, J., 1980: Downdrafts as linkages in dynamic cumulus seeding effects. *J. Appl. Meteor.*, **19,** 477-487.

Simpson, J., B. R. Morton, M. McCumber, and R. Penc, 1986: Observations and mechanisms of GATE waterspouts. *J. Atmos. Sci.*, **43,** 753-782.

Simpson, J., N. E. Westcott, R. J. Clerman, and R. A. Pielke, 1980: On Cumulus Mergers. Arch. Meteor. Geophys. *Bioklim.*, **A29**, 1-40.

Simpson, J., R. F. Adler, and G. R. North, 1988: A proposed tropical rainfall measuring misson (TRMM) satellite. *Bull. Amer. Meteor. Soc.*, **69**, 278-295.

Simpson, J., T. D. Keenan, B. Ferrier, R. H. Simpson, and G. J. Holland, 1993: Cumulus mergers in the maritime continent region. *Meteor. and Atmos. Phys.*, **51**, 73-99.

Simpson, J., and W. L. Woodley, 1975: Florida Area Cumulus Experiments 1970-1973 rainfall results. *J. Appl. Meteor.*, **14**, 734-744.

Skinner, T., and N. Tapper, 1994: Preliminary sea breeze studies over Bathurst and Melville Islands, Northern Australia, as part of the Island Thunderstorm Experiment (ITEX). *Meteor. and Atmos. Phys.*, **53**, 77-94.

Solomon, R., and M. Baker, 1994: Electrification of New Mexico thunderstorms. *Mon. Wea. Rev.*, **122**, 1878-1886.

Sommeria, G., and J. Testud, 1984: COPT81: A field experiment for the study of dynamics and electrical activity in continental tropical regions. *Bull. Amer. Meteor. Soc.*, **65**, 4-10.

Srivastava, R. C., 1985: A simple model of evaporatively driven downdraft: application to microburst downdraft. *J. Atmos. Sci.*, **42**, 1004-1023.

Stolzenburg, M., T. C. Marshall, W. D. Rust, and B. F. Smull, 1994: Horizontal distribution of electrical and meteorological conditions across the stratiform region of a mesoscale convective system. *Mon. Wea. Rev.*, **122**, 1777-1797.

Szoke, E. J., E. J. Zipser, and D. P. Jorgensen, 1986: Radar study of convective cells in mesoscale systems in GATE, Pt. 1, Vertical profile statistics and comparison of the hurricanes. *J. Atmos. Sci.*, **43**, 182-197.

Takahashi, T., 1978: Riming electrification as a charge generation mechanism in thunderstorms. *J. Atmos. Sci.*, **35**, 1536-1548.

Takahashi, T., 1984: Thunderstorm electrification: A numerical study. *J. Atmos. Sci.*, **41**, 2541-2558.

Tapia, A., J. A. Smith, and M. Dixon, 1998: Esimation of convective rainfall from lightning observations. *J. Appl. Meteor.*, **37**, 1497-1509.

Ulbrich, C. W., 1983: Natural variations in the analytical form of the raindrop size distribution. *J. Clim. Appl. Meteor.*, **22**, 1764-1775.

Uman, M. A., 1987: *The Lightning Discharge.* Academic Press, 377 pp.

Wakimoto, R. M., 1982: Life cycle of thunderstorm gust fronts as viewed with Doppler radar and rawinsonde data. *Mon. Wea. Rev.*, **110,** 1060-1082.

Wakimoto, R. M., 1985: Forecasting dry microburst activity over the high plains. *Mon. Wea. Rev.*, **113,** 1131-1143.

Wakimoto, R. M., and J. W. Wilson, 1989: Nonsupercell tornadoes. *Mon. Wea. Rev.*, **117,** 1113-1140.

Wakimoto, R. M., and N. T. Atkins, 1994: Observations of the sea-breeze front during CaPE. Part I: Single-Doppler, satellite and cloud photogrammetry analysis. *Mon. Wea. Rev.*, **122,** 1092-1114.

Webster, P. J., and R. A. Houze, 1991: The Equatorial Mesoscale Experiment (EMEX): An overview. *Bull. Amer. Meteor. Soc.*, **72,** 1481-1505.

Webster, P. J., and R. R. Lukas, 1992: The TOGA Coupled Ocean-Atmosphere Response Experiment. *Bull. Amer. Meteor. Soc.*, **73,** 1377-1416.

Weisman, M. L., and J. B. Klemp, 1982: The dependence of numerically simulated convective storms on vertical wind shear and buoyancy. *Mon. Wea. Rev.*, **110,** 504-520.

Weisman, M. L., and J. B. Klemp, 1984: The structure and classification of numerically simulated convective storms in directionally varying wind shears. *Mon. Wea. Rev.*, **112,** 2479-2498.

Weisman, M. L., and J. B. Klemp, 1986: *Characteristics of Isolated Convective Storms. Mesoscale Meteorology and Forecasting.* Ed. P. S. Ray, Amer. Meteor. Soc., 331-358.

Wexler, R., 1946: Theory and observations of land and sea breezes. *Bull. Amer. Meteor. Soc.*, **27,** 272-287.

Wilks, D. S., 1995: *Statistical Methods in the Atmospheric Sciences.* Academic Press, 467 pp.

Williams, E. R., 1985: Large-scale charge separation in thunderclouds. *J. Geophys. Res.*, ***90,*** 6013-6025.

Williams, E. R., 1995: *Handbook of Atmospheric Electrodynamics,* CRC Press. Ed. H. Volland, pp 27-59.

Williams, E. R., M. E. Weber, and R. E. Orville, 1989: Relationship between lightning type and convective state of thunderclouds. *J. Geophys. Res.*, **94,** 13213-13220.

Williams, E. R., R. Zhang, and D. Boccippio, 1994: Microphysical growth state of ice particles and large-scale electrical structure of clouds. *J. Geophys. Res.*, **99,** 10787-10792.

Williams, E. R., R. Zhang, and J. Rydock, 1991: Mixed-phase microphysics and cloud electrification. *J. Atmos. Sci.*, **48,** 2195-2203.

Williams, E. R., S. A. Rutledge, S. G. Geotis, N. Renno, E. Rasmussen, and T. Rickenbach, 1992: A radar and electrical study of tropical "hot towers". *J. Atmos. Sci.*, **49,** 1386-1395.

Williams, E. R., S. G. Geotis, N. Renno, S. A. Rutledge, E. Rasmussen and T. Rickenbach, 1990: Hot towers in the tropics. *Preprints,* AMS Conference on Atmospheric Electricity, October 22-26, 1990, Kananaskisa Provincial Park, Alta, Canada.

Wilson, J. W., and D. L. Megenhardt, 1997: Thunderstorm initiation, organization, and lifetime associated with Florida boundary convergence lines. *Mon. Wea. Rev.,* **125,** 1507-1525.

Wilson, J. W., and W. E. Schreiber, 1986: Initiation of convective storms at radar-observed boundary-layer convergence lines. *Mon. Wea. Rev.,* **114,** 2516-2536.

Zahrai, A., and D. S. Zrnic, 1993: The 10-cm wavelength polarimetric weather radar at NOAA's National Severe Storms Laboratory. *J. Atmos. Sci.,* **10,** 649-662.

Ziegler, C. L., P. S. Ray, and D. R. MacGorman, 1986: Relations of the kinematics, microphysics, and electrification in an isolated mountain thunderstorm. *J. Atmos. Sci.,* **43,** 2098-2114.

Zipser, E. J., 1994: Deep cumulonimbus cloud systems in the tropics with and without lightning. *Mon. Wea. Rev.,* **122,** 1837-1851.

Zipser, E. J., and K. R. Lutz, 1994: The vertical profile of radar reflectivity of convective cells: A strong indicator of storm intensity and lightning probability? *Mon. Wea. Rev.,* **122,** 1751-1759.

Zrnic, D. S., 1977: Spectral moment estimates from correlated pulse pairs. *IEEE Trans. Aerosp. Electron. Syst.,* **AES-13,** 344-354.

Zrnic, D. S., N. Balakrishnan, C. L. Ziegler, V. N. Bringi, K. Aydin, and T. Matejka, 1993: Polarimetric signatures in the stratiform region of a mesoscale convective system. *J. Appl. Meteor.,* **32,** 678-693.

Zrnic, D. S., and A. Ryzhkov, 1996: Advantages of rain measurements using specific differential phase. *J. Atmos. Oceanic Tech.,* **13,** 454-464.